TABLE OF CONTENTS

MAY 11 1978

NASA Contractor Report 2974

COMPLETED

ORIGINAL

Design of a Submillimeter Laser Thomson Scattering System for Measurement of Ion Temperature in Summa

Herman C. Praddaude and Paul Woskoboinikow

NASA

165

NASA Contractor Report 2974

Design of a Submillimeter Laser Thomson Scattering System for Measurement of Ion Temperature in Summa

Herman C. Praddaude and Paul Woskoboinikow
Massachusetts Institute of Technology
Cambridge, Massachusetts

NASA

National Aeronautics
and Space Administration

Scientific and Technical
Information Office

1978

BLANK PAGE

INTRODUCTION

Submillimeter (SMM) laser Thomson scattering is an attractive, and possibly unique, technique for the measurement of ion temperature and heavy highly ionized impurity concentration in hot plasmas. However, the implementation of this technique requires the advancement of the state of the art of submillimeter high power lasers and very sensitive receivers, as well as sophisticated signal gathering and processing equipment. During the past two years substantial improvements in these areas have been achieved: laser power has been increased and the spectral purity has been improved by better than an order of magnitude; and receiver sensitivity has been improved by almost two orders of magnitude. Furthermore, the problems facing the practical implementation of this diagnostic technique are now better understood and this makes us very optimistic of their successful resolution.

This project has been aimed at prescribing the requirements for implementing the SMM laser Thomson scattering diagnostic for the NASA - Lewis Research Center SUMMA machine. In order to meet this goal, a detailed analysis of Thomson scattering for measurement of ion temperatures in laboratory plasmas had to be undertaken. Furthermore, because the laser and receiver configurations are continually being revised, some of the details specific to SUMMA have yet to be worked out. For these reasons we include in this report detailed background information which also make these results applicable to any plasma machine. We believe this has resulted in a report of more widespread interest to the physics community, and represents a necessary first step for the practical implementation of the Thomson scattering ion temperature diagnostic.

Because of the continuous flow of ideas regarding the construction of the SMM high power laser and of the receiver, where specific construction details are given, they reflect our views only up to about February 1977.

Sections 1 and 2 present qualitative and quantitative descriptions of the plasma as a source or scattering media of electromagnetic radiation. Section 3 presents calculations of the scattered signal levels to be expected from a simple plasma. We expect that the signal levels calculated here will not change appreciably for a realistic plasma. An integral part of this Section is a large number of graphs that should permit fast and convenient estimates of signal levels and the resulting trade offs between parameters to be evaluated. Sections 4 and 5 establish the signal processing alternatives and present what we believe are realistic specifications for the SMM laser and receiver. Section 6 treats the collection optics and Section 7 treats the focusing of the laser beam into the plasma. Section 8 presents general discussion of the important laser beam and receiver viewing dumps. Finally, in Section 9 the SMM laser development at the National Magnet Laboratory is summarized. Guidelines for extrapolation of the present results to the power levels necessary for a successful diagnostic tool are also presented.

SECTION 1

LASER LIGHT SCATTERING BY PLASMAS: INTRODUCTORY BACKGROUND

The purpose of this introductory section is not to provide a detailed justification of the results that we will be using in this report, but rather to provide an intuitive qualitative understanding of the basic phenomena relevant to the use of submillimeter laser light scattering for plasma diagnostics. The detailed results have been thoroughly justified in a number of publications which will be referred to later on. The most important qualitative understanding we will be striving for refers to the statistical properties of the scattered light since these properties will have a profound effect on the requirements imposed upon the high power laser, detector, and signal processing equipment.

The amount of electromagnetic (EM) radiation coming out from a plasma, whether it is intrinsic noise (bremsstrahlung, synchrotron radiation) or driven noise (scattering of an electromagnetic wave) is due mostly to the electrons. This is so because, according to the Larmor equation of classical electromagnetism, the radiation field of a moving charge is proportional to its acceleration. Since the electrons have the smallest mass, their acceleration and their radiation field will be the strongest. Close electron-ion encounters will be responsible for bremsstrahlung radiation; deexcitation from highly excited cyclotron levels in a nonuniform magnetic field will produce broad cyclotron harmonic resonance features that are present up to high harmonic orders. Plasma density fluctuations, whether they result from plasma instabilities or from geometric resonances, will produce strong scattered radiation. Debye shielding of the ions by the electrons is a source of electron density fluctuations that reflects the density fluctuations of the ions, and

3

hence their temperature. Not to be forgotten is the scattering of EM radiation by the density fluctuations of the electrons in a length scale smaller than the Debye shielding length, which will provide a measure of the electron temperature. These different sources of noise will prevail at different conditions which are dependent on the wavelength and scattering angle of the radiation, on the electron and ion temperatures (different components of a multicomponent plasma need not be in equilibrium with each other), on the average plasma density, and on the plasma dimensions. As it is to be expected from any statistical process, the statistical properties of the radiation are dependent on the distribution function of the electrons and ions. For all the results quoted in this report the equilibrium distribution function is assumed to be Maxwellian. However, in some instances, deviation from a Maxwellian distribution will have important measurable effects as it is the case with emission at the harmonics of the cyclotron frequency where a small fraction of suprathermal electrons may enhance the radiated power many fold.

In order to understand the properties of the scattered signal let us build it up as a superposition of the scattered signals from the individual electrons. Let us first consider, Fig. 1, an electron moving with a velocity $\underline{v}$ in the EM field of a propagating plane wave with wave vector $\overline{k}_i$ and angular frequency ω_i. The electron in its rest frame will see an electric field with a frequency $(\omega_i - \overline{k}_i \cdot \overline{v})$ that will cause its acceleration and subsequent emission of radiation at the same frequency. If this scattered radiation is observed along a direction with a wavevector $\overline{k}_s$ in the laboratory frame, the frequency of the scattered signal is ($\omega_i - \overline{k}_i \cdot \overline{v} + \overline{k}_s \cdot \overline{v}$). (Here electron recoil effects have been neglected.) Therefore for forward scattering the Doppler shift is zero while for backward scattering the Doppler shift is maximum. The electric field of the scattered wave, Fig. 2, at the observation point P (far away from the scattering region) for a uniform density N_e of scattering centers such that $N_e \lambda^3 \gg 1$ (i.e. we observe the total scattered signal from many electrons) will be

4

zero due to phase cancellation (we are neglecting boundary effects). Therefore, in order to observe a nonvanishing scattering power at P the electron density must be inhomogeneous within the scattering volume λ^3. That is, the electron density fluctuations are the ones responsible for the scattered signal (the average electron density N_e is assumed to be constant). Two different kinds of scattering are possible: 1) the electron density fluctuations are spatially coherent, i.e. a well developed density wave, in which case all the electrons add to the electric field of the scattered wave coherently, hence the scattered power is proportional to $(N_e \lambda^3)^2$; 2) the electron density fluctuations are random with a coherence length λ_c much smaller than λ. In the latter case the ensemble average of the electric field at P is zero, and the ensemble average of the magnitude squared of the electric field is porportional to the number of electrons in the scattering volume, i.e. now it is the average scattered power that is a simple additive process. Two other statistical properties of the scattered signal are important to us: 1) The time correlation function of the scattered electric field at the observation point P, which according to the Wiener-Khintchine theorem is the Fourier transform of the power spectral density of the scattered signal; 2) The spatial correlation function of the electric field at two different observation points P and P'. The time correlation function will tell us how long a laser pulse width is needed in order to reduce the statistical errors of the measurement of random quantity below certain acceptable value or, in other words, it tells us how many independent samples of the scattered signal we have for an observation time T. Since the instantaneous electric field at the observation point P depends on the instantaneous electron configuration within the scattering volume $\lambda^3 >> \lambda_c^3$, the correlation time will be of the order of (coherence length λ_c)/(characteristic electron or ion speed). The spatial coherence of the scattered signal at the receiver antenna is related to the total volume from which the scattered signal emanates. Obviously, we want to maximize the scattered power at the receiver and this means to increase

the volume of signal scattering plasma that the receiver sees: the maximum volume is determined by the focusing optics and the antenna properties of the receiver, but the method of detection will set an upper limit to the (signal)/(noise) ratio that can be achieved. For example, let us assume that all the scattered signal is focussed onto the whisker of a semiconductor mixer. Then, unless most of the signal is spatially coherent, the electric field at the detector will not increase as (effective antenna aperture) but instead will increase as (effective antenna aperture)$^{1/2}$ as do other sources of broadband plasma noise. Therefore, the intrinsic plasma (signal)/(noise) ratio will remain constant. However, if the receiver itself is the most important source of noise we will always gain in the (signal)/(noise) ratio by going into a larger aperture antenna.

Next, we will consider in more detail the scattering process that provides information about the ion temperature, i.e. Thomson scattering, which can be used as a plasma diagnostic tool. Obviously the scattering process we are interested in should reflect the ion density fluctuations. Since the plasma as a whole is neutral, the ion density fluctuations will, to some extent, be followed by the electron density fluctuations. This process will be efficient when T_e/T_i is of the order of one or less. The shielding of the charge fluctuations produces a characteristic electron plasma frequency below which no transverse EM wave can propagate inside the plasma, and a characteristic Debye shielding length which corresponds to the radius of a sphere within which most of the ion charge unbalance is neutralized. Therefore, three of the basic ingredients for a successful ion temperature measurement using electron Thomson scattering are that the scattered EM wave has a frequency higher than the plasma frequency, that the wavelength of the electron density fluctuations observed is much larger than the Debye shielding radius, and that T_{elec}/T_{ion} is of order unity or smaller.

In order to have an idea of the order of magnitude of the quantities introduced previously, we have tabulated some useful parameters in Tables I-a and I-b. In Table I-a we show typical values of the Debye shielding length and of the number of electrons within the Debye sphere. At the highest electron temperature and the lowest electron density the experiment should be designed to observe electron density fluctuations with a wavelength much larger than 2.35×10^{-4} m. If the input signal wavelength is in the submillimeter region ($\lambda_i = 0.5$ mm to 0.3 mm) the scattering angle should be less than 10 degrees. If $\lambda_i \simeq 10$ μm (CO_2 laser) the scattering angle should be a fraction of a degree. In Table I-b we show the values of the correlation time for a Gaussian spectrum of varying bandwidth. For the plasma parameters of interest to us $\tau_c \leq 1$ nsec.

The qualitative considerations of this section serve the purpose to focus attention in a number of problems that will be quantified in the remaining sections of this report, and that will allow us to state more precisely the requirements for a successful ion temperature plasma diagnostic scheme.

THOMSON LASER LIGHT SCATTERING BY PLASMAS: QUANTITATIVE RESULTS

In the previous section we put forward a very qualitative argument that showed that EM radiation will be emitted from a plasma, whether it is irradiated with externally produced EM radiation or not. Measurement of the properties of the EM radiation emitted by the plasma has been and it will continue to be an extremely useful plasma diagnostic tool. Obviously, for any kind of plasma diagnostic the quantity that is being measured should have sufficient amplitude and last for a sufficient amount of time so it can be separated from other coexistent EM radiation and the ever present instrumental and statistical noise. It is the purpose of this section to provide a quantitative estimate of the amount of EM radiation scattered from an intense laser beam by plasmas under a variety of conditions that we expect will be encountered in various plasma producing and confining machines. It must be understood that the details of the scattered signal will be strongly dependent on the characteristics of the plasma associated with a given machine, i.e. the existence of an externally applied magnetic field, plasma instabilities and turbulence, plasma drift, plasma heating method, whether equilibrium conditions have been achieved or the plasma distribution function is non-Maxwellian and/or suprathermal electrons are present, etc. Clearly, these machine dependent plasma characteristics cannot be predicted ahead of time, but if any plasma diagnostic is to be of any utility it should provide an indication of suitable telltale signs if the plasma is not behaving according to expectations. For Thomson scattering the spectral distribution of the scattered energy is the most important characteristic that we are interested in knowing.

For nonrelativistic Maxwellian plasmas the scattering spectral function is well known. When these plasmas are subjected to an external magnetic field, the spectral function becomes modulated with the period of the cyclotron frequency and the overall scattered power may or may not be appreciably affected. However, when plasma instabilities set in and/or a high degree of plasma turbulence is present the electron density fluctuations increase many fold and so does the scattered power. Therefore, if we design the apparatus to detect the scattered signal from a Maxwellian, unmagnetized plasma, we will certainly be able to observe other plasma conditions. Consequently, in this section we will determine the characteristic dependence of the scattered power spectral density on the density fluctuations for a Maxwellian, unmagnetized plasma, and in subsequent sections we will determine the requirements necessary for the apparatus so the spectral density can be reconstructed within a certain accuracy. If the electron temperature is much smaller than the ion temperature (which is the condition for the SUMMA machine at NASA LRC) the spectral density alone will suffice to determine the ion temperature uniquely. However, for most other machines the ratio T_e/T_i is of order one, and further independent information about the electron temperature is necessary in order to determine the ion temperature. It will also become apparent that highly ionized, heavy atomic impurities (like iron) in hydrogen, deuterium, tritium or helium plasmas are readily detectable because of their characteristically intense and narrow spectral feature superimposed on the ion feature spectrum.

In Fig. 3 we sketch an idealized Thomson scattering experiment. The beam of a high power laser is focussed by means of L_1 into a convenient region of the plasma confined in a vacuum chamber. A small fraction of the incoming laser beam is scattered by the plasma electrons and the remaining energy is directed into a laser beam dump where, ideally, it is totally absorbed. A fraction of the scattered energy is collected by L_2 and focussed into a detector. At the detector the scattered

9

signal is transformed into some suitable electrical response which can be further processed in order to obtain the spectral power density of the scattered signal.

Figure 4 shows a block diagram of the components necessary for a Thomson scattering experiment. We will treat them separately in later sections. The scattering geometry is shown in Fig. 5. A transverse EM wave propagating along the z-axis with a wavevector $\bar{k}_i$, angular frequency ω_i, and linearly polarized with an electric vector $\bar{E}_i$, is scattered at the point O. The scattered signal is observed at the point P far away from the scattering center O. The transverse EM wave observed at P has a wavevector $\bar{k}_s$, frequency ω_s, and electric field $\bar{E}_s$.

To gain an appreciation for the scattering problem it will be necessary to go into some detail into the derivation of the equation for the scattered power spectral density. However, the amount of detail we provide will only sketch the crucial steps where the physical understanding come in and the sometimes lengthy algebraic details necessary to obtain the final results will be avoided. In accord with this approach we will dispense with details that, although important for the analysis of specific situations, do not add anything conceptually new. Therefore, we will consider a nonrelativistic, unbounded, collisionless, unmagnetized, isotropic, multicomponent plasma. Even with these simplifications we are faced with a complicated many-body problem and further approximations and a variety of different approaches have been used by different authors. A very incomplete list of references[1-9] can be found in the Bibliography section of this report. Also a number of books[10-13] and conference proceedings[14, 15] contain an impressive collection of results; we have found the books by Bekefi[10] and by Sheffield[11] most useful in the preparation of this report.

Since magnetic effects are being neglected entirely, the electric polarization $\bar{P}$ will be the sole source of radiation. Let us separate $\bar{P}$ into an average part

$\langle \overline{P} \rangle$ and a fluctuating part $\delta \overline{P}$, [16]

$$\overline{P} = \langle \overline{P} \rangle + \delta \overline{P} \tag{1}$$

We are interested in transverse EM waves, hence the average polarization is given by

$$\langle \overline{P} \rangle = \varepsilon_0 (K_T - 1) \overline{E}_i \tag{2}$$

where K_T is the transverse dielectric coefficient and $\overline{E}_i$ is the electric field vector of the EM wave propagating in the plasma.

For radiation with angular frequency $\omega_i > \omega_{pe}$, where $\omega_{pe} = (N_e e^2 / \varepsilon_0 m_e)^{1/2}$ is the electron plasma frequency, the polarization is local and the wave damping is negligible. Then

$$K_T - 1 \simeq - \omega_{pe}^2 / \omega_i^2 = - N_e e^2 / \varepsilon_0 m_e \omega_i^2 \tag{3}$$

Therefore, the fluctuating part of the polarization in Eq. (1) is proportional to the electron density fluctuations. [1]

$$\delta \overline{P} (\overline{r}, t) \simeq - \varepsilon_0 \frac{\delta N_e (\overline{r}, t)}{N_e} \frac{\omega_{pe}^2}{\omega_i^2} \overline{E}_i (\overline{r}, t) \tag{4}$$

Using Maxwell equations it can be shown that the wave equation for the electric field vector is

$$\nabla \times \nabla \times \overline{E}_s + \frac{1}{c^2} \frac{\partial^2 \overline{E}_s}{\partial t^2} = -\mu_0 \frac{\partial^2}{\partial t^2} \delta \overline{P}, \tag{5}$$

where the polarization $\delta \overline{P}$ is the source of the scattered radiation.

For the infinite domain this equation is easily solved with the use of the Fourier space and time transform. The transformed equation is

$$\overline{k}_s \times \overline{k}_s \times \overline{E}_s(\overline{k}_s, \omega_s) + \frac{\omega_s^2}{c^2} \overline{E}_s(\overline{k}_s, \omega_s) = - \mu_0 \omega_s^2 \delta \overline{P}(\overline{k}_s, \omega_s) \tag{6}$$

11

where $\bar{k}_s$ and ω_s are the wavevector and angular frequency of the scattered field $\bar{E}_s$, and the Fourier transform pair we use is

$$\tilde{E}(\bar{k}, \omega) = (2\pi)^{-2} \int d\bar{r} \int dt \, e^{-i(\omega t - \bar{k} \cdot \bar{r})} \bar{E}(\bar{r}, t) \tag{7}$$

$$\bar{E}(\bar{r}, t) = (2\pi)^{-2} \int d\bar{k} \int d\omega \, e^{i(\omega t - \bar{k} \cdot \bar{r})} \tilde{E}(\bar{k}, \omega). \tag{8}$$

This symmetrized form of the Fourier transform is not used in Ref. (11) and, consequently, results may differ by a power of (2π) from Sheffield's.

Using Eq. (4), and assuming that the incoming EM wave is a plane wave, i.e.,

$$\bar{E}_i(\bar{r}, t) = \bar{E}_{io} \, e^{i(\omega_i t - \bar{k}_i \cdot \bar{r})} \tag{9}$$

the Fourier transform of $\delta \bar{P}$ is

$$\delta \bar{P}(\bar{k}_s, \omega_s) = - \frac{\epsilon_o}{N_e} \frac{\omega_{pe}^2}{\omega_i^2} \bar{E}_{io} \int d\bar{r} \int dt \, e^{-i(\omega_s t - \bar{k}_s \cdot \bar{r})} \, e^{i(\omega_i t - \bar{k}_i \cdot \bar{r})} \delta N_e(\bar{r}, t)$$

$$= - \frac{4\pi r_o}{\mu_o \omega_i^2} \bar{E}_{io} \, \delta N_e \left[(\bar{k}_s - \bar{k}_i), (\omega_s - \omega_i) \right] \tag{10}$$

where $r_o = \mu_o e^2 / 4\pi m_e$ is the classical electron radius.

The solution of Eq. (6) is straightforward

$$\bar{E}_s(\bar{k}_s, \omega_s) = - \frac{\delta \bar{P}(\bar{k}_s, \omega_s)}{\epsilon_o} - \frac{\bar{k}_s \times [\bar{k}_s \times \delta \bar{P}(\bar{k}_s, \omega_s)]}{\epsilon_o k_s^2 \left[1 - \frac{\omega_s^2}{c^2 k_s^2} \right]} \tag{11}$$

12

The far field approximation corresponds to the second term in the right hand side of Eq. (11). Since the phase velocity of the EM wave in the plasma is equal to $\omega_s / k_s = c/\sqrt{K_T}$, then

$$\bar{E}_s(\bar{k}_s, \omega_s) \simeq \frac{4\pi c^2 r_0}{\omega_i^2} \quad \delta N_e(\bar{K}, \Omega) \left[\frac{\bar{k}_s \times (\bar{k}_s \times \bar{E}_{io})}{\left(k_s^2 - \frac{\omega_s^2}{c^2} \right)} \right] \quad (12)$$

where $\bar{K} = \bar{k}_s - \bar{k}_i$, $\Omega = \omega_s - \omega_i$, and we will assume that $\omega_s^2/\omega_i^2 \approx 1$ and $K_T \approx 1$. Therefore, the radiation part of the scattered electric field is the product of two Fourier transforms in $\bar{k}_s$-space. Hence it is the convolution of the two functions in $\bar{R}$-space. Working out the algebra we obtain

$$\bar{E}_s(\bar{R}, \omega_s) \simeq r_0 \left[\frac{\omega_s^2}{\omega_i^2} \right] \frac{e^{-ik_s R}}{R} \quad (2\pi)^{3/2} \quad \delta N_e(\bar{K}, \Omega) \quad \hat{k}_s \times (\hat{k}_s \times \bar{E}_{io}) \quad (13)$$

where the scattering wave vector is defined by the relation

$$\bar{k}_s = \frac{\omega_s}{c} \hat{R} , \quad (14)$$

$\hat{R} = \bar{R}/|\bar{R}|$, defines the direction of propagation of the scattered wave, $R = |\bar{R}|$, and $\hat{k}_s = \bar{k}_s/|\bar{k}_s|$.

The equation that relates the scattered electric and magnetic field is

$$\nabla \times \bar{E}_s = -\mu_0 \frac{\partial \bar{H}_s}{\partial t} . \quad (15)$$

Taking the time Fourier transform of Eq. (15) and retaining only the far field component we obtain

$$\bar{H}_s(\bar{R}, \omega_s) \simeq \left[\frac{\epsilon_0}{\mu_0} \right]^{1/2} r_0 \frac{\omega_s^2}{\omega_i^2} \frac{e^{-ik_s R}}{R} (2\pi)^{3/2} \delta N_e(\bar{K}, \Omega) \hat{k}_s \times [\hat{k}_s \times (\hat{k}_s \times \bar{E}_{io})] \quad (16)$$

13

The time average of the Poynting vector over a time interval T, and per unit angular frequency interval $d\omega_s$ is

$$\bar{S}_T(\bar{k}_s, \omega_s) = \left[\frac{\varepsilon_o}{\mu_o}\right]^{1/2} r_o^2 \left[\frac{\omega_s}{\omega_i}\right]^4 (2\pi)^3 \frac{(\delta N_e)(\delta N_e^*)}{2T} \frac{\hat{k}_s}{R^2} \mid \hat{k}_s \times (\hat{k}_s \times \bar{E}_{io}) \mid^2 . \qquad (17)$$

The power flow through an area $dA = R^2 d\Omega$, located at a distance $R >> \lambda$ (dimensions of the source) and subtending a solid angle $d\Omega$ is then

$$P_s(\bar{k}_s, \omega_s) \, d\omega_s = P_I \, \ell r_o^2 \, \frac{\omega_s^4}{\omega_i^4} \, (d\Omega) \, \frac{d\omega_s}{2\pi} \, N_e \, \frac{(2\pi)^4 (\delta N_e)(\delta N_e^*)}{T V N_e} \mid \hat{k}_s \times (\hat{k}_s \times \hat{E}_{io}) \mid^2 \qquad (18)$$

where $P_I = \frac{1}{2} \left[\frac{\varepsilon_o}{\mu_o}\right]^{1/2} \mid E_{io} \mid^2 A$ is the laser incoming power over an area A of the plasma, and $V = \ell A$ is the volume of plasma of length ℓ from which the scattering is observed.

This result applies to a particular realization of the random fluctuations spectrum. If the observation of the scattered power is performed over a long period of time, $T \to \infty$, then we will measure an average over all possible electron density random fluctuations realizations that the plasma can have.

Let us define the power spectrum density function as the following ensemble average

$$S(\bar{K}, \Omega) = \lim_{\substack{T \to \infty \\ V \to \infty}} \left\langle \frac{(2\pi)^4 \mid \delta N_e(\bar{K}, \Omega) \mid^2}{T V N_e} \right\rangle \qquad (19)$$

where the factor of $(2\pi)^4$ arises from our symmetrical definition of the space-time Fourier transform. The average scattered power is then

$$\langle P_s(\bar{k}_s, \omega_s) \rangle \, d\omega_s \simeq r_o^2 P_I \, \ell N_e \, (d\Omega) \, \frac{d\omega_s}{2\pi} \, S(\bar{K}, \Omega) \mid \hat{k}_s \times (\hat{k}_s \times \hat{E}_{io}) \mid^2 \qquad (20)$$

With the scattering geometry shown in Fig. 5, the geometrical factor for the dipole radiation is

$$\left| \hat{k}_s \times (\hat{k}_s \times \hat{E}_{io}) \right|^2 = 1 - \sin^2\theta \, \cos^2(\phi - \phi_0), \tag{21}$$

and the $\hat{x}$, $\hat{y}$ and $\hat{z}$ components of the scattered electric field $\bar{E}_s$ (Eq. 13) are proportional to

$$\hat{x}: \quad \sin^2\theta \, \cos\phi \, \cos(\phi - \phi_0) - \cos\phi_0 \tag{22a}$$

$$\hat{y}: \quad \sin^2\theta \, \sin\phi \, \cos(\phi - \phi_0) - \sin\phi_0 \tag{22b}$$

$$\hat{z}: \quad \sin\theta \, \cos\theta \, \cos(\phi - \phi_0) \tag{22c}$$

The maximum scattered power (regardless of the scattering angle θ) is obtained when $\phi - \phi_0 = \pi/2$. This condition can be achieved if the power laser electric field is polarized along the y-direction ($\phi_0 = \pi/2$), the scattering vector $\bar{k}_s$ is in the x-z plane ($\phi = 0$), and the receiving antenna is polarized along the y-axis. In Section 3 we present calculations of the scattered power for these conditions for a simple, two component plasma.

Equations (13), (19) and (20) are very important. They relate the scattered electric field with the plasma density fluctuations, and the average scattered power with the ensemble average of the square of the electron density fluctuations with wavevector $\bar{K}$ and frequency Ω.

At this point we must remark that, although we have exhibited the intended relationship between the scattered field and the plasma density fluctuations, we have been very cavalier when taking the space-time Fourier transform of stochastic variables over infinite time and space. However, as it was done by Dougherty and Farley,[2] the analysis can be made more rigorous if we consider a finite volume

15

that repeats periodically over the whole space and a time dependence that is a periodic function of time, and later take the limit of these periods to infinity.

The density fluctuation that appears in Eq. (12) is a stochastic variable which is calculated for a large number of electrons. Hence, we will have a sum over a large number of stochastic variables and, because of the central limit theorem of probability, [17] the probability distribution of $\bar{E}_s$ will be Gaussian. This result will be used later on when calculating the statistical errors associated with the spectral measurement.

We must notice that in Eqs. (13), (19) the source of the fluctuations is irrelevant to the physics of the scattering. In a plasma machine there exist a variety of normal modes that will share the energy that excites them. For the idealized plasma we are considering, the thermal energy is shared by the transverse and the longitudinal plasma waves. The dispersion relations that determine these modes are: [14]

$$k^2 c^2 = \omega^2 K_T(\bar{k}, \omega),$$
(23a)

$$K_L(\bar{k}, \omega) = 0.$$
(23b)

Here, the longitudinal dielectric coefficient is

$$K_L(\bar{k}, \omega) = 1 + \sum_\alpha \frac{\omega_{p\alpha}^2}{k^2} \int \frac{\bar{k} \cdot \nabla_v f_\alpha(\bar{v})}{\omega - \bar{k} \cdot \bar{v} - i0^+} \, d\bar{v}$$

$$= 1 + \sum_\alpha \frac{\omega_{p\alpha}^2}{k^2} \left[P \int \frac{\bar{k} \cdot \nabla_v f_\alpha(\bar{v})}{\omega - \bar{k} \cdot \bar{v}} \, d\bar{v} + i\pi \int d\bar{v} \, \delta(\omega - \bar{k} \cdot \bar{v}) \, \bar{k} \cdot \nabla_v f_\alpha(\bar{v}) \right]$$
(24)

where $\omega_{p\alpha}$ and $f_\alpha(\bar{v})$ are the plasma frequency and the velocity distribution function of the α - specie, $P \int$ denotes the principal value of the integral, and the imaginary part is the Landau damping term.

For the Maxwellian velocity distribution

$$f_\alpha(v) = (m_\alpha/2\pi kT_\alpha)^{3/2} e^{-m_\alpha v^2/2kT_\alpha} \tag{25}$$

the longitudinal dielectric coefficient is

$$K_L(\overline{k}, \omega) = 1 + \sum_\alpha \frac{\omega_{p\alpha}^2}{\omega^2} \Phi_\alpha(x_\alpha), \tag{26}$$

where

$$\Phi_\alpha(x_\alpha) = 2x^2\left[1 - 2xe^{-x^2}\int_0^x e^{t^2}\,dt - i\sqrt{\pi}\,xe^{-x^2}\right], \tag{27}$$

$$x = \omega/\sqrt{2}\,kv_o, \tag{28}$$

and

$$v_o = (kT_\alpha/m_\alpha)^{1/2}. \tag{29}$$

According to Bekefi[14] the ratio of the thermal energy content of the longitudinal modes (with a typical phase velocity v_o) to the transverse modes (with a phase velocity $\geq c$) is approximately equal to $(c/v_o)^2 \gg 1$, and we are justified in neglecting the effect of the transverse fluctuations in the scattered energy. Therefore, the Thomson scattering from thermal electron density fluctuations in a __stable plasma__ is due entirely to longitudinal electrostatic modes with the dispersion relation given by Equation (23b).

Several procedures have been used to calculate the ensemble average that appear in Eq. (19) for the longitudinal fluctuations. Dougherty and Farley[2] have used the fluctuation-dissipation theorem [18] (which relates thermal fluctuations with the dissipative component of a suitable linear response function to an external perturbation) to obtain the thermal average $\langle |\delta N_e|^2 \rangle$ from the known Landau damping for the

longitudinal modes. Rosenbluth and Rostoker[9] start with the equations of motion for the plasma distribution function (for a plasma with unequal electron and ion temperatures, a constant applied magnetic field, and electron drift relative to the ions) and obtain more general results that reduce to those of Ref. 2 in the suitable limits.

Figures 6 and 7 are taken from Rosenbluth and Rostoker[9]. Figure 6 shows the typical behavior of the scattered radiation [which is an even function of $(\omega_s - \omega_i)$] for various electron and ion temperatures. If $T_e/T_i << 1$, which is the case for the SUMMA machine,[19,20] the scattered radiation will fall off like a Gaussian dominated only by the ion temperature. For $T_e/T_i \sim 1$ the scattered intensity is a maximum for $|\omega_s - \omega_i| \neq 0$, and this behavior is very much pronounced when $T_e/T_i >> 1$. In the latter case the power scattered in the central ion feature is very much decreased and the thermal longitudinal fluctuations are not as useful to provide a measure of T_i. For more details the reader should consult Ref. (9). In Fig. 7 is shown the case when the electrons have a net drift velocity relative to the ions. The important feature here is that the scattered energy is not symmetric as a function of $(\omega_s - \omega_i)$.

Figures 6 and 7 make clear that the ion feature of the Thomson scattering, from thermal fluctuations of a plasma with $T_e/T_i << 1$ or with $T_e/T_i \sim 1$, is reproduced adequately (for the ion temperature measurement purposes) if the total frequency bandwidth of the receiver is limited to the value that includes the two points in the scattered power spectrum for which the ratio of the intensity at the wings is one tenth of the intensity at the center of the ion feature.

Because the ion feature of the scattered signal may be asymmetric it is important that we use a heterodyne receiver, i.e. f_{LO} (frequency of the local oscillator) $\neq f_L$ (frequency of the laser). This technique has two advantages: 1) It allows to select the center frequency, f_{IF}, of the IF amplifier at a convenient value so its low-noise characteristics are optimal; 2) Also, f_{IF} may be selected in a frequency band where further signal processing can be carried out with available

18

low noise hardware. The frequency response of the IF amplifier must be tailored so that only the 10 db bandwidth necessary to estimate the ion feature is passed. Of course, because the laser lines available for the local oscillator cover a discrete range of suitable values, the choice of f_{LO} should be made with great care. References 21 and 22 list several hundred laser lines from which to choose a suitable LO.

If the ion feature is symmetric or if its asymmetry is of no interest, a homodyne detector ($f_{LO} = f_L$) may be adequate. However, the noise temperature of the best IF amplifier with a 100 MHz - 1 GHz band pass may be much larger than the noise temperature of a good parametric amplifier with a 10 GHz - 12 GHz band pass. This is an important consideration since for the submillimeter mixers that will become available in the forseeable future, the IF amplifier contribution to the total noise is significant.

Before concluding this section we will consider semiquantitatively the effect of a finite plasma scattering volume on the wavevector conservation relation $\bar{K} = (\bar{k}_s - \bar{k}_i)$.

Let us recall that to derive Eq. (13) we have assumed an incoming plane wave of infinite extent scattering from an infinite volume plasma. Hence, when we encounter integrals over the space coordinates, like in Eq. (10), wavevector conservation is rigorously satisfied. However, the field of view of the receiver is finite and the incident laser beam is not an infinite plane wave, which means that the electric field $\bar{E}_s$ of the scattered wave is made up of contributions from a finite plasma volume and that the incoming wavevector $\bar{k}_i$ is not sharply defined. Since the Fourier transform of the electron density fluctuations is calculated for the whole plasma volume, then a number of $\bar{K}$ vectors will contribute to the value of $\bar{E}_s$ [Eq. (13)] thereby making the wavevector conservation condition $\bar{k}_s = (\bar{K} + \bar{k}_i)$ an ill defined relation.

There are two factors that make an approximate solution of this problem easier to handle: 1) The plasma scattering volume is finite but relatively large

(of the order of a few cubic centimeters); 2) The receiver has a finite solid angle of acceptance (of the order of a few millisteradians). We then expect that for a given value of $\bar{k}_s$ [Eq. (14)] the wavevector conservation relation, although not rigorously true, will be a rather sharply defined function whose width will shrink to zero as the scattering volume increases to infinity. Also, we always measure the scattered radiation falling on a finite solid angle $\Delta\Omega$. This allows us to approximate the problem as follows: we expand the convolution integral that takes us from Eq. (12) to Eq. (13) into a complete set of suitable orthogonal functions adequate for the integration volume. (For example, for a scattering volume in the shape of a rectangular prism, we can expand in terms of plane waves with wavevectors $k_x = 2\pi N_1/L_x$; $k_y = 2\pi N_2/L_y$; $k_z = 2\pi N_3/L_z$.) Hopefully, only the few terms in the expansion for which the wavevector conservation relation is approximately satisfied will contribute significantly. Therefore, we can associate with the vector $\hat{R}$ a nearby wavevector $\bar{k}_s = (k_x, k_y, k_z)$.

Since the $\bar{k}_s$'s are distributed over a discrete array of points in wavevector space, there is associated with each $\bar{k}_s$ an angular spread over which mostly one $\bar{K}$ will contribute. This angular spread is called the coherence solid angle because mostly one electron density fluctuation wavevector $\bar{K}$ contributes to the scattered signal. Since different wavevectors $\bar{K}$ are mostly uncorrelated, we may not gain any signal/noise advantage (when detecting one given fluctuation wavevector) by using a larger solid angle of acceptance for the receiver. If the acceptance angle is very much larger than the coherence angle we have a radiometer where the information about any one $\bar{K}$ is scrambled with information about many other $\bar{K}$-vectors at the receiver.

For a scattering volume in the shape of rectangular prism, the volume per point in k_s-space is given by

$$k_s^2 \, \Delta k_s \, \Delta\Omega_{coh} \simeq \frac{(2\pi)^3}{L_x L_y L_z} \tag{30}$$

20

where we have equated volume elements in spherical and rectangular coordinates.

Here

$$k_s^2 = (2\pi)^2/\lambda_s^2 \, ;$$

$$\Delta \vec{k}_s = \hat{x} \frac{2\pi}{L_x} + \hat{y} \frac{2\pi}{L_y} + \hat{z} \frac{2\pi}{L_z} \, ;$$

and

$$\Delta k_s \simeq \Delta \vec{k}_s \cdot \hat{k}_s = 2\pi \left(\frac{\sin\theta \cos\phi}{L_x} + \frac{\sin\theta \sin\phi}{L_y} + \frac{\cos\theta}{L_z} \right)$$

Finally

$$\Delta\Omega_{coh} \simeq \frac{\lambda_s^2}{L_y L_z \sin\theta \cos\phi + L_x L_z \sin\theta \sin\phi + L_x L_y \cos\theta} \, . \tag{31}$$

For example, if $\theta = 30°$; $\phi = 0°$; $L_x = L_y \simeq 1.4$ cm (Section 7); $L_z = 0.97$ cm (Table VI); $\lambda_s \simeq 385\,\mu m$; then $\Delta\Omega = 5.9 \times 10^{-3}$ sr (Table VI), and $\Delta\Omega_{coh} \simeq 0.6 \times 10^{-3}$ sr.

Since $\Delta\Omega/\Delta\Omega_{coh} \simeq 10$, we are measuring the contribution from ten neighboring $\vec{K}$ vectors and the receiver is operating in the radiometer mode, i.e. the electric field at the mixer diode is the sum of ten random electric fields, and its amplitude increases as $(\Delta\Omega/\Delta\Omega_{coh})^{1/2} \simeq 3.16$.

This is important in heterodyne detection since the output of the mixer increases only as the square root of the effective area of the antenna, while if $\Delta\Omega/\Delta\Omega_{coh} \leq 1$ then the output of the mixer increases proportionally to the collection area of the antenna. Therefore, it is very important to focus the power of the laser beam into as small a spot as possible to improve the mixing efficiency.

SECTION 3

MODEL CALCULATIONS FOR A SIMPLE PLASMA

A. ESTIMATE OF SCATTERING SIGNAL

In this section we collect the numerical results obtained for the simple, unmagnetized plasma discussed in Section 2. Here, we use the results and notation of Ref. 11, Chapters 6 and 7. The power collected by a receiver per unit frequency interval, which subtends a solid angle $\Delta\Omega$ and sees a length ℓ of plasma (measured along the laser beam) is given by

$$P_s(\bar{E}_s, \omega_s) = P_i N_e r_o^2 \ell \Delta\Omega \; |\hat{k}_s \times (\hat{k}_s \times \hat{E}_{io})|^2 \; S(\bar{R}, \Omega) \tag{1}$$

where

$$\bar{R} = \bar{k}_s - \bar{k}_i$$

$$\Omega = \omega_s - \omega_i$$

$$f_i = 604 \text{ GHz}$$

$$\omega_\alpha = k_\alpha c \; (\alpha = i \text{ or } s)$$

$$P_i = 10^6 \text{ W is the incident laser power}$$

$$N_e = 10^{20} \text{ m}^{-3} \text{ is the average electron density}$$

$$\ell \Delta\Omega = 10^{-4} \text{ m sr}$$

$$r_o = \mu_o e^2/4\pi m_e \simeq 2.82 \times 10^{-15} \text{ m is the classical electron radius}$$

and $S(\bar{R}, \Omega)$ is given by

$$S(\bar{R}, \Omega) = (2\pi^{1/2}/Ka)(A_e + A_i)/|\epsilon_o|^2 \tag{2}$$

where

$$A_e = \exp(-x_e^2)\left[\left\{1+\alpha^2 Z \frac{T_e}{T_i} Rw(x_i)\right\}^2 + \left\{\alpha^2 Z \frac{T_e}{T_i} Iw(x_i)\right\}^2\right] \quad (3)$$

$$A_i = Z \left[\frac{m_i T_e}{m_e T_i}\right]^{1/2} \exp(-x_i^2)\left[\left\{\alpha^2 Rw(x_e)\right\}^2 + \left\{\alpha^2 Iw(x_e)\right\}^2\right] \quad (4)$$

$$|\epsilon|^2 = \left\{\left[1+\alpha^2\left\{Rw(x_e) + Z \frac{T_e}{T_i} Rw(x_i)\right\}\right]^2 \right.$$
$$\left. + \left[\alpha^2 Iw(x_e) + \alpha^2 Z \frac{T_e}{T_i} Iw(x_i)\right]^2\right\} \quad (5)$$

$$x_e = \Omega/Ka \quad (6)$$

$$x_i = \Omega/Kb \quad (7)$$

$$\alpha = 1/K L_D \quad (8)$$

$$a = (2 k_B T_e/m_e)^{1/2} \quad (9)$$

$$b = (2 k_B T_i/m_i)^{1/2} \quad (10)$$

$$Iw(x) = \pi^{1/2} x \exp(-x^2) \quad (11)$$

$$\text{and } Rw(x) = 1 - 2 x \exp(-x^2) \int_0^x d\phi \exp(p^2) \quad (12)$$

Numerical calculations for a hydrogen plasma were performed for a variety of scattering angles θ, and electron and ion temperatures, T_e and T_i respectively. These results should not be taken as an absolute measure of the scattered signal expected, but only to provide a qualitative measure of the signal available. This should be useful for comparison with the plasma noise and the detector noise, and in this way meaningful specifications can be set for the SMM laser and receiver.

23

The numerical results have been plotted in Figures 8 through 22 and are very useful to determine design parameters and to weight the tradeoffs between conflicting requirements.

In Figure 8 we plot the value of α_0, determined using Eq. (8) for $\omega_s = \omega_i$. The plotted values can be scaled to other frequencies and densities because $\alpha_0 \simeq N_e^{1/2}/f_i$. In order to have most of the scattered energy coming from the ion feature, the value of α_0 must be larger than three. This condition is satisfied if the scattering angle is small.

However, practical considerations place a lower limit on θ. For small diameter plasmas (SUMMA, Alcator A) the SMM laser beam divergency will set a lower limit. For large volume plasmas (TFTR) beam defocussing by the density gradients will set the lower limit on θ. Also the dimensions of the laser beam dump and the receiver dump, and the mechanical details of the plasma machine will set values for θ_{min}. For the SUMMA, Alcator A and C, and the TFTR machines a value of $20^o \leq \theta \leq 30^o$ is practical.

In Figures 9 through 12 the scattered power at the center of the ion feature per unit frequency interval, S_0, is plotted as a function of the scattering angle θ. The range of T_e and T_i covers the SUMMA machine ($T_e/T_i << 1$, $T_i \leq 3$ KeV) and TFTR ($T_e/T_i = 0.5, 1, 2$, $T_e \leq 6$ KeV). The values of S_0 scale with the SMM laser input power $\bar{P}_i$ and with the product $L \, \delta\Omega$ (1 MW and 10^{-4} m sr in the calculations). If we assume a collection optics efficiency of 10%, we will collect 10^{-17} W/Hz at the center and 10^{-18} W/Hz at the wings for the SUMMA machine (Fig. 12). The power spectral density of the scattered signal will be superimposed on other noise sources. As we will show later on, the plasma bremsstrahlung and synchrotron radiation noise can be neglected except for the largest plasma volume, high magnetic field, and high T_e machines. Therefore, only the receiver noise need to be considered. The shape of the scattered power density can be extracted well

from the statistical noise of the measurement (Section 4) if we limit the receiver noise at the input to be less than or equal to the scattered power density at the wings, i.e., $kT_{eff} \leq 10^{-18}$ W/Hz. Receivers with this noise level have just become available (MIT-Lincoln Laboratory, and JPL) in the 600 GHz frequency band. The receiver requirement becomes more difficult to satisfy in large Tokamaks (i.e. TFTR). Here $S_0 \simeq 10^{-17}$ W/Hz for $T_e/T_i \simeq 1$ and $T_e \simeq 4$ Kev (Figs. 9 - 11). The same consideration as before require $kT_{eff} \leq 10^{-19}$ W/Hz for the receiver.

In Figures 13 through 16 we plot the total bandwidth, BW, between the - 10 db points (S_0 is the reference) in the scattered power density. The receiver bandwidth decreases with the scattering angle θ, and increases with T_i ($T_e/T_i \ll 1$) or T_e ($T_e/T_i \sim 1$). For SUMMA with $T_i \leq 2$ Kev the bandwidth requirements is BW $\simeq 2$ GHz (Fig. 16). For TFTR, BW $\simeq 4$ GHz (Figs. 13 - 15).

The bandwidth and noise requirements of the receiver can be relaxed if we can decrease the scattering angle θ. However, besides the restrictions mentioned previously about the constraint $\theta > \theta_{min}$ (because of beam divergency, refraction, and dumps) the spatial resolution of the measurement is decreased when going to smaller values of θ.

For a given scattering angle, the bandwidth (BW) of the receiver increases with the input frequency, and the scattered power density S_0 decreases, since the total scattered energy does not change much when $\alpha_0 > 1$. At present the most promising SMM power lasers are the CH_3F with $f_i \simeq 604$ GHz and D_2O with $f_i \simeq 780$ GHz. Therefore in Fig. 17 we have plotted the receiver bandwidth as a function of θ for the frequencies 604 GHz, 800 GHz and 1000 GHz for various energies.

Since the aperture of the receiver optics is finite and collects scattered signals over an angle $\Delta\theta$ centered on the scattering angle θ, it is important to know by how much the power spectral function will be distorted by the finite aperture. We have calculated this effect as follows. The power spectral density for small deviations

from θ can be expanded in a Taylor series

$$S(\theta + \epsilon) = S(\theta) + S'(\theta) \epsilon + \frac{1}{2} S''(\theta) \epsilon^2 + \dots \qquad (13)$$

where $S'(\theta) = \frac{dS}{d\theta}$, and $S''(\theta) = \frac{d^2 S}{d\theta^2}$.

The average of $S(\theta)$ over the aperture $\Delta\theta$ is

$$\bar{S}(\theta) = \frac{1}{\Delta\theta} \int_{-\Delta\theta/2}^{+\Delta\theta/2} d\epsilon\, S(\theta + \epsilon) = S(\theta) \left\{ 1 + \frac{S''(\theta)}{24\, S(\theta)} (\Delta\theta)^2 + \dots \right\} \qquad (14)$$

The fractional distortion

$$d = \frac{\bar{S}(\theta) - S(\theta)}{S(\theta)\, (\Delta\theta)^2} = \frac{S''(\theta)}{24\, S(\theta)} \qquad (15)$$

is tabulated in Tables II, III, and IV for several scattering angles θ and plasma temperatures.

We find that for $\theta = 30^{\circ}$ a SUMMA plasma with $T_e/T_i << 1$ and $T_i = 2000$ eV will have a worst spectral density distortion at about 3/4 way into the wings of 2×10^{-4} (degrees^{-2}) (Table IV). Hence if $\Delta\theta \simeq 5^{\circ}$, the measured spectral density will deviate from the ideal one by less than 0.5%. However, this value increases very fast for smaller values of θ.

For a Tokamak plasma with $T_e/T_i = 1$ and $T_i = 4000$ eV the worst distortion occurs at the wings and for the same scattering parameters as before ($\theta = 30^{\circ}$ and $\Delta\theta = 5^{\circ}$) we obtain a value of 3% (Table III).

These results show that for small angle scattering we may not gain as much signal as indicated in Figs. 9 through 12 because we must reduce the receiver aperture in order to obtain a faithful reproduction of the spectral density.

26

The numerical calculations we have discussed so far were made for a pure hydrogen plasma. This is the plasma used in all experimental plasma machines at the present time. However, fusion reactors will use deuterium and tritium plasmas. Furthermore, most plasmas are not pure but contain heavy, highly ionized impurities coming from the walls of the confinement chamber. We will now discuss qualitatively both effects.

As it was mentioned previously, the width of the ion feature is related to the Doppler shift of the scattered radiation due to the thermal velocity of the ions. Heavier ions will have a thermal velocity that decreases as the square root of the ion mass, hence the bandwidth of the ion feature will also decrease by the same factor. This is not a major effect, i.e., for a tritium plasma, the bandwidth will decrease by 40% compared to the hydrogen plasma and the intensity of the ion feature will increase accordingly. As long as the frequency resolution is adequate the Thomson scattering diagnostic will accommodate these various plasmas well. On the other hand heavy, highly ionized impurities (like Fe, Co and Mn) will contribute a very narrow and intense ion feature. These features will distort the central position of the main plasma ion feature, and we can use this effect to diagnose the presence of impurities. However, as indicated in Section 4, the statistical signal/noise ratio is inversely proportional to the frequency resolution of the spectra (smaller resolution $\rightarrow$ larger S/N) and for the foreseeable future we may expect that this additional diagnostic capability will not be available. If the SMM laser power can be increased well beyond 1 MW and the pulse length stretched to 1 μsec, and at the same time maintaining good laser spectral characteristics, then the impurity diagnostic may be feasible.

To gain an appreciation of the order of magnitude involved, in Figures 18 through 21 we have plotted the values of S_o vs θ and BW vs θ for the idealized (unrealistic) plasma of Fe ions (Fe^+, Fe^{13+}, and Fe^{26+}). If the real plasma contains, let us say, hydrogen with 5% of Fe^{26+}, the value of S_o for the Fe will be scaled accordingly and superimposed on the hydrogen ion feature. The total BW will remain the same.

B. ESTIMATE OF PLASMA NOISE

The bremsstrahlung radiation from hot electrons is estimated using the results given by Bekefi (Ref. 10, pp. 87, 134-135)

$$j_\omega = 3.53 \times 10^{-56} \frac{N_e \, (m^{-3}) \, N_i \, (m^{-3}) \, Z^2}{T_e \, (eV)^{1/2}} \quad \ln \Lambda \qquad (16)$$

$$\Lambda = 2.25 \frac{e \, T_e \, (eV)}{\hbar \omega} = 5.44 \times 10^5 \frac{T_e \, (eV)}{f \, (GHz)} \qquad (17)$$

where j_ω is given in units of W/m^3-sr-Hz-polarization, N_e and N_i are the electron and the ion densities, Z is the ion charge, T_e the electron temperature and ω is the angular frequency of the emitted radiation.

For SUMMA the effective plasma volume for bremsstrahlung radiation and the solid angle of collection of the receiver are calculated in Section 6. Let us take the following upper limits for a hydrogen plasma Tokamak:

$$\Delta\Omega = 5 \times 10^{-2} \text{ sr}$$

$$\Delta V = 5 \times 10^{-5} \text{ m}^3$$

$$T_e \simeq 4 \text{ KeV}$$

$$N_e = N_i = 10^{21} \text{ m}^{-3}$$

$$Z = 1$$

and $\quad f \simeq 6 \times 10^{11} \text{ Hz}.$

Then

$$\ln \Lambda \simeq 15$$

and $\quad J_\omega = j_\omega \, \Delta\Omega \, \Delta V \simeq 2 \times 10^{-20} \text{ W/Hz-polarization at 600 GHz.}$

28

For a Tokamak, in spite of the very unfavorable parameters that we have assumed the bremsstrahlung radiation is several orders of magnitude below the expected Thomson scattered signal.

For warm electrons (SUMMA) the parameter Λ is[10]

$$\Lambda = 6.19 \times 10^4 \ \frac{T\,(eV)^{3/2}}{f\,(GHz)\,Z} \tag{18}$$

For SUMMA assume that $T_e = 40$ eV and that all other parameters are the same as in the previous example, then

$$j_\omega = 1.41 \times 10^{-19} \ W/Hz\text{-polarization at 600 GHz.}$$

Therefore, bremsstrahlung radiation in SUMMA also is negligible.

If heavy, highly ionized impurities are present in the plasma the bremsstrahlung radiation will increase by the factor

$$\sum_{\alpha=1}^{n} (N_{i\alpha}/N_e)\,Z_\alpha^2 \ .$$

For a hot electron, hydrogen plasma with a fraction $a = 0.05$ of completely ionized Fe^{26+} impurities, the bremsstrahlung radiation will increase by the factor

$$\frac{\left[(1-a)\,Z_1^2 + a\,Z_2^2\right]}{\left[(1-a)\,Z_1 + a\,Z_2\right]} = \frac{0.95 + 0.05 \times 26^2}{0.95 + 0.05 \times 26} \simeq 15 \ .$$

Even with these highly unfavorable conditions the bremsstrahlung is negligible compared with the Thomson scattered signal.

Another, more troublesome source of plasma noise is synchrotron radiation from energetic electrons. In Fig. 22 we show the frequency of the first five cyclotron harmonics versus B_o. For the SUMMA machine we do not expect this source of noise to be significant because of its small electron temperature. However,

for high energy and large volume Tokamaks plasma machines synchrotron radiation may be a limiting factor to the usefulness of the Thomson scattering diagnostic. Measurements and calculations of synchrotron radiation have been done Costley et al.,[23] by Komm,[24] and by Boyd et al.[25] The results obtained so far indicate: 1) Supra-thermal electrons give a large contribution up to high harmonic order of the cyclotron resonance for low density and small dimension plasmas; 2) For a large volume, high temperature plasmas, thermal electrons produce a larger contribution to the plasma noise than suprathermal electrons. These conditions seem to hold true if the plasma is mostly transparent to the SMM laser radiation. This, of course, must be the case for a successful Thomson scattering diagnostic. For plasma machines like the TFTR, the results of Boyd et al.[25] indicate that the wavelength 496 μm of CH_3F or the 385 μm of D_2O are adequate up to fields of 5T, electron density of 10^{20} m^{-3}, and T_e = 4 KeV. The maximum sy.. nrotron radiation density expected is $I(500 \ \mu m) \leq 10^{-11}$ W/m^2-sr-Hz-polarization. One ameliorating effect is that the receiver looks into a dump instead of a highly reflecting wall. If the reflectivity of the wall is $R \simeq 0.90 - 0.95$ then the calculated synchrotron radiation is attenuated by the factor $1/(1-R) = 10 - 20$. Also, according to the antenna theorem[26,27] for a heterodyne receiver the maximum etendue of the receiver is $\Delta \Omega \ A_{eff} = \lambda^2$, where $\Delta \Omega$ is the solid angle of acceptance and A_{eff} is the effective area of the antenna. Using the above values the received intensity will be $\leq 2.5 \times 10^{-19}$ W/Hz-polarization. Background noise of this magnitude is acceptable and will not hinder the Thomson scattering diagnostic. However, for larger Tokamaks or for operation above 5T, synchrotron raidation may become a limiting factor for the ion temperature diagnostic in which case higher frequency, more powerful SMM lasers will be required.

The above values of plasma noise should be multiplied by two to obtain the effective noise level at the signal port of the mixer (Fig. 23). The reason for this is that while the ion feature spectral width will only enter through the signal port, the

bremsstrahlung and synchrotron radiation are wideband noise sources and will also enter through the image port (image frequency) of the mixer. (Physically the two ports share the same antenna.) For this reason it is always convenient (as far as it is possible) to insert an input filter that will reject the unwanted spectral region.

SECTION 4

SIGNAL PROCESSING

In this section we will study the electrical signal present at the output of the first mixer-IF amplifier (Fig. 4), and will consider various methods to determine its power spectrum. We recall from Section 2 that the power spectrum of the Thomson scattered signal is the function that conveys some of the available information about the plasma. Once this power spectral function is known, physical models of the plasma will allow to determine some of its parameters by fitting the predicted spectra to the measured power spectrum.

In Section 3 we have presented numerical results for the spectral function based on a rather simple plasma model. Using this model it is possible to work backwards and estimate the ion temperature of the plasma. For the SUMMA machine with $T_e/T_i \ll 1$, T_i is simply related to the width of the Gaussian power spectrum. When $T_e/T_i \sim 1$, fitting the model to the experimental data is not so simple, and T_e must be known from an independent measurement. In this report we will not address ourselves to this general problem, and will only consider ways to determine the power spectrum of the scattered signal.

It is most important to keep in mind that the scattered electric field, hence the IF amplifier output signal is noise-like. Therefore, the accuracy with which the power spectra can be measured increases with square root of the time allowed for the measurement. Also, for practical reasons explained previously, the signal is bandwidth limited. We sketch in Fig. 24 the power spectra of a band limited signal centered at a frequency f_o and with bandwidth $2\Delta F$. Within this limitation the signal

can be written

$$G(t) = G_1(t) \cos(\omega_0 t) + G_2(t) \sin(\omega_0 t) \tag{1}$$

where $G_1(t)$ and $G_2(t)$ are two arbitrary functions of time with bandwidth not larger than ΔF.

According to the sampling theorem[28] such bandwidth limited signals can be uniquely reconstructed if its in-phase and quadrature amplitudes are sampled at $1/2 \Delta F$ intervals (Fig. 25). Therefore, for a signal that lasts for a time T, the minimum number of signal samples necessary for each phase is

$$N_T = T(2 \Delta F) \tag{2}$$

Each sample is a realization of a Gaussian random process with zero mean and variance σ. Since we want the power spectrum we must take the Fourier transform, but the Fourier transform of a random process is also a random process. In order to obtain an estimate of the spectrum we must average over a number of realizations of the random process (if this is possible) or we may average over a number of neighboring points in the frequency space if the spectra is a smooth function of frequency. We use the latter procedure to determine the statistical signal/noise ratio of the power spectrum.

Let us divide the frequency interval $2 \Delta F$ into R blocks, so the frequency resolution is $2 \Delta F/R$ and the number of independent samples per block is $M = T(2 \Delta F/R)$. In terms of the real and imaginary component, each sample in the frequency domain has the value $[x(\omega), y(\omega)]$, where $x(\omega)$ and $y(\omega)$ are Gaussian random variables. The estimate of the power spectrum at ω_i is given by

$$S(\omega_i) = \frac{1}{M} \sum_{j = -M/2}^{+M/2} [x^2(i+j) + y^2(i+j)]. \tag{3}$$

This is the χ^2 distribution with 2M degrees of freedom.[17] The rms signal/noise ratio is

$$S/N = (2M/2)^{1/2}$$

$$= (T 2 \Delta F/R)^{1/2}$$

$$= (N_T/R)^{1/2} \tag{4}$$

In Table V we show the optimum S/N expected when R = 10, and for T = 200 nsec and T = 1 μsec.

Sampling in the time domain the in-phase and quadrature components of the signal and performing a complex fast Fourier transform (FFT), best use is made of the available information for the estimation of the spectral function. This scheme is summarized in Fig. 26. The purpose of the second local oscillator is to make the resulting IF center frequency equal to zero. The in-phase and quadrature detectors are available in package form in the frequency range 0-25 GHz. The output of each detector may be recorded by a Tektronix R7912 transient digitizer. Each one of these units has 512 storage channels, so we can optimize for a bandwidth of 2.5 GHz. Since the transient digitizer storage time is temporary (~ 1 msec) this signal must be transferred and stored into a semiconductor memory where a first signal processing occurs. The signal is FFT in a computer and finally the power spectrum is stored and/or displayed on a CRT. Hardware cost is high with this scheme.

Other nonoptimal methods of signal processing are possible and we will discuss two of them.

The first of the nonoptimal signal processing methods is shown in Fig. 27. It is similar to the standard method used by most spectrum analyzers in the market. A variable frequency second local oscillator mixes with the incoming signal in a

34

second mixer. The $f_{IF} \approx 0$ is selected by a low pass filter. The output of the filter is routed, in synchronism with the variable frequency oscillator, to a series of sample-hold amplifiers where the resulting signal is temporarily stored. After the laser pulse is terminated the signals are processed by a logarithmic amplifier, and subsequently are digitized and stored in memory. The memory output may be used to drive a CRT display. If $2 \Delta F = 2.5$ GHz, $R = 10$ and $T \simeq 200$ nsec, as before, we must sweep the variable local oscillator by $\Delta f = 250$ MHz in $T/R = 20$ nsec. This means that the bandwidth of the low pass filter should be $BW \approx R/T \simeq 50$ MHz for the signal to rise to full amplitude in the allowed 20 nsec. The signal/noise ratio is, approximately, given by

$$S/N \approx (\Delta f/BW)^{1/2} \simeq (250/50)^{1/2} \simeq 2.2 \qquad (5)$$

Although this method is simple to implement (in theory), the $S/N = 2.2$ is very small for the Thomson scattering needs. Furthermore the rate of sweep of the local oscillator, 2.5 GHz/200 nsec $= 12,500$ MHz/μsec, is much higher than what can be achieved in practice. This method becomes more viable as the laser pulse width T is increased but, at the present time, this is beyond the proven submillimeter laser technology.

The second method, shown in Fig. 28, gains over the previous method in that all the time T is available for averaging. To accomplish all of this gain it requires a true N-channel multiplexer filter that separates the bandwidth $2 \Delta F$ into N channels, each of bandwidth $2 \Delta F/N$. If the bandwidth $2 \Delta F/N$ is idealized by a rectangular passband (impossible to achieve in practice), and each section drives a power detector and RC low pass filter, the S/N is given by[29]

$$S/N = [2 RC (2 \Delta F/N)]^{1/2} \qquad (6)$$

The filter time constant has to be chosen so the signal rises to close to full amplitude

during the time T of the pulse. If we choose $RC \approx T/3 \approx 60 - 70$ nsec, the output signal will rise to about 95% of the maximum value. Hence, using the same assumptions as before, we obtain

$$S/N = [(2/3)(N_T/N)]^{1/2} = [(2/3)(500/10)]^{1/2} = 5.8 \qquad (7)$$

Hence we obtain a S/N that is $\sqrt{2/3} = 0.81$ of the optimum value. In practice, S/N will be somewhat smaller to account for the bandpass shape of the multiplexer filter.

This method is reasonably efficient and considerably less expensive than the optimal method. It will be very promising if the laser pulse length can be increased to 1 μsec.

The signal/noise ratios that we predict are rather dismaying in view of the complexity and expense of the necessary hardware. It can be justified only if the information that we obtain is unique or as a demonstration model to that extent. Furthermore, a plasma diagnostic method will be generally acceptable only if the physical parameters that characterize the plasma are easily retrievable. In this regard the optimal method offers possibilities not shared with the other two methods, that only estimate the power spectrum of the Thomson scattering. The reasons are that with the optimal method we measure detailed information about the random amplitude and phase of the scattered electric field. Part of this information is thrown out when the power spectra is calculated.[30] Furthermore, since the ion feature of the Thomson scattering is a rather smooth function of frequency it may be amenable to a description by means of an autoregressive time series[31] with a small number of parameters. These parameters may be estimated by well known methods in time series analysis,[32,33] and they will be related to the basic parameters that enter in the models used to describe the plasma. Therefore, we may be able to determine more information about the plasma than just the ion temperature, and we may also have a check for consistency of the model used. It is for these reasons that the time series analysis may justify its expense and become a powerful diagnostic tool.

Regardless of the signal processing technique employed, the spectra should be normalized in order to obtain an absolute determination of the spectral function. The simplest approximation is to normalize the spectra to the total laser energy during the pulse. For this purpose a small window at the Brewster angle is placed at the tip of the laser dump (Section 8). This normalization is very simple to perform as a change of scale in the display hardware. With the signal/noise ratio expected at the present time, this normalization of the power spectral function will not introduce undue error. However, corrections for the laser pulse spectral response, IF amplifier frequency response, etc., may be necessary if a more accurate plasma spectral function is required.

The signal/noise ratio estimates that we presented previously only relate the first and second moments of the χ^2 distribution; we did not discuss in any detail confidence bands, shape of the distribution, etc. Instead of presenting the details of statistical errors, we will show the results of a computer simulation that closely resembles the optimal configuration. Using a random number generator we simulate two independent realizations of band limited white noise sources; each noise source is a 1024 point time series with independent real and imaginary components. The time and frequency scale in Figs. 29 - 33 have been normalized to sample number. The 1024 point FFT (fast Fourier transform) of the first noise source, with an RMS power of one unit, is shown in Fig. 29. This figure shows very dramatically that the FFT of a noise signal is also noise. This noise simulates the contribution to the signal arising from plasma background and from the first mixer - IF amplifier.

The second noise source, with an RMS power of ten units, is passed through a chain of RC filters to simulate the Gaussian power spectral function (expected from SUMMA) shown in Fig. 30. The 1024 point FFT of this signal is shown in Fig. 31 which again manifest the noise character of the transform. We now average over 64 consecutive points in the FFT and the results are depicted in Fig. 32 and Fig. 33.

Figure 32 shows the result for the Gaussian signal only, while Fig. 33 shows the result for the superposition of the Gaussian spectrum noise plus the white noise. In each of these the expected RMS signal/noise ratio is

$$S/N = (64)^{1/2} = 8 \tag{8}$$

These results show, quite dramatically, the effect of signal statistics on the measured power spectrum.

SECTION 5

SMM LASER AND RECEIVER SPECIFICATIONS

In this section we will collect the specifications for the laser and the receiver that have been discussed previously and will complete them with further details.

A. LASER SPECIFICATIONS

One important requirement we will discuss now is the spectral purity of the laser output. This specification is closely related to the dump efficiency, so we will consider it first.

In Fig. 3 we sketch a realization of the Thomson scattering experiment. The laser output is focussed by the lens L_1 into the plasma. A minute fraction of this signal is scattered by the plasma and collected by the lens L_2 into the receiver. The remaining signal falls into the laser beam dump where it is almost completely absorbed. However, a small fraction of this signal is reflected back into the vacuum chamber where it is scrambled by many reflections in the walls. The walls of the vacuum chamber will then have a brightness proportional to the ratio of the laser beam dump area to the effective vacuum chamber area. Since the field of view of the receiver is entirely covered by the viewing dump, the stray signal collected by L_2 will be decreased by viewing dump absorption factor. In Section 8 there is a discussion of possible dump configurations, and it is estimated that a dump efficiency (ratio of reflected signal to incoming signal) of 10^{-4} is possible. If we assume an area ratio of 10^{-3}, the total dump efficiency is ($10^{-4} \times 10^{-3} \times 10^{-4}$)

$$D = 10^{-11}.$$

We can now estimate the spectral requirements of the SMM laser. As we show in Fig. 34 the power spectrum of the laser is divided in two parts: 1) the main laser line which is assumed to have a Gaussian line shape; 2) the superradiance which (lacking a better criter⁻ n) is assumed to have a rectangular line shape. These two components will contribute stray signals to the measured power spectra that must be kept below the -10 db power level of the Thomson scattered signal. This require-ment is imposed in order to make the Thomson scattering power spectral features to be above the statistical noise level (Section 4) of the measured spectra, and also to allow for a simple background subtraction.

The Gaussian line shape will totally obliterate the central feature of the Thomson spectral function and will also make impossible the detection of the spectral features of heavy impurities unless its spectral width is very narrow. If we accept a loss of approximately 10% of the total spectral width and no more than $\delta F = 250$ MHz, the -10 db total laser line width is calculated as follows.

The laser line spectral function is

$$I(F) = 1.71 (P_T/\delta f) \exp[-(2F/\delta f)^2 \ln 10],   \tag{1}$$

where P_T is the total laser power in the main line, δf the -10 db total linewidth, $F = f - f_o$, and f_o is the laser center frequency.

Then

$$S_o/10 \geq 1.71 (P_T/\delta f) \exp[-(\delta F/\delta f)^2 \ln 10] D   \tag{2}$$

For $P_T = 1$ MW, $\delta F = 250$ MHz, $D = 10^{-11}$ we find that

$S_o/10$ (W/Hz)	δf (MHz)
10^{-19}	100
10^{-18}	110
10^{-17}	120

Laser superradiance will contribute a background signal over a larger region of the Thomson spectral density, and its effect is calculated in the same way as above

$$S_o/10 \geq D P_{sr}/BW_{sr} , \tag{3}$$

where P_{sr} is the total amount of power in the superradiance background, and BW_{sr} is its bandwidth.

The superradiance bandwidth has not yet been measured for the CH_3F or the D_2O lasers. It is estimated that it may be anywhere between one to three GHz. If we assume that $BW_{sr} = 2.5$ GHz, we find

$S_o/10$ (W/Hz)	P_{sr}(W)
10^{-19}	25
10^{-18} (TFTR)	250
10^{-17} (SUMMA)	2500

Therefore, the amount of superradiance allowed is very much restricted.

Finally the laser and dump specifications are the following:

TOTAL POWER	$P_T \geq 1$ MW
PULSE WIDTH	$T > 200$ nsec
GAUSSIAN LINEWIDTH (-10 db)	$\delta f \leq 110$ MHz
SUPERRADIANCE:	
SUMMA	$P_{sr} \leq 2500$ W/2.5 GHz
TFTR	$P_{sr} \leq 250$ W/2.5 GHz
TOTAL DUMP EFFICIENCY	$D \leq 10^{-11}$

B. RECEIVER SPECIFICATIONS

The receiver consists of the antenna, mixer, local oscillator, and the low noise IF amplifier. Considerable development work is going on at the MIT - Lincoln Laboratory, MA and at the Jet Propulsion Laboratory, CA, and in this report we will not discuss the details of this work. We will summarize the receiver specifications that have been established in earlier sections and will make an educated guess of the mixer conversion loss in order to estimate the IF amplifier again. The antenna parameters that have been used in Section 6 to study the collection optics, correspond to the 50 mm aperture, lens corrected cylindrical horn presently being used at the Lincoln Laboratory as the standard rig for Schottky diode testing. This structure has not been optimized and may change in the future.

A summary of the receiver specifications follows:

HETERODYNE RECEIVER	$f_{IF} \approx 5 - 15$ GHz
COLLECTION OPTICS EFFICIENCY	$\eta \approx 10\%$
SOLID ANGLE OF ACCEPTANCE TIMES LENGTH OF PLASMA FOCUSSED	$\ell \Delta \Omega \approx 10^{-4}$ m. sr
INPUT NOISE	
SUMMA	$kT_{eff} \leq 10^{-18}$ W/Hz
TFTR	$kT_{eff} \leq 10^{-19}$ W/Hz
BANDWIDTH	
SUMMA	$BW \approx 2$ GHz
TFTR	$BW \approx 4$ GHz

In Section 6 we calculated that the value of $\ell \Delta \Omega \approx 0.5 \times 10^{-4}$ m. sr, but the collection optics efficiency probably can be increased to $\eta \approx 20\%$, hence the product is approximately constant.

The conversion loss L of the mixer is an important quantity. If L is large the IF amplifier noise and the effective mixer temperature T_M will contribute significantly to the single sideband input noise, while the antenna temperature will not be important. For the time being we do not expect mixers with a conversion loss better than ~ 13 db (20), hence a single sideband input noise of the order (Fig. 23)

$$T_{eff} \approx (L - 2) T_M + L T_{IF} = 1.14 \times 10^4 \, K \qquad (4)$$

$$\text{or } kT_{eff} = 1.6 \times 10^{-19} \, W/Hz,$$

where we have assumed that $T_M \approx 500$ K and $T_{IF} \approx 120$ K. The latest results from MIT[34] and JPL[35] show measured values $kT_{eff} \approx 2 - 4 \times 10^{-18}$ W/Hz. This will satisfy the requirements for SUMMA, but for TFTR we require a factor of ten improvement.

We can now determine the power gain of the IF amplifier. The total power scattered between the -10 db points of the spectra has been determined by numerical integration of the spectral density and it is equal to

$$P_s \approx 3 \times 10^{-8} \, W \text{ for TFTR}$$
$$\text{and } P_s \approx 7 \times 10^{-8} \, W \text{ for SUMMA,}$$

where we have assumed that $P_T = 1$ MW, $l\Delta\Omega = 10^{-4}$ m. sr, and $N_e = 10^{20}$ m^{-3}.

For convenient signal processing and in order to minimize the effects of electromagnetic interference, the output of the IF amplifier must have a power level P_{IF} between 0.1 and 1 mW. (We assume the standard 50 ohm impedance lines.) Then

$$P_{IF} = P_s \, \eta \, G_{IF}/L \qquad (5)$$

where η is the efficiency of the collection optics, and G_{IF} is the power gain of the IF amplifier. If we assume that $L \approx 100$ for SUMMA or $L \approx 20$ for TFTR, $\eta \approx 0.1$, and $P_{IF} \approx 10^{-3}$ W, then the power gain of the IF amplifier is $G_{IF} \approx 70$ db.

43

Finally, the specifications for the IF amplifier are:

PARAMETRIC AMPLIFIER
    INPUT NOISE TEMPERATURE $T_{IF} \simeq 120$ K

POWER GAIN $G_{IF} \simeq 70$ db

CENTER FREQUENCY $f_{IF} \simeq 5 - 15$ GHz

(The center frequency will be determined once the SMM laser and the local oscillator are chosen.)

BANDPASS

SUMMA $\Delta f \simeq 2$ GHz

TFTR $\Delta f \simeq 4$ GHz

SECTION 6

COLLECTION OPTICS AND ANTENNA FOR THE THOMSON SCATTERED RADIATION

The collection system must satisfy the following requirements:

1) It must be efficient; i.e., the ratio $P_d/P_s \leq 1$ of the scattered power reaching the detector and the total scattered power allowed in the aperture of the optical system must be as large as possible.

2) The product, $\ell \, \Delta\Omega$, of the plasma scattering length along the incoming laser beam and the solid angle of scattering should be large in order to maximize the scattered power.

3) The angular spread, $\Delta\theta$, of the scattered radiation should be small in order to have a good spectral resolution.

4) The scattering length ℓ should be within the depth of focus of the collection optics.

5) The mechanical setup of the collection system must satisfy stringent alignment requirements.

6) EMI (electromagnetic interference) should not hinder the operation of the detector and/or introduce spurious signals.

7) As far as it is possible the collection system should be insensitive to spurious scattered signals and plasma noise.

As we will see shortly, some of the above conditions are incompatible with each other and compromises will have to be accepted. The particular machine for which Thomson scattering diagnostic will be used, the laser power available, the detector noise and other relevant factors will have to be considered before reaching an acceptable compromise.

In Figure 35 we sketch a suitable arrangement for the collection optics. We will use it to deduce the necessary equations and obtain estimates of the important parameters. The lens L_1 collimates the scattered radiation centered at its focus F_1. Because of the finite extent l of the plasma scattering region, we must insure:

a) That the depth of focus to the 3 db points of L_1[36] is sufficient to accommodate l, i.e.,

$$l \cos \theta < 6.3 \lambda \, f_1^2/D^2 \qquad (1)$$

where λ is the wavelength of the radiation and the F-number of the lens L_1 is equal to f_1/D.

b) For maximum efficiency of the receiving antenna, the angle α of the collimated beam is made equal to the 3 db full beamwidth angle of the main radiation lobe of the antenna. For the quasioptical antennas required at the frequencies of interest here, the angle α (in degrees) is given by[37]

$$\alpha = K\lambda/D \qquad (2)$$

where K is weakly dependent on the antenna type, on whether the E- or H-plane of polarization is used and on the illumination function of the aperture.

These two requirements plus the scattering angle θ are sufficient to write all the necessary geometrical relationships between the parameters of interest. Here we have assumed that only paraxial rays are important to describe the lens L_1. We find that:

Plasma scattering length

$$l = \frac{\pi}{180} \, \frac{K\lambda}{\sin \theta} \, \frac{f_1}{D} \qquad (3)$$

Solid angle of collection

$$\Delta\Omega(sr) \approx \frac{\pi}{4}\left(\frac{D}{f_1}\right)^2 \tag{4}$$

Angular spread of scattered radiation

$$\Delta\theta \text{ (degrees)} \approx \frac{180}{\pi}\frac{D}{f_1} \tag{5}$$

and

$$\ell\Delta\Omega \approx \frac{\pi^2 K}{720}\frac{\lambda}{\sin\theta}\frac{D}{f_1} \tag{6}$$

The F-number of L_1 is determined by $\Delta\theta$ which is determined by the spectral resol̲ ̲ ̲ ̲l, Δf, that is required. The plasma electron and ion temperatures (T_e and T_i) and the scattering angle θ will play a major role in assigning a value to $\Delta\theta$. On the other hand we also want to maximize the scattered power which is proportional to $\ell\Delta\Omega$ and, therefore, proportional to $\Delta\theta$. Calculations performed with typical plasma parameters suitable for the VERSATOR and the SUMMA machines show that for $\theta = 30^\circ \pm 2.5^\circ$ and $\theta = 20^\circ \pm 1.5^\circ$ we may expect a frequency resolution for the important features of the ion spectrum of $\pm 5\%$. Using these values for θ and $\Delta\theta$ and Eq. (5) the F-number of the collection optics can now be calculated. It is listed in Table VI for the two possible scattering angles. To calculate the focal length, f_1, and aperture, D, of the collection lens some details of the plasma machine must be known. For example, in SUMMA the collection optics must be a minimum of 1 m from the plasma. Assuming a focal length between 1.0 and 1.5 m the aperture of the collection optics has been calculated and listed in Table VI. These values also represent the lower limit on the diameter of an access port a distance f_1 from the plasma.

The plasma scattering length, ℓ, and $\ell\Delta\Omega$ have also been calculated and tabulated in Table VI for $\lambda = 385\,\mu m$ and $K = 63$.[37] The plasma scattering length

decreases with increasing scattering angle but because $\Delta\theta_{max}$ and as a result $\Delta\Omega$ increase, $\ell \Delta\Omega$ is nearly the same for both scattering angles. The depth of focus of L_1 is the final entry in Table VI and a comparison of these values with ℓ shows that the inequality Eq. (1) is well satisfied.

An axicon[38, 39] can be used to increase $\Delta\Omega$ without affecting $\Delta\theta$ or the frequency resolution. The scattering volume of the plasma for a given scattering angle radiates symmetrically around the laser beam axis. Using an axicon can increase the arc centered on the laser beam axis over which scattered radiation can be collected. The solid angle of collection for an axicon is given by

$$\Delta\Omega(sr) = (\pi/180)^2 \, \Delta\phi \, \Delta\theta \, \sin\theta \qquad (7)$$

where $\Delta\phi$ is the number of degrees in the axicon arc centered on the laser beam axis and $\Delta\theta$ (degrees) and θ are the same as defined earlier. Eq. (7) reduces to Eq. (4), the nonaxicon case, when

$$(\pi/180) \, \Delta\phi \, \sin\theta = (\pi/180) \, \Delta\theta = (D/f_1)$$

and a correction is made for a circular area (multiply by $\pi/4$).

The use of an axicon is illustrated in Figure 36 where it is labelled with an A. The axicon is a segment of a conical surface the inside surface of which is a reflector. It has the property of projecting the scattered radiation from a point on its axis on to a line along its axis. The geometrical relationships between the parameters of interest are given by

$$z = x \left(\cos\theta + \frac{\sin\theta}{\tan(\theta - \beta)} \right) \qquad (8)$$

$$\Delta z = 2x \left(1 + \frac{\sin\theta}{\sin(\theta - \beta)} \right) \tan\frac{\Delta\theta}{2} \qquad (9)$$

$$p = \frac{\pi}{180} \frac{x \, \Delta\theta}{\sin\frac{\beta}{2}} \qquad (10)$$

$$C = (2r + p \sin\tfrac{\beta}{2}) \sin\tfrac{\Delta\phi}{2} \qquad (11)$$

where

z is the distance from the plasma scattering volume to the center of the projected line

Δz is the length of the projected line

x is the distance from the plasma scattering volume to the center of the axicon

β is the angle at the apex of the cone of which the axicon is a segment

p is the slant length of the axicon

C is the length of the longest chord in the axicon arc

r is the radius of arc of the center of the axicon and is equal to $x \sin\theta$.

The rest of the parameters are the same as defined previously. The details of the collection optics following the axicon will depend to a large extent on the value of the angle β chosen. When $\beta = \theta$ the scattered radiation is projected onto a line at infinity and the collection optics following the axicon can be placed adjacent to it so that the focal length of lens L_1 is given by

$$f_1 = x + \tfrac{1}{2} p \cos\tfrac{\beta}{2} \qquad (12)$$

The parameters of interest for this case are tabulated in Table VII for two possible scattering angles of 20° and 30°. We have assumed $\Delta\phi = 30^{\circ}$, $\lambda = 385 \, \mu m$, and $K = 63$. The distance of the axicon from the plasma will depend to a large extent on the plasma machine and in the case of SUMMA would have to be at least 1.2 m. The frequency resolution of the collected radiation is determined by the slant length, p, of the axicon. The F-number of the collection optics depends on the requirement that all the radiation reflected by the axicon must be collected. Large apertures with diameter C are required and as a result the F-number is much smaller than

when no axicon is used. The motivation for using an axicon is evident by comparing the values for $\Delta\Omega$ in Table VII with those of Table VI. $\Delta\Omega$ is about a factor of four larger with a 30° axicon, but because the F-number is much smaller the plasma scattering length as calculated by Eq. (3) is also smaller and therefore there is only a modest improvement in $\ell\,\Delta\Omega$. This small improvement in $\ell\,\Delta\Omega$ could be offset by increased absorption in a larger lens L_1.

It is possible to increase the F-number of the lens following the axicon by moving it to the axicon axis and choosing $\beta < \theta$ so that Δz is within the depth of focus of the larger F-number lens. The depth of focus of such a lens is related to angle θ by

$$d = 6.3\,\lambda\left(\frac{1}{2\tan(\theta - \beta)}\right)^2 \qquad (13)$$

where the quantity in parentheses is equal to the F-number. Since, for small values of $(\theta - \beta)$, d increases as the inverse square of $(\theta - \beta)$ and Δz of Eq. (9) increases only as the inverse of $(\theta - \beta)$, then we require a lens with a large F-number to image Δz. In fact it seems possible to make the F-number large enough so that ℓ equals the depth of focus of the laser beam or the plasma diameter whichever is smaller. For SUMMA the plasma diameter is small, about equal to 10 cm. Therefore it is possible to increase $\ell\,\Delta\Omega$ at the expense of spacial resolution by a factor of 18 and 40 for 20° and 30° scattering respectively using an axicon of $\Delta\phi = 30°$. The problem with achieving this potential improvement is that $(\theta - \beta)$ must be less than 2° and using Eq. (8) it can be shown that L_1 has to be placed further than 13 and 18 m from the plasma for 20° and 30° scattering respectively. Such distances for the collection optics are impractical.

We therefore conclude that the use of a single axicon does not look feasible at this time. Axicons do have a great potential for increasing $\ell\,\Delta\Omega$ and should not be ruled out completely. Future design studies using two axicons together may overcome the practical limitations of one axicon.

It appears at this time that the collections optics setup of Fig. 35 is the most promising. Consideration should now be given to the kind of mechanical stability required. The combined mechanical stability and the alignment accuracy is determined by the 3 db full beamwidth, α, of the main radiation lobe of the antenna and by the focal length, f_1, of lens L_1. The value of f_1 should be made as small as possible to keep the alignment requirements as loose as possible. For example, in SUMMA, f_1 will have to be equal to at least 1.0 m. This also determines the aperture D, of the lens since the F-number is fixed by the required frequency resolution. Using the value of D in Table VI and Eq. (2), α for the antenna main radiation lobe can be calculated to be 0.47° and 0.28° for 20° and 30° scattering respectively. The fraction of angle α which represents a good and practically realizable alignment and mechanical stability requirement will depend on the details of the antenna and plasma machine under consideration. We believe that a minimal requirement is $\Delta\alpha \leq \pm \frac{\alpha}{10} = \pm 0.047^\circ$ or $\pm 0.028^\circ$ for 20° and 30° scattering angles respectively.

The choice of antenna will depend on a variety of considerations, some of them rather difficult to quantify. For antenna apertures $D \geq 0.05$ m and $D/\lambda \gg 1$, a lens corrected conical horn is a rugged and reasonably easy to align structure. However, the type of detector/mixer used (for the submillimeter Thomson scattering radiation considered here) will have an important role in selecting a suitable antenna. For a Schottky barrier diode detector (Section 5), with a characteristic dimension $d < \lambda$ and a typical RF impedance of the junction $|Z_{RF}| \simeq 50\,\Omega$, there is not, at the present time, an optimal configuration for diode assembly. As an expedient and temporary approach for receiver measurements we have selected a lens corrected conical horn with an aperture $D = 0.05$ m, feeding an oversize waveguide. An estimate of the horn aperture efficiency (G. Gill, TRG, Woburn, MA, private communication) is $\eta_1 \simeq 0.50$. This means that only one half of the incoming energy will reach the waveguide.

The fraction ($1 - \eta_2$) of energy loss due to transmission and multimoding in the oversize waveguide cannot be estimated at the present time. These losses will be strongly dependent on the diode mount, machining accuracy, alignment, surface roughness and local oscillator feed arrangement. In an optimized system we would like to avoid multimoding losses and minimize the waveguide transmission losses. However, with the presently proposed configurations, we are not optimistic that an efficiency larger than $\eta_2 \simeq 0.25$ can be achieved.

We must also consider the reflection and transmission losses of the scattered radiation by the exit port window and lens L_1. These components will most likely be made of a plastic such as polyethylene or TPX which have an index of refraction of 1.46 and absorption coefficients of 0.2 and 0.3 cm^{-1} respectively, measured at a wavelength of 337 μm.[40] The reflection loss per surface can be calculated to be 3.5% and absorption losses per cm of thickness as 18% and 26% for polyethylene and TPX respectively. If a thin polyethylene window about 1 mm thick is used and lens L_1 is made of polyethylene or TPX then a transmission efficiency of $\eta_3 = 0.80$ is possible. Therefore, the total efficiency of the collection optics and antenna system is $\eta_T = \eta_1 \eta_2 \eta_3 \simeq 0.10$. This means that only one tenth of the scattered power collected at the exit port will reach the Schottky diode mixer.

The collection optics and antenna will also determine the volume of plasma, V_{eff}, that will contribute to the plasma noise (Section 3) seen by the detector. If the plasma is assumed to be optically transparent (i.e., the plasma dispersion and refractive index is neglected) the effective noise volume can be shown to be equal to the intersection of the plasma with two truncated cones joined at the smallest plane right sections, centered at the focal point F (Fig. 37), and with the cones axis along the lens L_1 axis. The smallest diameter of the cones where they are connected is equal to the focal spot size of lens L_1. The formula for this volume for the approximations $\frac{D}{f_1} << 1$ and $h >> s$ is

$$V_{eff} = \frac{1}{6} \pi h \left\{ s^2 + \left(h \frac{D}{f_1} + s \right)^2 + s \left(h \frac{D}{f_1} + s \right) \right\} \qquad (14)$$

where h is the radius of the plasma and $s = 2.44 \lambda f_1 / D$ is the spot size of the focal point of L_1. Assuming $f_1 = 1.0$ m and the same collection optics parameters as before and a plasma radius of 5 cm $V_{eff} = 29$ cm^3 and 13 cm^3 for 20° and 30° scattering respectively.

SECTION 7

SUBMILLIMETER LASER BEAM FOCUSING

Highly transmitting lens and window material for submillimeter radiation is difficult to find, especially for 20 cm diameter optics. High density polyethylene, teflon, and TPX which are most commonly used have absorption and reflection losses of 20% to 30% for thicknesses of 1 cm.[41-43] These materials, except for TPX, are also opaque to visible light which would make optical components difficult to align. For these reasons the number of windows in the submillimeter path should be kept to a minimum and wherever lenses are required mirrors should be used instead. Optical quality mirrors are readily available and are essentially lossless to submillimeter radiation.

It is required that the laser beam be focussed to the smallest size possible so that there is adequate spatial resolution and all the available laser power is concentrated for scattering within the field of view of the collection optics. Two basic effects can limit the size to which a laser beam can be focussed. They are aberrations and diffraction. Both these effects are wavelength dependent with aberrations becoming worst for shorter wavelengths and diffraction effects becoming worst for longer wavelengths. It has been shown that primary spherical aberrations can be the dominant effect in determining the intensity distribution of a focussed laser beam when they are equal to or larger than the wavelength of the laser radiation.[44] The spherical aberration for a plano convex lens is given by[45]

$$\psi = -\frac{\rho^4}{32\,f^3}\left[\frac{n^2}{(n-1)^2} - \frac{n}{n+2} + \frac{(2n^2-n-4)^2}{n(n+2)(n-1)^2}\right] \tag{1}$$

54

where

  ρ is the radius of the laser beam

  f is the focal length of the lens

  n is the index of refraction of the lens.

For submillimeter wavelengths it can be shown that $\psi < \lambda$ for all practical values of ρ, f, and n. Using focussing mirrors instead of lenses the spherical aberrations can be reduced.

One type of primary aberration called coma can be a problem if spherical mirrors are used to focus off axis. Coma can be eliminated by using mirrors made of parabolic segments. We therefore feel that aberrations will not be the limiting factor in focussing the submillimeter laser b am. The dimension of the laser focal spot will be determined primarily by diffraction effects.

If a focussing mirror or lens is uniformly illuminated a diffraction pattern will be formed at the focus. The pattern will consist of a bright central spot surrounded by concentric rings of diminishing intensity. The central spot is known as the Airy disc and its diameter is given by[46]

$$s = 2.44 \lambda \frac{f}{D} \tag{2}$$

where

  λ is the wavelength of the radiation

  f is the focal length of the lens or mirror

  D is the diameter of the lens or mirror.

84% of the laser power will be contained within the diameter defined by s. The Airy disc plus the first two diffraction rings will contain 94% of the total power within a diameter given by

$$s' = 6.47 \lambda \frac{f}{D} \tag{3}$$

In reality, the mirror or lens will not be uniformly illuminated. The output of a laser operating in its fundamental transverse mode (TEM_{oo}) has a Gaussian intensity distribution

$$I(r) = \frac{2P_o}{\pi a^2} e^{-2r^2/a^2} \tag{4}$$

where

P_o   is the total laser power

I(r)   is the intensity at a distance r from the beam axis

a   is the radius of the beam where the intensity falls to $1/e^2$ of the maximum intensity.

The laser beam diameter is generally defined as 2a and contains 86.5% of the total beam power. The image to which a Gaussian beam can be focussed depends on the size of the lens or mirror aperture. If the aperture is less than 2a, then the image will be similar to an Airy pattern. As the aperture is increased, the diffraction effect produced at the aperture boundary decreases and more of the laser power is focussed into the central spot. When the aperture diameter is larger than 2.8a the Gaussian intensity distribution is preserved at the focal point and its diameter to the e^{-2} intensity points is[47]

$$s_G = 1.27 \lambda \frac{f}{D} \tag{5}$$

Since the submillimeter laser beam will have a radius of about 10 cm, it may be practical to make the focussing mirror large enough to achieve a spot size given by Eq. (5). That would require a mirror with a diameter of at least 28 cm. We plan to use a mirror with an aperture of 20 cm and therefore Eqs. (2) and (3) are more applicable to determine the focal spot size.

Figure 38 shows a possible arrangement for focussing a submillimeter laser beam into a plasma for Thomson scattering. The focussing mirror is an off axis segment of a parabola with a focal length f. The parabolic segment was chosen to be 34° off axis so that if a polyethylene window is used between the mirror and laser the laser beam would be incident at Brewster's angle, minimizing reflection losses.

Baffles are used to minimize the amount of stray submillimeter radiation in the plasma. These baffles are inverted cones placed inside the entrance tube to the plasma to trap stray submillimeter radiation that is not following the focussed laser beam path. They are made of a reflector covered on both sides with a submillimeter absorbing material. One possibility for making these baffles is to use a metallic cone sandwiched between two plexiglass cones (Section 8). Stray radiation coming from the plasma would also be trapped by this arrangement.

A number of these baffles with varying aperture size to conform to the focussed laser beam path should be used between the focussing mirror and plasma. This requirement is in conflict with the need to place the focussing mirror as close as possible to the plasma to minimize the focal spot size, Eq. (2). A compromise has to be made. In SUMMA, for example, no optics or conical baffles can be placed less than 1 m from the plasma because of the sputtering problem. The focussing mirror should be placed an additional 2 m away to allow room for a few baffles and a shutter to protect the optics. Therefore, a focussing mirror with a focal length of about 3 m will be required. The corresponding diffraction limited spot size will be 1.4 cm for 84% of the laser power and 3.7 cm for 94% of the power at $\lambda = 385$ μm. These dimensions are well with the depth of focus of the collection optics (Section 6) so that the entire 1 MW submillimeter laser beam can be usefully focussed. The fact that the focussing mirror has a diameter of 20 cm and does not reflect the entire Gauss'an laser beam should not be considered a loss because when the 1 MW output of the laser is measured it is done with a finite aperture mirror also.

SECTION 8

BEAM AND VIEWING DUMPS

After the laser beam passes through the plasma it must be collected and absorbed as efficiently as possible with a beam dump to minimize the background radiation. A viewing dump opposite the collection optics will also be required to further reduce the background radiation reaching the detector. Many different beam dump designs have been successfully used with ruby laser Thomson scattering.[48] These usually take the form of blackened light cones or highly absorbing blue glass at Brewster's angle.[49, 50] The latter require a well collimated and polarized laser beam. Submillimeter laser beam dumps can be of similar design, but the materials they are made of will have to be different. For example, black coatings are not absorbing at submillimeter wavelengths.

One promising submillimeter beam dump material that we have tested is plexiglass (acrylic, polymethyl methacrylate), a common plastic. It is readily available, easy to mold into any shape, and can be used in vacuum. At 385 μm we have measured a 3 mm thick piece to transmit only 4% of the submillimeter laser beam and to reflect about 7% at near normal incidence. These experimental measurements can be interpreted if plexiglass has an index of refraction of 1.7 and an absorption coefficient of about 10 neper cm^{-1} at a frequency of 780 GHz. The nearest published values taken at 3 GHz give an index of refraction of 1.61 and absorption coefficient of 0.75 neper cm^{-1}.[51] The high absorption coefficient measured for submillimeter waves means that if a plexiglass window at Brewster's angle is used as a beam dump and the submillimeter laser beam is well collimated

and linearly polarized then a window thickness of only 1 cm would give a beam dump efficiency of 2×10^{-9}.

In practice the submillimeter laser beam will not be well collimated. The laser beam will start out 15 to 20 cm in diameter and will be focussed to a diffraction limited spot in the plasma. As it leaves the plasma it will be diverging with an angle dependent on the focal length of the focussing mirror. It is not expected that the plasma itself will add significantly to the laser beam divergence (for small dimension plasmas). How well a Brewster's angle window will act as a beam dump in this case can be analyzed by using Fresnel's equation for reflectance from a surface when the polarization of the light is parallel to the plane of incidence:

$$R = \left(\frac{\tan(\theta_i - \theta_t)}{\tan(\theta_i + \theta_t)} \right)^2 \tag{1}$$

where θ_i is the angle of incidence relative to the surface normal and θ_t is the angle of the transmitted ray given by Snell's law, $\sin\theta_i = n \sin\theta_t$ where n is the index of refraction of the window material. Brewster's angle is defined as the angle of incidence for which $\theta_i + \theta_t$ equals 90°. In that case the denominator of Eq.(1) goes to infinity and the reflectance is zero. Plexiglass has a Brewster's angle of 59.5° for an index of refraction equal to 1.7.

If we assume that the submillimeter laser beam is 20 cm in diameter and is focussed with a 3 m focal length mirror, then the laser beam will be diverging with a half angle of about 2° when it is incident on the plexiglass beam dump. Using Eq. (1) the reflectance of light rays $\pm 2^{\circ}$ from Brewster's angle can be calculated. This reflectance is about equal to 7.0×10^{-4} and drops to 4.0×10^{-4} for light rays $\pm 1.5^{\circ}$ from Brewster's angle. It can be shown for this case that 40% of the laser beam power has a half angle of divergence between 1.5° and 2° so that a maximum beam dump efficiency of roughly 3.0×10^{-4} is expected. This number

will increase if the laser beam is not completely polarized. Such a value is not good enough for the submillimeter Thomson scattering experiment.

Improved beam dump efficiency independent of laser beam polarization can be achieved by making a plexiglass light cone. The theory is to trap the laser beam into making as many reflections as possible to dissipate its intensity. The trans-mitted fraction at each reflection can be ignored if the cone is everywhere made at least 1 cm thick and is enclosed in a metallic cylinder. The number of reflections that a light ray will make in a cone before it is reflected back out is given by

$$m = \text{Int}\left[2\left(\frac{90 - \delta}{\beta}\right)\right] \tag{2}$$

where the right side is truncated to an integer value, β is the angle at the apex of the cone in degrees, and δ is the angle in degrees that an incoming light ray makes relative to the cone axis. Equation (2) is true only if geometrical ray tracing is valid, i.e., only when the cone is large enough and the light ray is far enough off axis so that none of the reflections take place in the region near the apex of the cone where the diameter of the cone is comparable to a wavelength.

A cone with a length 10 times its diameter will have $\beta \simeq 5.8^{\circ}$. If we use such a plexiglass cone centered on the laser beam axis as a beam dump (see Fig. 39), for a 20 cm diameter laser beam that was focussed with a 3 m focal length mirror then the outside light rays collected by the beam dump will have $\delta = 2^{\circ}$ and the total number of reflections that ray will make is 30. Of these 30 reflections 4 will be close to normal incidence for which the reflection coefficient is about 7% and another 11 reflections will be at angles of 45° or less for which the reflection coefficient is 15% or less. Just these 15 reflections alone will attenuate that light ray by a factor of 2×10^{-14}. The remaining 15 reflections at angles greater than 45° will attenuate the light ray further but their contribution would depend greatly on the polarization.

We will ignore these reflections and use the value 2×10^{-14} as an upper limit for the attenuation of the outside rays of the laser beam. In fact, it can be shown that all light rays of the laser beam will be attenuated by at least this factor if they do not interact with the small dimension of the cone near its apex. Therefore, if the plexiglass cone is made large enough a beam dump efficiency of better than 2×10^{-14} is possible.

In practice because of the large size of the submillimeter laser beam it may not be practical to make such a large cone. Possible dimensions for a beam dump cone are shown in Fig. 39. We are assuming that the beam dump is placed 1 m from the focal spot of a 20 cm diameter laser beam that was focussed by a 3 m focal length mirror. It can be estimated that the diameter of the laser beam at the aperture of the cone will be 8 cm. A cone with an opening of 10 cm in diameter should be adequate to insure that the entire laser beam is collected. A small Brewster's angle window is cut in the apex of the cone to monitor the laser beam (Fig. 40). The attenuation efficiency of such a cone can be analyzed by dividing the cross section of the laser beam at the cone aperture into three areas (Fig. 41): the outside rays of the laser beam which suffer 30 reflections and are attenuated by a factor of 2×10^{-14}, the light rays that pass close to the cone axis and receive less than 30 reflections but are not close enough to the cone axis to pass through the Brewster's angle window, and the area near the cone axis which contains the light rays that do go through the Brewster's angle window without reflection. The efficiency for attenuating a light ray in each of these regions must be weighted by the fraction of the laser beam energy passing through that region. The overall attenuation of the cone is then the sum of the attenuation factors for each region of the cone.

If we assume the laser beam has a parabolic profile at the cone aperture then 85% of the beam energy will be located in the outside region of the beam cross section bounded by the 1 cm and 4 cm radius circles (see Fig. 41). The attenuation

factor for this part of the laser beam is 1.7×10^{-14}. In the annulus bounded by the 0.1 cm radius Brewster's angle window and a 1 cm radius circle the light rays do not receive 30 reflections. The number of reflections the light ray will suffer will vary from about 30 at the 1 cm radius circle down to at least one at the 0.1 radius circle. The geometrical average of 10^{-1} and 2×10^{-14} multiplied by 0.15 which is the fraction of the total laser beam energy in this region, gives an attenuation factor for this part of the laser beam of 7×10^{-9}. The 2 mm diameter Brewster's angle window at the cone apex will only intersect about 6×10^{-4} of the laser beam and if the window is 0.5 cm thick a maximum of only 3×10^{-8} can be reflected from this region of the beam dump while passing a peak intensity of about 1 W for a monitor detector. The overall beam dump attenuation efficiency is the sum of 1.7×10^{-14}, 7×10^{-9}, and 3×10^{-8} which is about 4×10^{-8}.

This particular design for a beam dump will depend on the laser beam polarization. The contribution from the Brewster's angle window will increase for a nonpolarized beam. If 1% of the laser beam is of the wrong polarization then the beam dump attenuation factor can increase to 2×10^{-6} if we assume no trapping of the light ray of the wrong polarization incident on the Brewster's angle window. Actually, there will be some multiple reflections for this ray so that a beam dump efficiency of better than 10^{-6} is possible for a laser beam 99% linearly polarized. If the submillimeter laser beam is not this well polarized at the output of the laser amplifier a wire polarizer can be used to achieve at least 99% polarization before the beam is focussed into the plasma.

The viewing dump will be a cone similar to the beam dump except there will be no window at its apex. Therefore the efficiency of the viewing dump will be at least 10^{-8} independent of polarization. A beam dump efficiency of 10^{-6} combined with a viewing dump efficiency of 10^{-8} is more than adequate for submillimeter Thomson scattering plasma diagnostics.

SECTION 9

SUBMILLIMETER LASERS

A. INTRODUCTION

The minimum requirements of a submillimeter laser for Thomson scattering plasma diagnostics are that its power level be 1 MW in pulses lasting 200 ns with a full linewidth at one tenth maximum of 100 MHz. No submillimeter laser has yet been built which meets these requirements, but the level of progress achieved with optically pumped submillimeter lasers shows that such a laser will be available soon. Optically pumped submillimeter laser emissions are produced by molecular gases which are pumped by an infrared laser, typically a CO_2 laser, from a ground vibrational level to an upper vibrational level. Submillimeter laser action then takes place between two rotational levels of the upper vibrational state. These lasers were first invented in 1970[52] and at that time achieved peak power levels of 0.1 Watt. Development of these lasers has progressed at a remarkable pace and at the present time peak power levels of over 10^5 watts with linewidths and pulse lengths approaching those required for Thomson scattering plasma diagnostics have been demonstrated.

Interest in developing a high power submillimeter laser for plasma diagnostics at the Francis Bitter National Magnet Laboratory was first generated in 1974 by Jassby et al.[53] It was realized then that the conversion efficiency of CO_2 laser pump energy to submillimeter laser energy in CH_3F at 496 μm was high enough (0.1%) to be scaled to 1 MW power levels with current CO_2 lasers. In this section we will review the work presently being done at the National Magnet Laboratory to develop a laser for submillimeter Thomson scattering plasma diagnostics. First, in Part B of this

63

section we will briefly review the theory of submillimeter lasers and explain why we currently feel that D_2O is more promising than CH_3F for the submillimeter laser medium. In Part C we will describe the various laser system designs that have been built and tested here. It will be shown that eliminating superradiance is a major problem and how it can be overcome. Finally, in Part D a possible design for the 1 MW laser will be described.

B. THEORY

Figure 42 sketches the energy level diagram of a molecule used as an optically pumped submillimeter laser source. The ground and excited vibrational levels are subdivided into a number of rotational levels. The molecule is pumped from its ground vibrational level to its excited level by an intense optical pump. This requires a laser which oscillates on a wavelength that closely matches the pump transition. Submillimeter laser action then takes place between two rotational levels of the upper vibrational state. This transition is labeled FIR for far infrared in Figure 42.

A reason why high power submillimeter lasers operate as pulsed lasers is because the vibrational relaxation time of the excited vibrational level is generally slow and, under hard pumping conditions, after half the molecules are pumped to the upper vibrational level no more pumping will take place because the ground state will not repopulate fast enough by relaxing molecules. A fast rotational relaxation time will also hinder submillimeter laser action because molecules in the excited vibrational level redistribute the rotational energy among all the rotational levels and therefore reduce the population inversion for the submillimeter laser transition. A fast rotational relaxation time together with a slow vibrational relaxation time is referred to as the "bottleneck" effect and can represent a fundamental limitation on the amount of submillimeter energy one can expect from a given volume of a submillimeter laser

at a given pressure.[54, 55] A rough upper limit to the SMM energy available per pulse can be estimated as follows: under bottleneck conditions only about one half of the molecules can be pumped to the upper SMM laser level, and only half of these molecules can lase if the stimulated emission rate is faster than the rotational relaxation rate. Under these conditions for D_2O lasing at 385 μm we can expect an upper limit of 4.2 joules m^{-3} Torr^{-1} per pulse. At the present time only 4% of this energy is realized in practice.

A possible experimental setup for producing submillimeter laser radiation is shown in Figure 43. CO_2 lasers which oscillate on a number of transitions in the wavelength range from 9 to 11 μm are the most common optical pumps used. This is not just because many of the transitions of the CO_2 laser coincide in frequency with the vibrational pump transitions of many molecules, but also because CO_2 lasers are the best developed and most powerful infrared lasers available. In Figure 43 a TEA (transverse electric discharge at atmospheric pressure) CO_2 laser is shown because it is one of the more common commercially available pulsed CO_2 lasers. Note that the major component of the CO_2 laser is a grating reflector which is used to tune the laser to oscillate at one wavelength corresponding to the submillimeter laser pump transition.

The gain of submillimeter lasers is generally quite high and therefore a laser cavity is not required to produce submillimeter laser emissions. All that is needed is a long tube with a window on one end transparent to the infrared radiation, usually NaCl, and a window at the other end transparent to the submillimeter radiation, usually teflon or polyethylene. Laser emissions occur because some spontaneous emission is amplified by the high gain of the medium in one pass through the tube. This type of laser action is often called superradiance and presents a major problem in developing a submillimeter wave laser for Thomson scattering because of the inherent broad linewidth of superradiance.

A total of twenty-six gases have been discovered to produce submillimeter laser action when pumped with a CO_2 laser.[56] In Table VIII three of these gases that were studied at the National Magnet Laboratory as possible candidates for the Thomson scattering submillimeter laser are listed. CH_3F and D_2O were studied because they produce the strongest submillimeter laser emissions, and CH_3I was studied because it has the narrowest superradiant linewidth. CH_3I currently is not considered a likely candidate because of its weak emissions. CH_3F and D_2O are more desirable because of their strong submillimeter emissions, but both have a broad superradiant linewidth which requires the use of a laser cavity.

Originally much attention was given to the CH_3F laser at the National Magnet Laboratory,[57, 58] and currently much attention is given elsewhere[59-61] to this gas as a very likely candidate for the Thomson scattering submillimeter laser. However, we now feel that D_2O will make a better laser and are concentrating our research effort on this gas. The problem with the CH_3F is that it is a symmetric rotor and the K-level spacing around any one J-level is small. Consequently, the homogeneously broadened CO_2 P(20) laser line at 9.55 μm can pump as many as six K-levels simultaneously, and may produce FIR radiation within a 1 GHz bandwidth. This inefficient pumping of the J-level makes it extremely difficult to develop an efficient single longitudinal mode CH_3F oscillator. Furthermore, in an oscillator-amplifier combination the simultaneous pumping of many K-levels in the amplifier produces broad bandwidth mirrorless laser action which adds a large superradiant background to the oscillator-amplifier signal. This is probably the major reason why a high power CH_3F laser without superradiance has not been developed yet. This problem might be investigated if a narrow linewidth CO_2 laser is used, but such a laser with enough energy to pump a 1 MW submillimeter laser has not yet been demonstrated, though there is some encouraging work in this area with lower energy pulsed CO_2 lasers.[62, 63] However, off resonance pumping would probably still lead to pumping of a number of nearby levels.

The advantage of D_2O (asymmetric rotor) is that its rotational level spacing is large enough so that a TEA CO_2 laser will only pump one transition. It should therefore be much easier to eliminate superradiance. An ther advantage of D_2O is that it appears, experimentally, to have a higher conversion efficiency of CO_2 laser pump energy to submillimeter energy. Possibly this is also a result of pumping only one transition. The shorter wavelength of D_2O submillimeter emission can also be considered an advantage over CH_3F if the Thomson scattering is being done in a plasma in a high magnetic field because the scattered signal will be further away in frequency from cyclotron harmonics noise. For these reasons we have concentrated most of our recent effort to develop a D_2O submillimeter laser for the Thomson scattering plasma diagnostic experiment.

D_2O though, is not without its own problems. Figure 44 shows an energy level diagram of the D_2O levels involved in the submillimeter laser emissions. As shown there, the center of the CO_2 pump line at 9.26 μm is not exactly at the same frequency as the pump transition of D_2O. They are offset by 318 MHz. When the CO_2 pumping is intense this gives rise to a Raman transition on the 385 μm line which is 318 MHz lower in frequency than the line center transition. This effect has been observed experimentally and is shown in Figure 45. There the curves represent Fabry-Perot scans of D_2O superradiance at 385 μm. The Fabry-Perot had a free spectral range of 1.24 GHz and each scan shown goes through two orders, i.e., the second peak is a repeat of the first. A number of scans were taken at different pressures in the range of 0.08 and 10.63 Torr. All these scans are aligned horizontally so that the vertical dashed line intersects the same frequency in each curve. From these curves it is evident that for a pressure between 0.5 and 0.91 Torr the D_2O laser emission switches in frequency by about 320 MHz. R.J. Temkin[55] has identified the superradiance at low pressure to be due to the line center transition and at high pressure to be due to the Raman transition.

67

The effect illustrated in Figure 45 is not unique to D_2O. Other gases also exhibit a Raman transition off line center under intense optical pumping when the pumping frequency is not the same as the pumped transition. Yet it has only been during the past year that these transitions have been first observed in optically pumped submillimeter lasers. It is important to understand these effects from the laser development point of view. For example, if one builds an oscillator-amplifier submillimeter laser system and the conditions in the oscillator are not the same as in the amplifier, it is possible that the two could be operating at different frequencies even though they may be raidating on the same transition. New theories are being developed to understand the pyisics of intense optically pumped submillimeter lasers.[55, 64]

Laser Modes: Before going on to describe the various submillimeter laser designs that have been built and tested it is worthwhile to review the basic features of laser cavity modes.[65] There are two types of modes, transverse and longitudinal. Simultaneous oscillation in several of these modes is undesirable because they cause increased linewidth, and in the case of higher order transverse modes increased laser beam divergence. In optically pumped submillimeter lasers transverse modes do not present as serious a problem as longitudinal modes. Transverse modes can be eliminated by using apertures. If the laser cavity has flat mirrors then the presence of the transverse modes will not add significantly to the linewidth, and in that case their presence may be tolerated if they do not cause the laser beam to become too divergent.

Multiple longitudinal modes on the other hand, must be avoided. The increase in overall linewidth caused by additional longitudinal modes cannot be tolerated when using the laser for Thomson scattering plasma diagnostics. The effect of longitudinal modes on the laser output is illustrated in Figure 46. The modes are separated in frequency by $c/2L$ where c is the speed of light and L is the length of the cavity. The gain of the laser medium will usually be positive for a number of the modes and therefore, the laser output will look like the bottom set of lines. It should be noted that the superradiant output would look like the laser gain curve.

68

Multiple longitudinal mode operation can be eliminated in several ways. The easiest is to use a short enough oscillator so that the spacing between modes is larger than the laser gain profile. This requires cavities less than 50 cm long in the case of optically pumped submillimeter lasers. Other methods are to use an internal mode selector or injection locking where the laser emissions of a short oscillator are used to control the frequency output of a long oscillator that normally operates on several modes. All these methods have been tried and will be reviewed in the next part.

C. LASER SYSTEM DESIGNS

All the laser systems to be described here were operated with D_2O gas oscillating at a wavelength of 385 μm. All the systems also used the same TEA CO_2 pump laser which consisted of a Lumonics #103 oscillator and #601 amplifier stage. The CO_2 oscillator beam made a triple pass through the amplifier and was expanded from a 3 cm diameter beam to a rectangular beam of about 7 x 8 cm. The CO_2 laser pulses were 60 ns long between half power points and had a low intensity tail lasting over 1 μs if nitrogen gas was added to the oscillator. The laser energy output of the amplifier with the oscillator tuned to the 9.26 μm R(22) line was usually 11 Joules without nitrogen in the oscillator and 21 Joules with nitrogen. These energy values were at times measured to be as large as 15 and 31 Joules respectively under optimum conditions. In the following system description the CO_2 oscillator was run without nitrogen unless otherwise stated.

C1. Oscillator and Amplifier

Figure 47 shows the first D_2O laser system built and tested.[66] It consisted of a short oscillator with a 36 cm long cavity to insure single longitudinal mode operation and an 8 m long amplifier. Both were constructed of 10 cm internal diameter

pyrex glass pipe. NaCl windows were used for the CO_2 laser pump and teflon windows were used for the submillimeter radiation.

The CO_2 laser pump beam was split so that 20% pumped the oscillator and 80% pumped the amplifier. In the oscillator the CO_2 laser beam had to pass through two copper meshes which caused losses that resulted in only 30% of the CO_2 laser energy incident on the oscillator actually pumping the cavity. The purpose of the mesh at 45° to the CO_2 laser beam was to pass the pump beam and reflect the submillimeter laser beam. This mesh was a 250 lines per inch copper mesh which was measured to have a reflectivity of 85% at 45° incidence for the 385 μm. At the other end of the cavity was a 10 m radius of curvature gold coated mirror. This oscillator produced single mode pulses at 385 μm with energies of about 1 mJ corresponding to a peak power level of about 15 KW. There was also some weak emission at 359 μm due to the cascade transition in D_2O (see Fig. 44).

The amplifier used a crystal quartz plate for coupling in the CO_2 laser beam. At the CO_2 laser wavelength of 9.26 μm crystal quartz has a reflectivity of 85% for an incident angle of 45°. The submillimeter losses for transmission through the same plate was only about 10%. The ability to use crystal quartz as a CO_2 laser beam coupler in this way is another advantage of using D_2O as the submillimeter laser medium.

With the oscillator optimally tuned, the total submillimeter energy output of the amplifier was 16.8 mJ of which 12.7 mJ was due to the 385 μm transition and the rest to the 359 μm transition. Submillimeter energy was measured with a pyroelectric detector. The D_2O operating pressure of the amplifier was 4.0 Torr and for the oscillator it was 5.5 Torr. The efficiency for converting CO_2 energy to submillimeter energy at 385 μm was calculated to be 0.11% without taking into account loss of CO_2 or submillimeter laser radiation at windows or couplers.

A Schottky diode detector was used to measure the submillimeter pulse length. It was determined to be about 65 ns. The resulting peak power level at

385 μm was therefore 195 KW. A polarization measurement was also made which showed that only 70% of the 385 μm laser emission was polarized perpendicular to the CO_2 laser pump beam. In the Thomson scattering plasma diagnostic experiment the detector will be sensitive only to one polarization so that a submillimeter laser not completely polarized in one direction will be wasting energy.

Fabry-Perot scans of the amplifier output were made and are shown in Figure 48. The lower scan shows the spectral distribution of the superradiant emission of the amplifier with no oscillator input. The 385 μm line has a FWHM of 450 MHz. The upper scan shows the amplifier output with the oscillator on. The FWHM of the 385 μm transition narrows to 70 MHz, but the superradiance is not eliminated and, therefore, this peak rests on a nearly flat background of large bandwidth superradiant emission. There is also some 359 μm radiation from the oscillator seen amplified in this scan. The presence of the 359 μm emission in the laser output will not affect the Thomson scattering experiment because the heterodyne detector will not be sensitive to that wavelength, but the presence of the superradiant background is unacceptable. Delaying pumping of the amplifier relative to the oscillator did not help to eliminate the superradiance. This result demonstrates another problem of D_2O which is the saturation intensity of the 385 μm transition is very high. This problem can only be overcome if a higher power narrow linewidth submillimeter oscillator at 385 μm is developed.

C2. Short Oscillator

Fabry-Perot scans of the output of the 36 cm long oscillator showed no evidence of superradiant emission. Figure 49 shows such a scan where the single mode output of the oscillator at 385 μm appears to satisfy the linewidth requirements for Thomson scattering plasma diagnostics. As stated earlier the presence of the 359 μm emission will not interfere with the Thomson scattering experiment.

71

Encouraged by the good linewidth quality of the short oscillator we used all of the available CO_2 laser energy to pump it. By doing this we were able to increase the oscillator output at 385 μm from about 15 to 50 KW and still maintain operation on a single mode with little evidence of a superradiant background. With 100% of the CO_2 laser pump energy the optimum D_2O pressure in the oscillator increased to 11 Torr. The higher D_2O pressure caused pulse lengths to be slightly shorter, between 50 and 60 ns. The energy conversion efficiency of CO_2 laser energy to submillimeter energy was only 0.03%, but if CO_2 beam insertion losses through the two meshes is taken into account it was about 0.1%.

Further experimentation showed that this was the best we could do with the short oscillator. Using a higher reflectivity front mesh, about 60%, caused the oscillator output to become multimodal. The submillimeter output energy at 385 μm did increase to about 65 KW, but because at least two different longitudinal modes were present the linewidth at one tenth maximum was over 400 MHz. CO_2 laser pump energy was attenuated until only one mode was present in the submillimeter output. The output became single mode when the CO_2 was attenuated by 25%, but the submillimeter energy output dropped to below 50 KW. An attempt to make the short oscillator a bigger diameter also failed to increase power because diverging the CO_2 beam to pump a larger area decreased the pumping efficiency.

C3. Injection Oscillator

A long oscillator can produce more power than a short oscillator, but the output will be in several longitudinal modes. One possible way to eliminate multimodal operation of long oscillators which has worked with pulsed CO_2 lasers[63] is to inject a signal of the desired frequency into the long cavity before it is pumped. If this signal is in resonance with one of the laser modes it will cause that mode to oscillate first and deplete the gain of the transition before the other modes can build up. It practice this technique did not work very well.

Figure 50 shows the experimental arrangement for trying this technique.
It is nearly identical to the oscillator-amplifier setup of Figure 47, except now the
amplifier has been converted into a 1.55 m long oscillator. The single mode output
of the short oscillator is tuned to be in resonance with one of the modes of the long
oscillator. The short oscillator laser beam is directed into the long cavity through
a mesh beam splitter. The purpose of the beamsplitter is to couple out the long
oscillator output.

The effect of injection locking is shown in Figure 51. A continuous
Fabry-Perot scan with a free spectral range of 650 MHz is shown there. The
left side of the curve represents the output of the long oscillator without a signal
from the short oscillator. There are several longitudinal modes separated by
97 MHz present in the output. The ones labeled with Roman numerals are due to
the 385 μm transition and the ones labeled with letters are due to the 359 μm
transition. When a signal from the short oscillator is injected into the long oscillator
the right side of the curve shows that one of the 385 μm modes is strongly enhanced,
but the other modes are not completely eliminated. The result shows that injection
locking will not be adequate for the Thomson scattering laser.

C4. Fox-Smith Oscillator

Another method for eliminating multiple longitudinal mode operation of a
laser is to use an internal mode selector. One that has been successful with visible
lasers is known as a Fox-Smith mode selector.[67] Figure 52 shows an oscillator
configuration which applies this technique to the submillimeter region. The
Fox-Smith mode selector consists of a wire mesh beam splitter and two flat mirrors
at one end of the laser. Together these components form an end mirror for the long
laser cavity which is highly reflecting back down the cavity only for particular
frequencies. The Fox-Smith mode selector can be thought of as a short L-shaped

Fabry-Perot cavity which is tuned by translating the side mirror to be in resonance with one of the modes of the main laser cavity. That mode will not see the mesh beamsplitter and will be reflected normally by the end flat mirror. Other modes and superradiant emission not in resonance with the Fox-Smith cavity will see the mesh and be reflected out of the main laser cavity into the submillimeter dump. The useful output of the laser is coupled out of the other end of the laser cavity through a mesh mirror.

The selectivity of the Fox-Smith mode selector depends on the reflectivity of the beamsplitter. In visible lasers it is usually about 50%, but working with the D_2O submillimeter laser we found we needed a beamsplitter with a reflectivity of 85% to discriminate against adjacent logitudinal modes separated by 94 MHz for a 1.6 m long cavity. The length of the L-shaped Fox-Smith cavity was chosen to be about 30 cm long so that the resonances of that cavity were separated by 500 MHz. This insured that the adjacent resonances of the Fox-Smith mode selector would not be in resonance with a longitudinal mode of the main cavity when a mode near the center of the D_2O gain profile was selected.

A further improvement made in the submillimeter oscillator of Figure 52 is the method for optical pumping. A crystal quartz plate was placed inside the laser cavity so that the CO_2 laser pump beam could be coupled into the cavity without any transmission losses through meshes. The submillimeter wave losses because of having the quartz inside the cavity were less than the losses due to decreased pumping efficiency when the quartz was outside of the cavity. This method for optical pump coupling could not be used with submillimeter lase gases other than D_2O that use a different CO_2 pump transition because the quartz would need a special coating to be reflective to the other CO_2 laser transitions. It has been our experience that such coatings increase the losses to the submillimeter radiation and preclude the possibility of placing the quartz into the cavity.

The spectral output of this oscillator with and without the beamsplitter of the mode selector in place is shown in Figure 53. Each of the vertical lines in the Fabry-Perot scans represents one pulse of the laser system. The laser system fires once every 10 seconds and it took 90 shots to take each Fabry-Perot scan with a free spectral range of 700 MHz shown in Figure 53. The left scan without the mode selector shows the 1.6 m long oscillator operating on a number of longitudinal modes for each of two different transitions (385 μm, 359 μm) and a nonzero superradiant background. With the mode selector only one longitudinal mode at 385 μm is present in the laser output. This mode has a linewidth of 25 MHz at half maximum, 120 MHz at one tenth maximum, and apparently no significant superradiant emission. Also, the intensity of this mode is a factor of three greater than any one mode without the mode selector, meaning that the conversion efficiency of CO_2 laser energy to submillimeter energy will not be too much worse with the mode selector than without. This is a consequence of using a mode selector internal to the cavity because unwanted modes are not allowed to build up and share the available energy.

For a CO_2 pump energy of 11 joules the output energy at 385 μm was 5.7 millijoules. The efficiency of the Fox-Smith mode selector oscillator was therefore about 0.05% or half that of the oscillator amplifier system. This is not a bad result and together with the good linewidth quality made the oscillator with the Fox-Smith mode selector the most promising design for the Thomson scattering laser. A detailed study was next carried out to see how this design might be scaled.

Figure 54 shows submillimeter laser output energy as a function of D_2O pressure in the Fox-Smith oscillator for a number of different CO_2 pump energies. The Fox-Smith oscillator was operating one one mode for these measurements. The optimum D_2O pressure increases with increasing pump intensity. At a CO_2 pump energy of 2.8 joules the optimum pressure is about 3.0 Torr and at 11 joules

it increases to about 6.0 Torr. When nitrogen is added to the CO_2 laser oscillator to increase the pump energy to 21 Joules the optimum D_2O pressure decreases to about 4.5 Torr. This result can be expected if the low intensity tail of the CO_2 laser pulse, present when nitrogen is added to the oscillator, pumps the D_2O to emit a low intensity submillimeter tail. The four curves taken at lower CO_2 pump energies imply that the optimum D_2O pump pressure for decreasing CO_2 pump intensity decreases and therefore, when nitrogen is added to the CO_2 oscillator the optimum D_2O pressure should also decrease.

This interpretation of the D_2O pressure scans is supported by the data shown in Figure 55. There time resolved photographs of the CO_2 and D_2O laser pulses are shown for the two cases of with and without nitrogen in the CO_2 oscillator. The corresponding D_2O pressure was 6.0 and 4.5 Torr respectively. The CO_2 laser pulses were taken with a photon drag detector and the D_2O laser pulses with a Schottky diode. The vertical scales of the two D_2O laser pulse pictures are the same because extra attenuation was used in front of the Schottky diode when nitrogen was added to the CO_2 oscillator. This was done to prevent saturation and to insure against possible damage to the diode by a too intense submillimeter pulse. These pictures clearly show that the submillimeter pulse follows the CO_2 pump pulse and when the CO_2 pulse has a tail so does the D_2O pulse.

Another important feature of these pictures is that there is no evidence of a bottleneck effect. The existence of a long tail in the D_2O submillimeter pulse corresponding to the CO_2 laser pump pulse may be evidence that the vibrational relaxation time of D_2O may be fast enough for this submillimeter laser to operate CW if a CW pump source at the right frequency could be found. Increased resolution of the CO_2 and D_2O pulses is shown in Figure 56. The CO_2 laser pulse shows structure due to multimodal operation while the single mode D_2O pulse is relatively smooth with some structure that appears to correspond to the pump pulse. The

submillimeter pulse is 80 ns long at half maximum which is a little longer than the 60 ns long CO_2 pulse.

For the Thomson scattering laser we will want a pulse at least 200 ns long. It appears from the data of Figures 55 and 56 that if a CO_2 pump laser with a pulse length 200 ns is used then this goal can be achieved. The smoothness of the submillimeter pulse can also be improved if a single mode CO_2 laser is used. This can be done by also using a mode selector in the CO_2 oscillator.

Linewidth, pulse length, and submillimeter energy output of the Fox-Smith oscillator are plotted in Figure 57 as a function of CO_2 laser pump energy to show how this design will scale. Each of these parameters was measured at the optimum D_2O pressure for the given optical pump energy as determined in Figure 54. Submillimeter energy increases linearly with CO_2 pump energy for the range of CO_2 pump energy used. Every two joules of CO_2 pump energy produces one millijoule of submillimeter energy corresponding to an energy conversion efficiency of 0.05%. There is no evidence of saturation or bottlenecking up to a pump energy of 23 joules and a submillimeter energy of 9.5 mJ. The reason that the two points for pumping energies greater than 20 joules fall below the line is because nitrogen had to be added to the CO_2 oscillator to attain those energies. The resulting low intensity tail in the CO_2 laser pulse pumps the D_2O vapor with less efficiency. Therefore, displacement of those points from the line is probably representative of the CO_2 energy in the tail and not evidence of saturation.

To further support this argument the CO_2 laser beam was focussed with a long focal length mirror so that roughly half the original volume of the Fox-Smith oscillator was pumped with the same CO_2 energy. For a CO_2 pumping energy of 11 joules this doubled the pump intensity from 2.7 MW cm^{-2} to 5.4 MW cm^{-2}. The points marked with an X show the resulting submillimeter energy for focussing the CO_2 pump beam. Even though the volume of D_2O vapor used was halved

the submillimeter energy actually increased with increasing pump intensity. This not only demonstrates improved efficiency with increasing CO_2 pump intensity, but further shows the absence of a bottleneck effect. Based on this submillimeter energy data it appears that scaling to higher CO_2 pump energies and intensities will increase the submillimeter energy output with slightly improved efficiency.

The pulse length and linewidth of the Fox-Smith oscillator also appear to increase with increasing CO_2 pump energy. In the case of pulse length this is a desirable feature. It demonstrates that scaling to higher energies is not inconsistent with longer pulses. Though increasing linewidth with CO_2 pump energy is not desirable the rate of increase is not serious. For an increase in pump energy from 2.8 to 21 joules the linewidth increases only from 125 to 145 MHz at one tenth maximum. This linewidth can be further controlled by the reflectivity of the front mesh mirror. The linewidth at one tenth maximum was reduced to 100 MHz by increasing the reflectivity of the front mesh from 60% to 70% as shown in Figure 56. The submillimeter energy did drop by about 30% for the higher reflectivity front mesh so that narrower linewidth is obtainable at the expense of efficiency.

The Fox-Smith oscillator not only has a narrow linewidth but it is also 90% polarized horizontally. This is due to the quartz plate in the oscillator cavity which preferentially increases the losses for the vertical polarization. The polarization can be further improved in the future by placing the plate at Brewster's angle (64°) instead of the present 45° angle. Overall, the performance of the Fox-Smith oscillator was found to be the most encouraging of all the laser designs that we have tried. We plan to scale this oscillator for use in the final design of the 1 MW Thomson scattering laser.

D. 1 MW LASER SYSTEM

In this part we will describe how we plan to scale the 70 kW, 80 ns long pulse Fox-Smith oscillator described in Part C to a 1 MW, 200 ns long pulse laser system for Thomson scattering. The increase in pulse length can be achieved by using a CO_2 pump laser with the desired pulse length. The increased power level can be accomplished in one of two ways. One possibility is a straightforward scaling of the Fox-Smith oscillator in size and CO_2 laser pump intensity until the required submillimeter power is reached. Another way is to scale the oscillator only to power level necessary to saturate an amplifier and then scale up the amplifier to achieve the required power level. The latter alternative is more desirable because in Part C it was shown that an oscillator-amplifier combination was twice as efficient as the Fox-Smith oscillator. Making the submillimeter laser as efficient as possible will reduce the requirements of the CO_2 pump laser which will be the single most expensive item in the 1 MW submillimeter laser system.

The question, of course, is how much power at 385 μm is needed to saturate that transition in D_2O. We do not really know the answer to that question, but we do know that 100 W cm^{-2} is not enough which is approximately the intensity of the short oscillator pulse used to pump our amplifier when a superradiant component was measured in the output. Probably at least an order of magnitude of increase in the submillimeter oscillator pulse intensity will be need before we can saturate the amplifier. Whether or not an oscillator-amplifier combination will work in the final system will have to be experimentally determined. In the following it will be assumed that such a combination will work and a possible 1 MW submillimeter laser system will be described based on that assumption. It will also be shown that the Fox-Smith oscillator alone can be scaled to a 1 MW power level if one is willing to invest in a larger CO_2 pump laser. First a description of a possible CO_2 laser pump for the 1 MW submillimeter laser system will be given.

D1. CO_2 Pump Laser

To produce a 1 MW 200 ns submillimeter laser pulse 200 mJ of submillimeter energy is required. The best observed conversion efficiency of CO_2 laser energy to submillimeter laser energy was about 0.1% for the D_2O oscillator-amplifier. The Fox-Smith oscillator demonstrated an energy conversion efficiency of only 0.05%. Therefore, the CO_2 pump laser will have to provide energies of 200 to 400 Joules[68] the exact requirement depending on the final design of the submillimeter laser.

A possible CO_2 pump laser that is made up of commercially available TEA oscillator and amplifier modules and produces 270 Joule pulses at 9.26 μm is shown in Figure 59. The oscillator and amplifiers are labelled by Lumonics model numbers. The oscillator is about three meters long and controlled by a grating to oscillate on the desired CO_2 laser transition. This oscillator is modified to produce a pulse length of 200 ns or longer as required to achieve approximately a 200 ns long pulse at the output of the last amplifier stage. The amplifiers will tend to shorten the oscillator pulse as it is amplified, therefore pulse lengths much longer than 200 ns may be required from the oscillator. (It is possible to make CO_2 oscillator pulses up to several microseconds long by using large amounts of nitrogen in the oscillator gas mixture.)

The CO_2 laser beam is gradually expanded as it is amplified. At the oscillator it starts out about 3 cm in diameter, then is expanded to fill the 8 cm diameter aperture of the first amplifier and finally expanded to 20 cm in diameter to fill the aperture of the last amplifier. This is done for two reasons. One reason is to keep the amplifier chain from self-oscillating. Using large diameter amplifiers keeps the required length of the amplifier chain short which reduces the chance of self oscillations. Another reason for expanding the beam is to lower the energy density so that there is a smaller chance of damaging laser windows and mirrors.

The size of this CO_2 pump laser is large. As stated earlier the CO_2 oscillator is about 3 m in length, the 8 cm aperture amplifier is another 3 m in length, and the 20 cm aperture amplifier is about 5 m in length. To place all these modules colinearly a space about 12-14 m in length would be required. It is possible to fold the CO_2 laser setup as shown in Figure 59 which would then require a space of about 10 x 3 m^2. If more than 270 Joules of pump energy is needed for the 1 MW D_2O submillimeter laser then it would be advisable to switch to an electron beam CO_2 laser which would be a factor of 2 to 3 times more efficient than a TEA CO_2 laser. Adding additional TEA amplifier modules to the amplifier chain of Fig. 59 probably would not be possible because of self oscillation problems.

D2. Submillimeter Oscillator and Amplifier

Most of the scaling of the Fox-Smith oscillator to increased power levels can be obtained as a result of making it larger in size. The 70 KW power level measured for this Oscillator (Part C) was obtained by pumping only about a 6 cm diameter portion of the 10 cm diameter volume available. Increasing the diameter to 20 cm, about the size of the CO_2 laser pump beam, and pumping the entire volume with a CO_2 laser intensity of 5.4 MW cm^{-2} should increase the submillimeter power by a factor of eleven or to 770 KW. A further increase to 1 MW can be realized by increasing the CO_2 pump intensity to about 7.0 MW cm^{-2}. Absorption measurements of the 9.26 μm D_2O transition have been made which show that saturated absorption does not take place until power levels greater than 10 MW cm^{-2} are reached.[69] Therefore, it appears feasible that the Fox-Smith oscillator alone can be scaled to a 1 MW power level if a 400 Joule or greater CO_2 pump laser is used.

To reduce the requirements of the CO_2 pump laser it would be more desirable to scale the Fox-Smith oscillator only to about 250 KW and then try to saturate an amplifier stage. Only about 100 Joules of CO_2 laser pump energy would then be

81

required for the oscillator and only an additional 150 Joules for an amplifier stage if the amplifier has an energy conversion efficiency of 0.1% and there are no losses to the oscillator pulse. The CO_2 pump laser of Figure 59 would then be adequate and such a submillimeter oscillator-amplifier configuration is shown in Figure 60. To increase chances of saturating an amplifier the 20 cm diameter beam of the oscillator is focussed with a long focal length mirror to about 2-3 cm in diameter so that the submillimeter intensity will be about 50 KW cm^{-2} when it enters the amplifier. Inside the amplifier the oscillator beam is expanded in diameter and folded to make a triple pass through the amplifier. This is done so that as much as possible of the amplifier is saturated with submillimeter radiation of the desired frequency. It also keeps the overall length of amplifier short, which minimizes the possibility of superradiant buildup. The starting intensity of the oscillator pulse in the amplifier will be a factor of 25 times greater than ever tried before and hopefully this will saturate the 385 μm transition of D_2O.

Both oscillator and amplifier will be constructed with an internal diameter slightly greater than the 20 cm diameter CO_2 laser pump beam. Their length will be kept between 1.5 and 2.0 m the same as the length of our current Fox-Smith oscillator which showed little evidence of superradiance. Each will use a crystal quartz plate to couple in the CO_2 laser pump beam. The quartz plates will be placed at Brewster's angle, 64°, for the 385 μm radiation so that their reflection losses for the horizontal polarization is very small. This also should improve the polarization of the oscillator output to better than 90%. Because of the angle the quartz couplers have to make with respect to the oscillator and amplifier axes their dimensions must be 46 x 20 cm. Single pieces of crystal quartz this large with the optic axis inside the plane of the quartz plate are difficult to obtain. Therefore, the quartz couplers should be made of four 23 x 10 cm pieces butted together. The smaller pieces of quartz can also be made thinner to minimize submillimeter absorption losses. A thickness of about 3-4 mm would be desirable.

Whether or not a submillimeter amplifier can be saturated by a high power submillimeter oscillator still remains to be resolved. If it can a fairly efficient 1 MW submillimeter laser can be built. Otherwise, it should still be possible to scale a high power oscillator to 1 MW. After obtaining our Fox-Smith oscillator results we are very optimistic that a 1 MW submillimeter laser can be built for Thomson scattering, and we should investigate various configurations to maximize efficiency.

SUMMARY OF RESULTS

High power submillimeter (SMM) laser Thomson scattering is a prom-
ising technique for the measurement of ion temperature in plasmas. Further-
more, useful information may be obtained about the presence of high atomic
number highly ionized impurities polluting the plasma, and in large volume
plasmas measurement with spatial resolution may be feasible.

The physical principles of this technique are very simple but its practical
implementation is rather involved and requires development of the state of the
art in high power narrow linewidth SMM lasers, low noise SMM receivers,
and data collection and processing. The measurement of T_i works as follows:
A high power, highly monochromatic and well collimated SMM laser beam
illuminates the plasma to be studied and is scattered by the thermal random
electron density fluctuations. The scattered electromagnetic wave will be
doppler shifted in frequency by an amount proportional to the electron speed
and its amplitude will be proportional to the local electron density inhomogene-
ity. The scattered signal at any one time will be random since the electron
motion and the density fluctuations are random. Sampling the scattered signal
for a long enough time ($\geq$ 200 nsec) will allow us to estimate some of its
statistical properties. The power spectral density is the function that is used
to infer the plasma parameters, although other moments of the distribution
may also be useful. Two further requirements are necessary to insure that
we measure T_i: 1)   the experiment must be set up so we measure an electron
density fluctuation wavelength that is larger than (2π) (Debye shielding radius),
and 2) the ratio of the electron to the ion temperature is less than two. In
this case we will mostly measure the ion density fluctuations since they are
being effectively shielded by the highly mobile electrons. Spectral density

84

calculations carried out for simple plasmas are instrumental in setting guide-
lines for the specifications of the SMM laser and receiver. We also identify
the optimal signal processing and analyze various suboptimal alternatives.

For the feasibility of the experiment, the following is a summary of the
components specifications.

SMM laser power	1 MW
10 db laser bandwidth	100 MHz
Laser pulse length	200 nsec.
Laser frequency	600 - 800 GHz
Receiver noise	10^{-18} to 10^{-19} W/Hz
Scattering angle	20° to 30°
IF amplifier gain	70 db
IF amplifier bandwidth	1 to 2 GHz
IF frequency	5 to 15 GHz
IF amplifier noise	120 to 200 K

Furthermore, it is required that the SMM laser and the SMM receiver each
looks into a signal dump with an absorption of 99.99%.

The focussing and collection optics are considered on general terms with
the purpose to establish estimates for the laser beam diameter (1.5 cm), solid
angle of acceptance (5×10^{-3} sr), scattering angle spread (3°), and plasma noise
volume (15 to 30 cm^3). Bremsstrahlung radiation noise is negligible.

Finally, a review of the CO_2 pumped molecular gas lasers indicate that
the 385 μm transition of D_2O is highly promising both for the power levels
necessary and the spectral purity.

REFERENCES

1. F. Villars and V.F. Weisskopf, "On the Scattering of Radio Waves by Turbulent Fluctuations of the Atmosphere," Proc. IRE 43, 1232 (1955).

2. J.P. Dougherty and D.T. Farley, "A Theory of Incoherent Scattering of Radio Waves by a Plasma. I," Proc. Roy. Soc. (London) A259, 79 (1960).

3. D.T. Farley, J.P. Dougherty and D.W. Barron, "A Theory of Incoherent Scattering of Radio Waves by a Plasma II. Scattering in a Magnetic Field," Proc. Roy. Soc. (London) A263, 238 (1961).

4. J.P. Dougherty and D.T. Farley, "A Theory of Incoherent Scattering of Radio Waves by a Plasma III. Scattering in a Partly Ionized Gas," J. of Geophysical Research 68, 5473 (1963).

5. D.T. Farley, "A Theory of Incoh ent Scattering of Radio Waves by a Plasma 4. The Effect of Unequal Ion and Electron Temperatures," J. of Geophysical Research 71, 4091 (1966).

6. E.E. Salpeter, "Electron Density Fluctuations in a Plasma," Phys. Rev. 120 1528 (1960).

7. E.E. Salpeter, "Plasma Density Fluctuations in a Magnetic Field," Phys. Rev. 122, 1663 (1961).

8. E.E. Salpeter, "Density Fluctuations in a Nonequilibrium Plasma," J. of Geophysical Research 68, 1321 (1963).

9. M.N. Rosenbluth and N. Rostoker, "Scattering of Electromagnetic Waves by a Nonequilibrium Plasma," Physics of Fluids 5, 776 (1962).

10. G. Bekefi, "Radiation Processes in Plasmas," John Wiley and Sons, Inc. 1966.

11. J. Sheffield, "Plasma Scattering of Electromagnetic Radiation," Academic Press, New York 1975.

12. R.H. Huddlestone and S.L. Leonard (Editors), "Plasma Diagnostic Techniques," Academic Press, New York 1965.

13. W. Lochte-Holtgreven (Editor), "Plasma Diagnostic," North-Holland Publishing Co., Amsterdam 1968.

14. C. DeWitt and J. Peyraud (Editors), "Plasma Physics," 1972 Les Houches Lectures, Gordon and Breach Science Publishers, New York 1975.

15. B.J. Rye and J.C. Taylor (Editors), "Physics of Hot Plasmas," Scottish Universities Summer School 1968, Plenum Press, New York 1970.

16. B. Harbecke and A. Stahl, "Light Scattering and the Microscopic Theory of Driven Noise," Z. Physik B24, 315 (1976).

17. E. Parzen, "Modern Probability Theory and its Applications," John Wiley and Sons, Inc. 1960.

18. W. Bernard and H.B. Callen, "Irreversible Thermodynamics of Nonlinear Processes and Noise in Driven Systems," Reviews of Modern Physics 31, 1017 (1959) and references therein.

19. J.J. Reinmann, M.R. Lauver, R.W. Patch, S.J. Posta, A. Snyder and G.W. Englert, "Hot Ion Plasma Heating Experiments in SUMMA," IEEE Trans. Plasma Science PS-3, 6 (1975).

20. J.J. Reinmann, R.W. Patch, M.R. Lauver, G.W. Englert and A. Snyder, "SUMMA Hot-ion Plasma Heating Research at NASA Lewis Research Center," NASA Technical Memorandum, NASA TMX-71840 (1975).

21. M. Rosenbluh, R.J. Temkin and K.J. Button, "Submillimeter Laser Wavelength Tables," Applied Optics 15, 2635 (1976).

22. J.J. Gallagher, M.D. Blue, B. Bean and S. Perkowitz, "Tabulation of Optically Pumped Far Infrared Laser Lines and Applications to Atmospheric Transmission," Infrared Physics 17, 43 (1977).

23. A.E. Costley, R.J. Hastie, J.W.M. Paul and J. Chamberlain, "Electron Cyclotron Emission from a Tokamak Plasma: Experiment and Theory," Phys. Rev. Lett. 33, 758 (1974).
Also A.E. Costley, private communication.

24. D.S. Komm, "Cyclotron Radiation in a Hot Dense Plasma," Ph.D. Thesis submitted to the Massachusetts Institute of Technology, June 1976. Unpublished.

25. D.A. Boyd, C.M. Celata and F.J. Stauffer, "Submillimeter Background Emission from Tokamaks." Unpublished.

26. J.D. Kraus, "Radio Astronomy," McGraw-Hill, Inc. 1966, p. 157, Eq. 6-15.

27. A.E. Siegman, "The Antenna Properties of Optical Heterodyne Receivers," Proc. IEEE 54, 1350 (1966).

28. S. Goldman, "Information Theory," Dover Publications, Inc., N.Y. 1968.

29. R. Bracewell, "The Fourier Transform and its Applications," McGraw-Hill Book Company, N.Y. 1965, p. 339.

30. R.B. Blackman and J.W. Tukey, "The Measurement of Power Spectra," Dover Publications, Inc., N.Y. 1959.

31. W.A. Fuller, "Introduction to Statistical Time Series," John Wiley and Sons, New York 1976.

32. P. Bloomfield, "Fourier Analysis of Time Series: An Introduction," John Wiley and Sons, New York 1976.

33. E.R. Kanasewich, "Time Sequence Analysis in Geophysics," Second Revised Edition, University of Alberta Press, Canada 1975.

34. H.T. Fetterman: Private Communication.

35. J.J. Gustineic: Private Communication.

36. M. Born and E. Wolf, "Principles of Optics," Pergamon Press, New York, Fifth Ed. 1975, p.441.

37. A.F. Kay, "Millimeter Wave Antennas," Proc. IEEE 54, 641 (1966).

38. J.K. McLeod, "The Axicon: A New Type of Optical Element," J. Optical Soc. America 44, 592 (1954).

39. S.A. Ramsden and W.E.R. Davies, "Observation of Cooperative Effects in the Scattering of a Laser Beam from a Plasma," Phys. Rev. Lett. 16, 303 (1966).

40. G.W. Chantry, "Submillimeter Spectroscopy," Academic Press, New York 1971, p.341.

41. Ibid.

42. L.C. Robinson, "Physical Principles of Far-Infrared Radiation," Academic Press, New York 1973, p. 99.

43. M.N. Afsar, J. Chamberlain and G.W. Chantry, "High-Precision Dielectric Measurements on Liquids and Solids at Millimeter and Submillimeter Wavelengths," IEEE Trans. Inst. and Meas. IM-25, 290 (1976).

44. J.M. Aaron, C.L.M. Ireland, C. Grey Morgan, "Aberration Effects in the Interaction of Focused Laser Beams with Matter," J. Phys. D: Appl. Phys. 7, 1907 (1974).

45. M. Born and E. Wolf, "Principles of Optics," Pergamon Press, New York, Fifth Ed. 1975, p. 228.

46. Ibid, p. 395.

47. Special Optics Bulletin 103, "Diffraction Limited Optics," Little Falls, N.J.

48. H.J. Kunze in "Plasma Diagnostics," W. Lochte-Holtgreven (Editor), North Holland Publishing Co., Amsterdam 1968.

49. R. Protz, F. Soldner and K.H. Stever, "Multichannel Laser Light Scattering Diagnostics for Density Profile Measurements in Belt Pinch Plasmas," J. Appl. Phys. 48, 125 (1977).

50. S.A. Ramsden and W.E.R. Davies, "Observation of Cooperative Effects in the Scattering of a Laser Beam from a Plasma," Phys. Rev. Lett. 16, 303 (1966).

51. "Reference Data for Radio Engineers," Howard W. Sams and Co., Inc., Indianapolis, Fifth Ed. 1972, p. 4-28.

52. T.Y. Chang and T.J. Bridges, "Laser Action at 452, 496 and 541 μm in Optically Pumped CH_3F," Optics Comm. 1, 423 (1970).

53. D.L. Jassby, D.R. Cohn, B. Lax and W. Halverson, "Tokamak Diagnostics with the 496 μm CH_3F Laser," Nucl. Fusion 14, 745 (1974).

54. R.J. Temkin and D.R. Cohn, "Rate Equations for an Optically-Pumped, Far-Infrared Laser," Optics Comm. 16, 213 (1976).

55. R.J. Temkin, "Theory of Optically Pumped Submillimeter Lasers," IEEE J. Quan. Electronics QE-13, 450 (1977).

56. M. Rosenbluth, R.J. Temkin and K.J. Button, "Submillimeter Laser Wavelength Tables," Appl. Optics 15, 2635 (1976).

57. D.R. Cohn, T. Fuse, K.J. Button, B. Lax and Z. Drozdowicz, "Development of an Efficient 9 KW 496 μm CH_3F Oscillator," Appl. Phys. Lett. 27, 280 (1975).

58. Z. Drozdowicz, R.J. Temkin, K.J. Button and D.R. Cohn, "Efficient High-Power CH_3F Amplifier for a 496 μm Cavity Laser," Appl. Phys. Lett. 28, 328 (1976).

59. A. Sement and N.C. Luhmann Jr., "High Power Narrow-Line Pulsed 496 μm Laser," Appl. Phys. Lett. 28, 659 (1976).

60. F. Brown, P.D. Hislop and S.R. Kronhein, "Characteristics of a Linearly Pumped Laser Oscillator-Amplifier at 496 μm," Appl. Phys. Lett. 28, 654 (1976).

61. D.E. Evans, L.E. Sharp, W.A. Peebles and Gary Taylor, "A High-Intensity Narrow Bandwidth Pulsed Submillimeter Laser for Plasma Diagnostics," IEEE J. Quan. Electronics QE-13, 54 (1977).

62. A. Gondhalekar, N.R. Heckenberg and E. Holzhauer, "The Mechanism of Single-Frequency Operation of the Hybrid-CO_2 Laser," IEEE J. Quan. Electronics QE-11, 103 (1975).

63. Pierre Andre Belanger and Jacques Boivin, "Gigawatt Peak-Power Pulse Generation by Injection of a Single Short Pulse in a Regenerative Amplifier Above Threshold (RAAT)," Canadian J. Phys. 54, 720 (1976).

64. R.L. Panock and R.J. Temkin, "Interaction of Two Laser Fields with a Three Level Molecular System," IEEE J. Quan. Electronics QE-13, 425 (1977).

65. H. Kogelnik and T. Li, "Laser Beams and Resonators," Proc. IEEE 54, 1312 (1966).

66. P. Woskoboinkow, Z. Drozdowicz, K. Isobe, D.R. Cohn and R.J. Temkin, "A High Power, Narrow Linewidth D_2O Laser at 384.6 μm," Phys. Lett. 59A, 264 (1976).

67. P.W. Smith, "Mode Selection in Lasers," Proc. IEEE 60, 422 (1972).

68. M.C. Richardson, A.J. Alcock, K. Leopold and P. Burtyn, "A 300 J Multigagawatt CO_2 Laser," IEEE J. Quan. Electronics QE-9, 236 (1973).

69. V.N. Bagratashvili, I.N. Knyazev, V.S. Letokhov and V.V. Lobko, "Optoacoustical Detection of Multiple Photon Molecular Absorption in a Strong IR Field," Optics Comm. 18, 525 (1976).

Table Ia   Debye length, L_{DEBYE}, and number of electrons within the Debye sphere, N_{DEBYE}, for various electron temperature, T_e, and electron density, N_e.

$$L_{DEBYE} \ (m) \ \alpha \ T_e^{1/2} / N_e^{1/2}$$

T_e (eV)	N_e (m^{-3})		
	10^{19}	10^{20}	10^{21}
10	7.43×10^{-6}	2.35×10^{-6}	7.43×10^{-7}
100	2.35×10^{-5}	7.43×10^{-6}	2.35×10^{-6}
1000	7.43×10^{-5}	2.35×10^{-8}	7.43×10^{-6}
10000	2.35×10^{-4}	7.43×10^{-5}	2.35×10^{-5}

$$N_{DEBYE} \ \alpha \ T_e^{3/2} / N_e^{1/2}$$

T_e (eV)	N_e (m^{-3})		
	10^{19}	10^{20}	10^{21}
10	1.72×10^{4}	5.44×10^{3}	1.72×10^{3}
100	5.44×10^{5}	1.72×10^{5}	5.44×10^{4}
1000	1.72×10^{7}	5.44×10^{6}	1.72×10^{6}
10000	5.44×10^{8}	1.72×10^{8}	5.44×10^{7}

Table Ib   Correlation time, τ_c, calculated between the origin and the one-tenth amplitude of the correlation function for a random process with a Gaussian spectral density.

Δf_T (GHz)	τ_c (nsec)
0.6	2.5
1.0	1.5
2.0	0.8
3.0	0.5
4.0	0.35
5.0	0.3

Table II   Fractional distortion ($1/\text{Degree}^2$) of the measured spectral power density due to the finite aperture of the collection optics. For each scattering angle the bandwidth (DF/DW) is measured in units of the total bandwidth between the 10% points of the scattering power density. The scattering angle THETA (degree) is taken to be 1, 3, 10, 30, and 90. For this calculation we assume a H^+ plasma ($Z = 1$, $MI = 1.007$) with an electron density $NE = 10^{20}$ m^{-3}, a CH$_3$F high power laser (FI = 604 GHz) with an output power PI = 1 MW, a plasma scattering length $L = 10^{-2}$ m, and a solid angle of collection DOMEGA = 10^{-2} sr. For this example, the plasma frequency FPL = 89.79 GHz, the electron temperature TE = 600 eV, and the ion temperature T_i = 600 eV.

NOTE: For these normalized calculations the results are independent of the value of DOMEGA used.

NE: 1.000D+20   Z: 1.000D+00   MI(AMU): 1.007D+00   TE: 6.000D+02   TI: 6.000D+02   FI: 6.040D+02

PI: 1.000D+06   L: 1.000D-02   DOMEGA: 1.000D-02   FPL: 8.979D+01

THETA(DEGREE):	1.	3.	10.	30.	90.
DF/HW			DELTAS(1/DEGREE**2)		
-5.0000D-01	1.6493D+00	1.8372D-01	1.6374D-02	1.6533D-03	6.4559D-05
-4.7500D-01	1.1124D+00	1.2406D-01	1.1037D-02	1.0931D-03	3.0947D-05
-4.5000D-01	5.8177D-01	6.5075D-02	5.7654D-03	5.4466D-04	5.7391D-08
-4.2500D-01	8.6238D-02	9.9381D-03	8.4311D-04	3.7997D-05	-2.6115D-05
-4.0000D-01	-3.1450D-01	-3.4722D-02	-3.1391D-03	-3.6618D-04	-4.4238D-05
-3.7500D-01	-5.5031D-01	-6.1075D-02	-5.4838D-03	-5.9786D-04	-5.1190D-05
-3.5000D-01	-5.8988D-01	-6.5583D-02	-5.8774D-03	-6.2765D-04	-4.6580D-05
-3.2500D-01	-4.7581D-01	-5.2953D-02	-4.7414D-03	-5.0126D-04	-3.3956D-05
-3.0000D-01	-2.9813D-01	-3.3205D-02	-2.9711D-03	-1.1149D-04	-1.8913D-05
-2.7500D-01	-1.3404D-01	-1.4947D-02	-1.3353D-03	-1.3748D-04	-5.9058D-06
-2.5000D-01	-1.7378D-02	-1.9620D-03	-1.7190D-04	-1.3830D-05	3.2305D-06
-2.2500D-01	5.1687D-02	5.7272D-03	5.1716D-04	5.9497D-05	8.6776D-06
-2.0000D-01	6.6216D-02	9.5725D-03	8.6183D-04	9.6238D-05	1.1430D-05
-1.7500D-01	9.9734D-02	1.1079D-02	9.9686D-04	1.1064D-04	1.2506D-05
-1.5000D-01	1.0204D-01	1.1337D-02	1.0200D-03	1.1309D-04	1.2664D-05
-1.2500D-01	9.9197D-02	1.1021D-02	9.9170D-04	1.1001D-04	1.2389D-05
-1.0000D-01	9.4599D-02	1.0511D-02	9.4587D-04	1.0505D-04	1.1963D-05
-7.5000D-02	9.0042D-02	1.0004D-02	9.0041D-04	1.0013D-04	1.1542D-05
-5.0000D-02	8.6411D-02	9.6008D-03	8.6419D-04	9.6211D-05	1.1205D-05
-2.5000D-02	8.4121D-02	9.3462D-03	8.4134D-04	9.3735D-05	1.0992D-05
0.0	8.3342D-02	9.2596D-03	8.3357D-04	9.2892D-05	1.0919D-05

93

Table III   Same calculation as for Table II but TE = 4000 eV and TI = 4000 eV.

NE= 1.000D+20   Z= 1.000D+00   MI(AMU)= 1.007D+00   TE= 4.000D+03   TI= 4.000D+03   FI= 6.040D+02

PI= 1.000D+06   L= 1.000D-02   DOMEGA= 1.000D-02   FPL= 8.979D+01

THETA(DEGREE)=	1.	3.	10.	30.	90.
DF/BW			DELTAS(1/DEGREE**2)		
-5.0000D-01	1.6490D+00	1.8330D-01	1.5899D-02	1.2483D-03	-1.0257D-05
-4.7500D-01	1.1122D+00	1.2369D-01	1.0604D-02	7.3599D-04	-2.5045D-05
-4.5000D-01	5.8165D-01	6.4767D-02	5.4066D-03	2.5705D-04	-3.7108D-05
-4.2500D-01	8.6196D-02	9.72⁵4D-03	5.8710D-04	-1.6095D-04	-4.4805D-05
-4.0000D-01	-3.1449D-01	-3.4832D-02	-3.2787D-03	-4.6959D-04	-4.6939D-05
-3.7500D-01	-5.5027D-01	-6.1100D-02	-5.5221D-03	-6.2082D-04	-4.3110D-05
-3.5000D-01	-5.8986D-01	-6.5563D-02	-5.8551D-03	-6.0391D-04	-3.4118D-05
-3.2500D-01	-4.7581D-01	-5.2923D-02	-4.7017D-03	-4.6496D-04	-2.1956D-05
-3.0000D-01	-2.9815D-01	-3.3182D-02	-2.9384D-03	-2.8162D-04	-9.1741D-06
-2.7500D-01	-1.3405D-01	-1.4934D-02	-1.3145D-03	-1.1764D-04	2.0665D-06
-2.5000D-01	-1.7388D-02	-1.9537D-03	-1.5921D-04	-7.9359D-07	1.0608D-05
-2.2500D-01	5.1684D-02	5.7340D-03	5.2611D-04	6.9413D-05	1.6298D-05
-2.0000D-01	8.6219D-02	9.5792D-03	8.6958D-04	1.0520D-04	1.9608D-05
-1.7500D-01	9.9739D-02	1.1086D-02	1.0044D-03	1.1952D-04	2.1215D-05
-1.5000D-01	1.0205D-01	1.1345D-02	1.0277D-03	1.2210D-04	2.1746D-05
-1.2500D-01	9.9204D-02	1.1029D-02	9.9945D-04	1.1911D-04	2.1680D-05
-1.0000D-01	9.4607D-02	1.0518D-02	9.5361D-04	1.1415D-04	2.1?41D-05
-7.5000D-02	9.0049D-02	1.0012D-02	9.0808D-04	1.0918D-04	2.0?35D-05
-5.0000D-02	8.6?16D-02	9.6082D-03	8.7179D-04	1.0519D-04	2.0583D-05
-2.5000D-02	8.4128D-02	9.3535D-03	8.4888D-04	1.0266D-04	2.0352D-05
0.0	8.3349D-02	9.2669D-03	8.4109D-04	1.0180D-04	2.0275D-05

94

TABLE OF CONTENTS

Table IV   Same calculation as for Table II but TE = 40 eV and TI = 2000 eV.

NE= 1.000D+20   Z= 1.000D+00   MI(AMU)= 1.007D+00   TE= 4.000D+01   TI= 2.000D+03   FI= 6.040D+02

PI= 1.000D+06   L= 1.000D-02   DOMEGA= 1.000D-02   FPL= 8.979D+01

THETA(DEGREE)=	1.	3.	10.	30.	90.
DF/BW			DELTAS(1/DEGREE**2)		
-5.0000D-01	1.5967D-02	1.9298D-03	1.6586D-04	7.0429D-06	-1.0796D-05
-4.7500D-01	-5.9194D-02	-6.4675D-03	-5.8649D-04	-7.2053D-05	-1.5086D-05
-4.5000D-01	-1.1403D-01	-1.2598D-02	-1.1355D-03	-1.2946D-04	-1.7880D-05
-4.2500D-01	-1.5107D-01	-1.6742D-02	-1.5063D-03	-1.6789D-04	-1.9374D-05
-4.0000D-01	-1.7271D-01	-1.9169D-02	-1.7232D-03	-1.8992D-04	-1.9758D-05
-3.7500D-01	-1.8128D-01	-2.0138D-02	-1.8093D-03	-1.9805D-04	-1.9211D-05
-3.5000D-01	-1.7901D-01	-1.9897D-02	-1.7869D-03	-1.9464D-04	-1.7906D-05
-3.2500D-01	-1.6799D-01	-1.8680D-02	-1.6771D-03	-1.8197D-04	-1.6009D-05
-3.0000D-01	-1.5021D-01	-1.6710D-02	-1.4997D-03	-1.6215D-04	-1.3673D-05
-2.7500D-01	-1.2754D-01	-1.4192D-02	-1.2733D-03	-1.3717D-04	-1.1041D-05
-2.5000D-01	-1.0166D-01	-1.1317D-02	-1.0149D-03	-1.0885D-04	-8.2457D-06
-2.2500D-01	-7.4119D-02	-8.2548D-03	-7.3985D-04	-7.8825D-05	-5.4039D-06
-2.0000D-01	-4.6263D-02	-5.1574D-03	-4.6166D-04	-4.8540D-05	-2.6195D-06
-1.7500D-01	-1.9266D-02	-2.1550D-03	-1.9206D-04	-1.9247D-05	1.8147D-08
-1.5000D-01	5.8851D-03	6.4242D-04	5.9093D-05	8.0041D-06	2.4344D-06
-1.2500D-01	2.8379D-02	3.1445D-03	2.8371D-04	3.2349D-05	4.5683D-06
-1.0000D-01	4.7572D-02	5.2795D-03	4.7535D-04	5.3103D-05	6.3720D-06
-7.5000D-02	6.2969D-02	6.9923D-03	6.2908D-04	6.9742D-05	7.8089D-06
-5.0000D-02	7.4209D-02	8.2426D-03	7.4129D-04	8.1882D-05	8.8525D-06
-2.5000D-02	8.1046D-02	9.0032D-03	8.0955D-04	8.9264D-05	9.4854D-06
0.0	8.3341D-02	9.2585D-03	8.3246D-04	9.1741D-05	9.6974D-06

95

Table V Optimal signal/noise ratio when 10 db bandwidth (2 ΔF) is subdivided in ten parts and the data averaged within each (2 ΔF/10) spectral range. Data is collected for an interval T = 200 nsec and T = 1 μsec, and the sampling interval is given by the Nyquist criterion τ_s = 1/2 ΔF.

$$S/N = (N_T/10)^{1/2}$$

2ΔF(GHz)	T=200 nsec		T= 1μsec	
	N_T	S/N	N_T	S/N
0.5	100	3.2	500	7.1
1.0	200	4.5	1000	10
1.5	300	5.5	1500	12.2
2.0	400	6.3	2000	14.1
2.5	500	7.1	2500	15.8
3.0	600	7.7	3000	17.3

Table VI Collection optics parameters for scattering angles of 20° and 30°. $\Delta\theta_{max}$ is the angular resolution, f_1/D is the F-number of lens L_1 (see Fig. 35), f_1 is the focal length of L_1, D is the diameter of L_1, ℓ is the plasma scattering length, $\Delta\Omega$ is the solid angle of collection, and the final entry is the depth of focus of L_1.
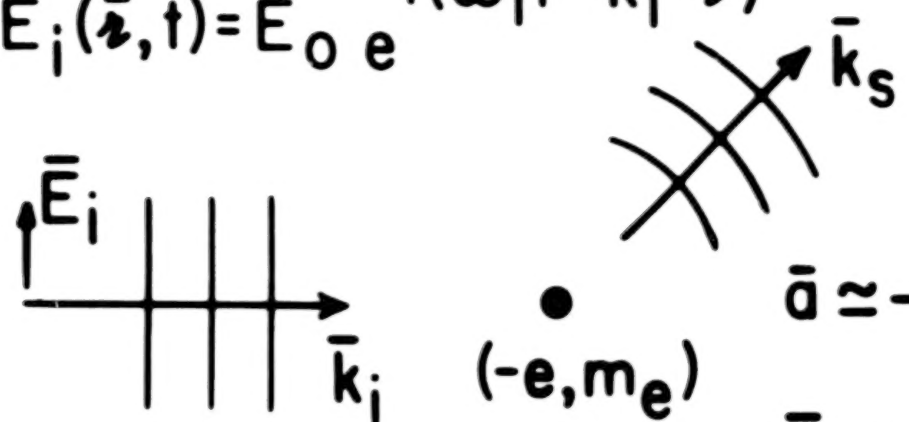
Parameter	Scattering Angle 20°	Scattering Angle 30°
$\Delta\theta_{max}$	3°	5°
f_1/D	19.1	11.5
f_1	1.0 - 1.5 m	1.0 - 1.5 m
D	5.2 - 7.9 cm	8.7 - 13.0 cm
ℓ	2.36 cm	0.97 cm
$\Delta\Omega$	2.15×10^{-3} sr	5.9×10^{-3} sr
$\ell\,\Delta\Omega$	5.07×10^{-5} m sr	5.7×10^{-5} m sr
$6.3\,\lambda\,(f_1/D)^2$	0.88 m	0.32 m

Table VII   Collection optics parameters with an axicon which has its apex angle, β, equal to the scattering angle, θ. The axicon is only a 30° arc of the total cone. $\Delta\theta_{max}$ is the angular resolution, x is the distance of the axicon from the plasma, p is the slant length of the axicon (see Fig. 36), f_1 is the focal length of the lens following the axicon, C is the maximum chord length in the axicon arc of 30°, f_1/D is the F-number of the lens following the axicon, ℓ is the plasma scattering length, $\Delta\Omega$ is the solid angle of collection, and the final entry is the depth of focus of the lens following the axicon.
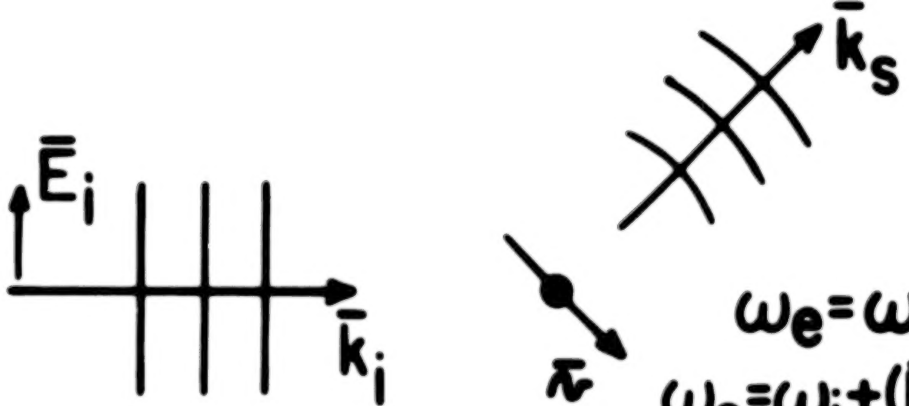
Parameter	Scattering Angle 20°	Scattering Angle 30°
$\Delta\theta_{max}$	3°	5°
x	1.2 m	1.2 m
p	0.36 m	0.40 m
f_1	1.38 m	1.40 m
C = D	22.8 cm	33.7 cm
f_1/D	6.05	4.15
ℓ	0.75 cm	0.35 cm
$\Delta\Omega$	9.4×10^{-3} sr	2.3×10^{-2} sr
$\ell\,\Delta\Omega$	6.8×10^{-5} m sr	8.0×10^{-5} m sr
$6.3\lambda\,(f_1/D)^2$	8.9 cm	4.2 cm

98

Table VIII List of various molecules that have been tested as possible candidates for the 1 MW submillimeter laser for Thomson scattering.

Molecule	CO_2 Pump Line	Submillimeter Wavelength	Relative Strength	Superradiant Linewidth (FWHM)
CH_3F	9.55 μm P(20)	496 μm	1	300 - 700 MHz
D_2O	9.26 μm R(22)	385 μm	2	300 - 700 MHz
CH_3I	10.57 μm P(18)	447 μm	0.05	100 MHz

$$\bar{E}_i(\bar{\imath}, t) = \bar{E}_0 \, e^{i(\omega_i t - \bar{k}_i \cdot \bar{\imath})}$$

$\bar{k}_s$

$\bar{E}_i$

$\bar{k}_i$

$(-e, m_e)$

$$\bar{a} \simeq -\frac{e}{m_e} \bar{E}_i$$

$$\bar{E}_s \propto \bar{a}$$

$\bar{k}_s$

$\bar{E}_i$

$\bar{k}_i$

$\bar{v}$

$$\omega_e = \omega_i - \bar{k}_i \cdot \bar{v}$$

$$\omega_s = \omega_i + (\bar{k}_s - \bar{k}_i) \cdot \bar{v}$$

Fig. 1   Sketch of the electromagnetic wave ($\bar{k}_s$, ω_s) scattered by a single electron at rest (top) or in motion with a velocity $\bar{v}$ (bottom) when subjected to the electric field $\bar{E}_i$ of an incoming plane wave ($\bar{k}_i$, ω_i).
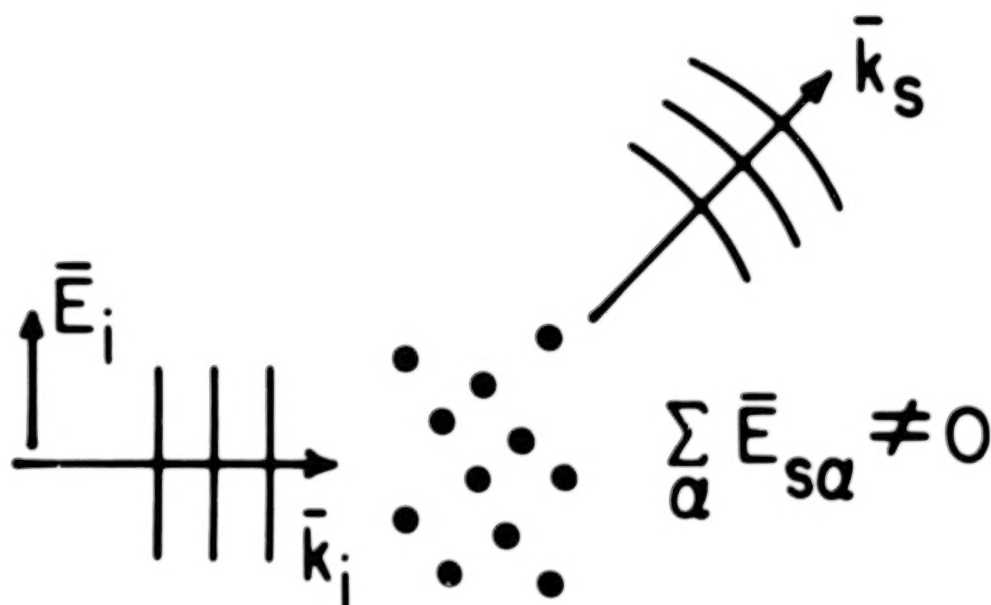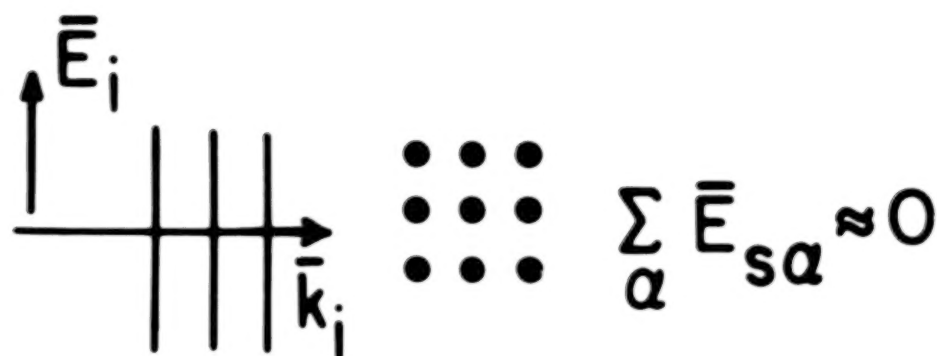
Fig. 2   Sketch of the EM wave scattered by a uniform array of electrons (top, no
          scattering) and a random array of electrons (bottom) when the number
          of electrons $N_e \lambda^3$ in the scattering volume λ^3 is very large.

DETECTOR

VACUUM CHAMBER

L_2

HIGH POWER LASER

L_1

PLASMA

LASER BEAM DUMP

VIEWING DUMP
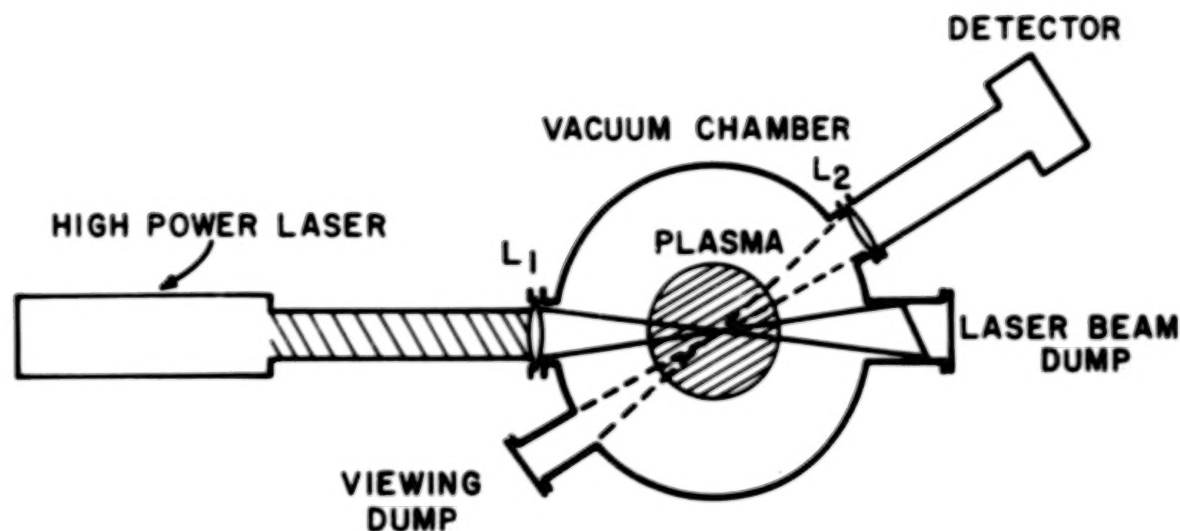
L_1 and L_2 FOCUSING LENSES LOCATED AT THE ENTRANCE AND EXIT PORT

Fig. 3   Simplified sketch of the Thomson scattering experiment. The high power laser beam is focussed into the plasma by the lens L_1 and the beam that goes through the plasma is absorbed by the laser beam dump. The receiver optics L_2 looks at the scattered signal from the plasma and into a viewing dump to minimize stray radiation.
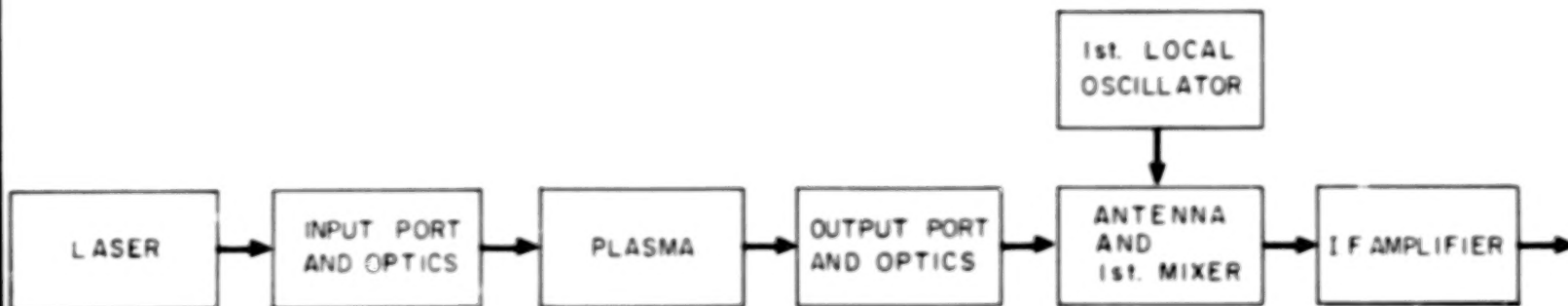
Fig. 4   Block diagram of some of the components necessary for the Thomson
scattering diagnostic.
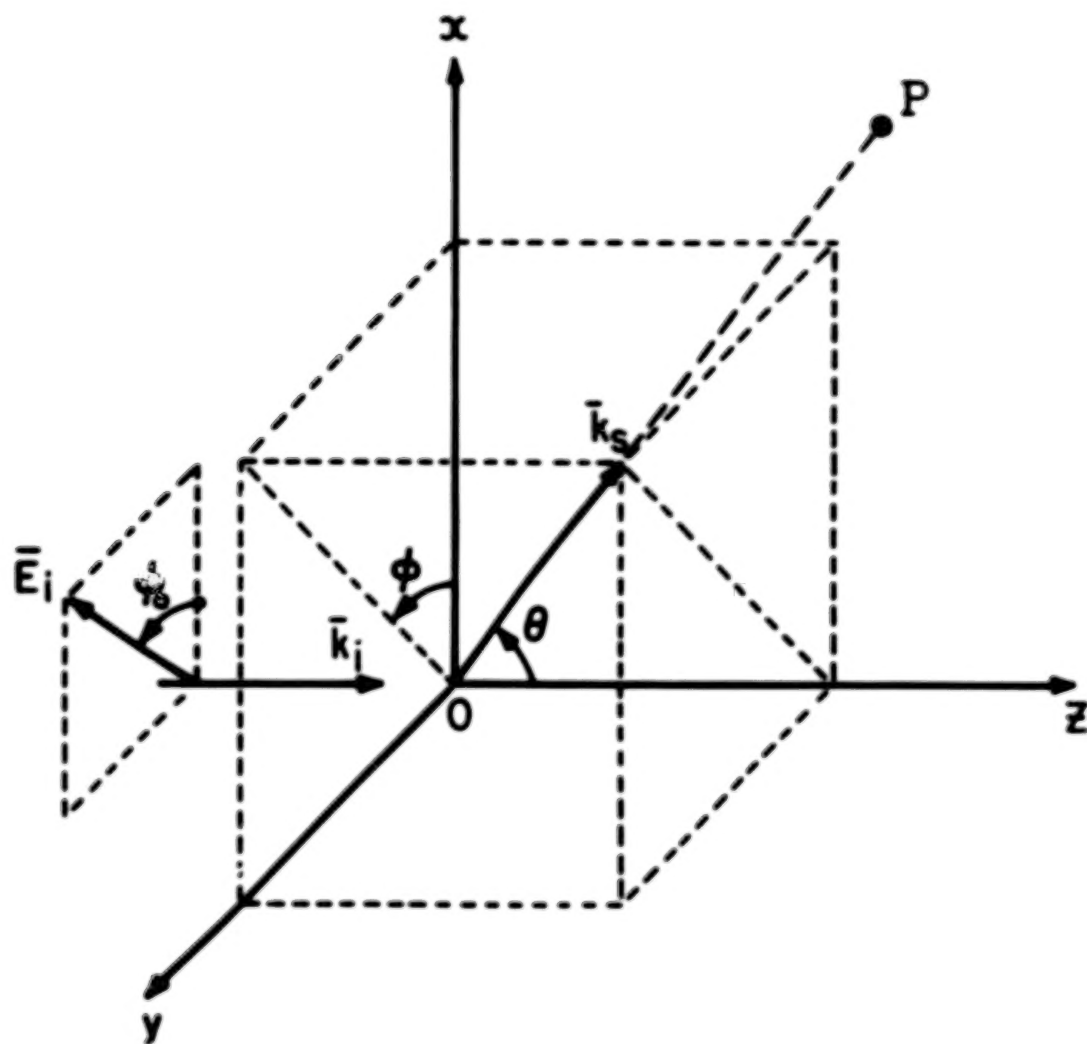
Fig. 5 Geometry of the linearly polarized high power laser beam ($\bar{k}_i$, $\bar{E}_i$) and of scattered signal ($\bar{k}_s$) observed at P.

104
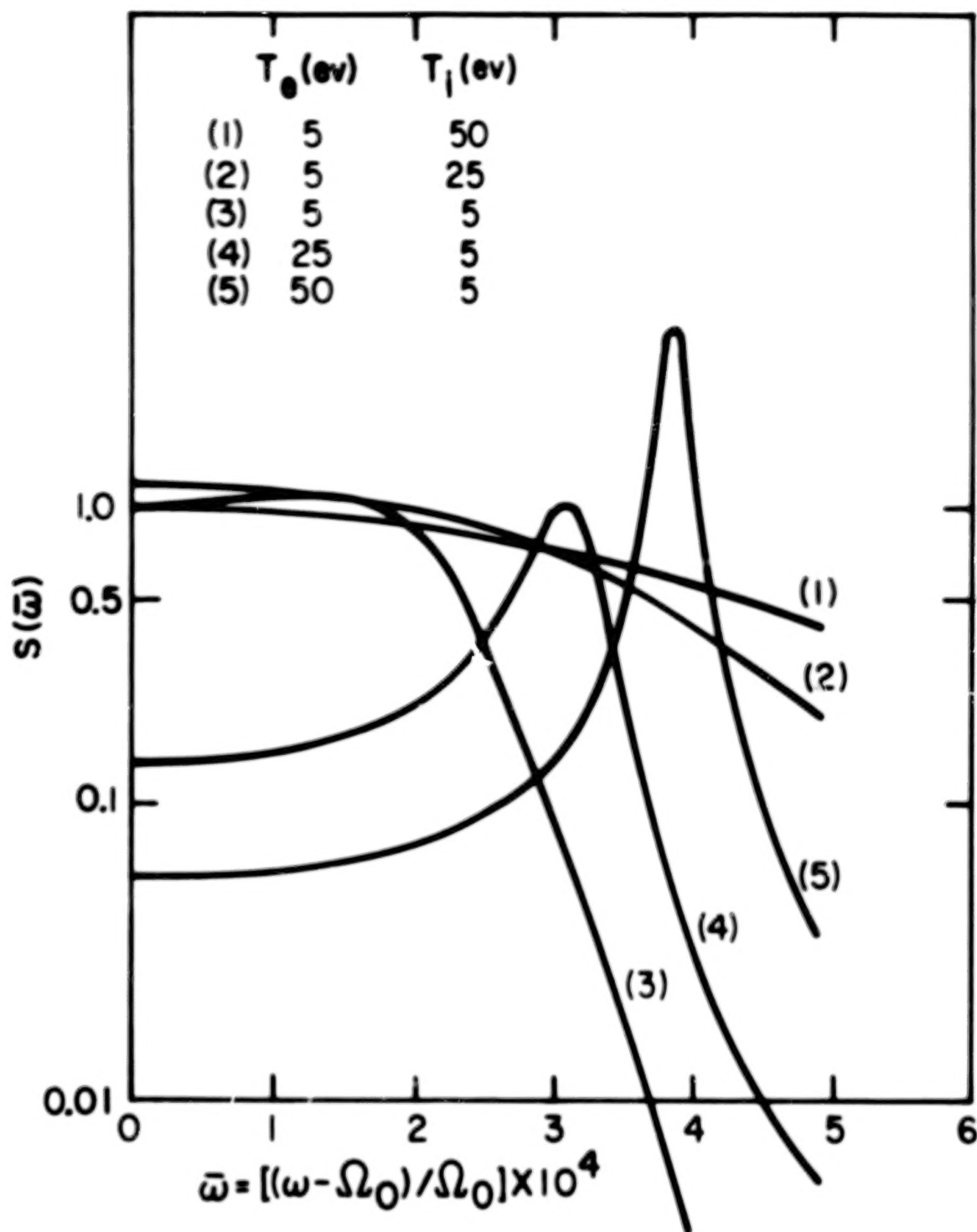
Fig. 6   Plot of the normalized scattering spectral density vs. the fractional
angular frequency deviation. The shape of the curves depends on the
ratio T_e/T_i. Taken from M.N. Rosenbluth and N. Rostoker, Physics
of Fluids 5, 776 (1962), Fig. 2.
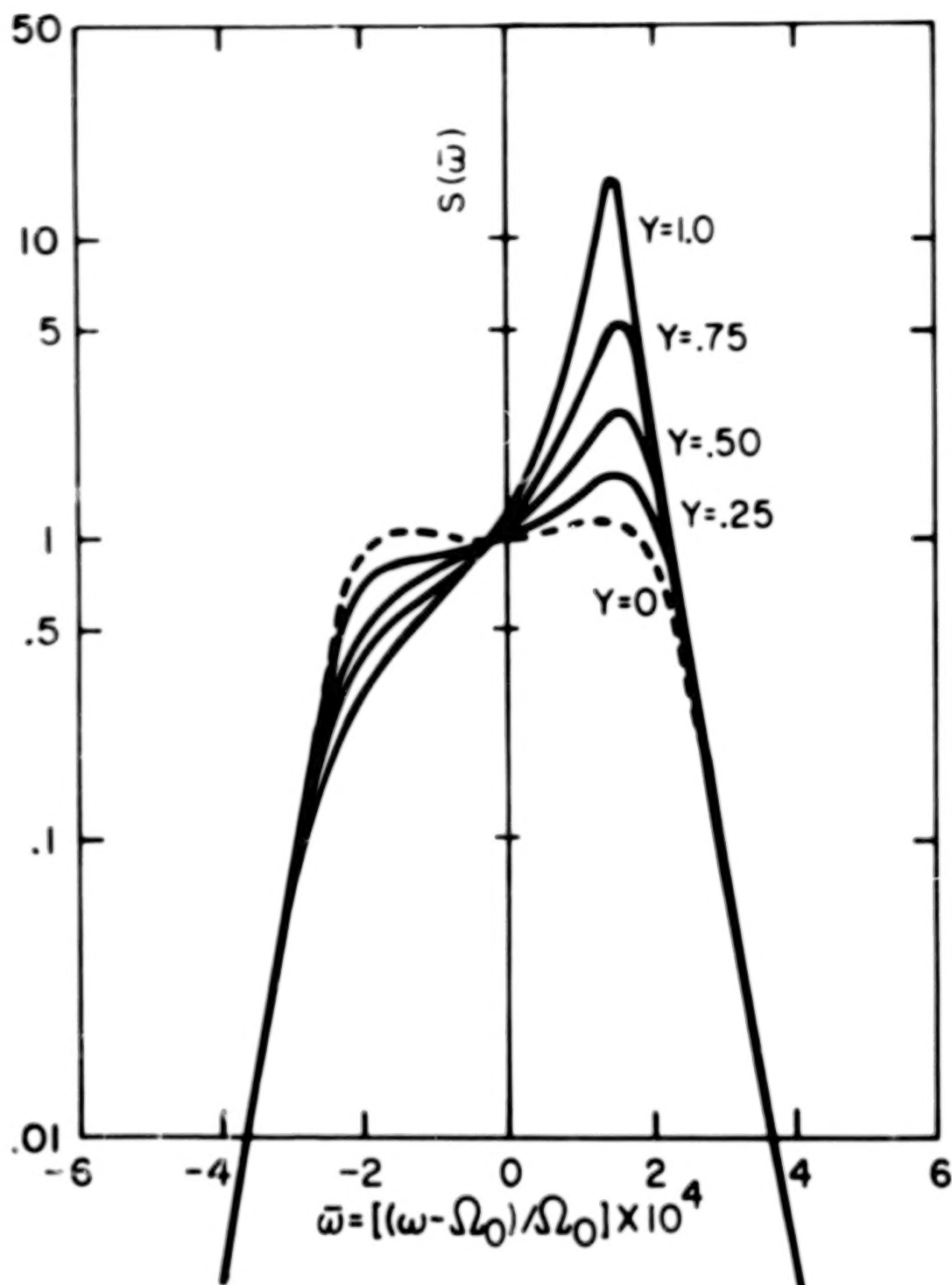
Fig. 7   Plot of the normalized scattering spectral density vs. the fractional angular
frequency deviation. The various curves are calculated for $T_e/T_i = 1$
and for a plasma with an electron drift velocity u measured as the fraction
$Y = u/v_e$ of the electron thermal velocity $v_e = (kT_e/m_e)^{1/2}$. Taken
from M.N. Rosenbluth and N. Rostoker, Physics of Fluids 5, 776 (1962),
Fig. 3.
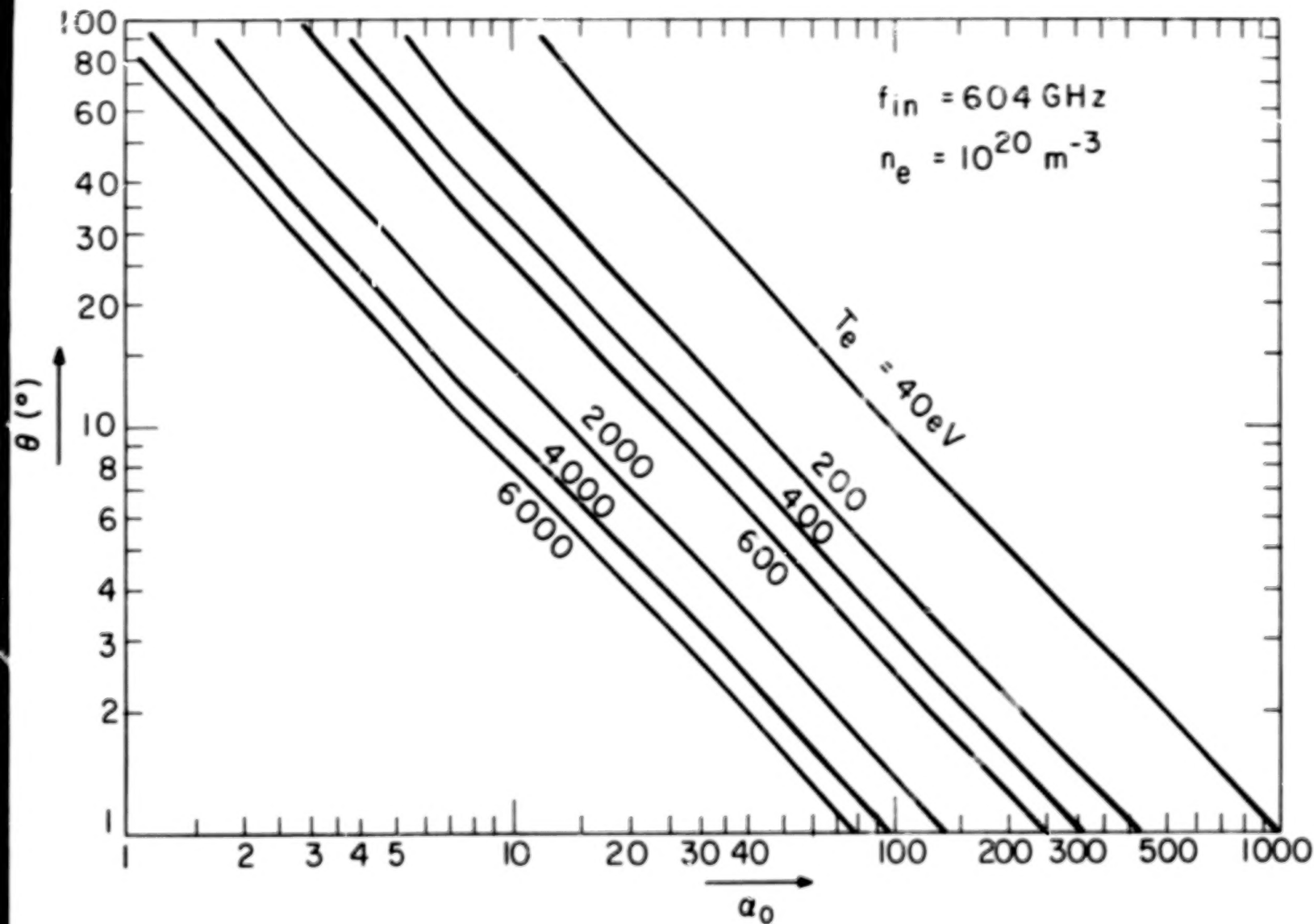
Fig. 8   Plot of $\alpha_o = \lambda_i / 4 \pi L_D \sin\frac{\theta}{2}$ vs. scattering angle θ for various electron temperature T_e. The H^+ plasma has the same parameters as those indicated under Table II caption.
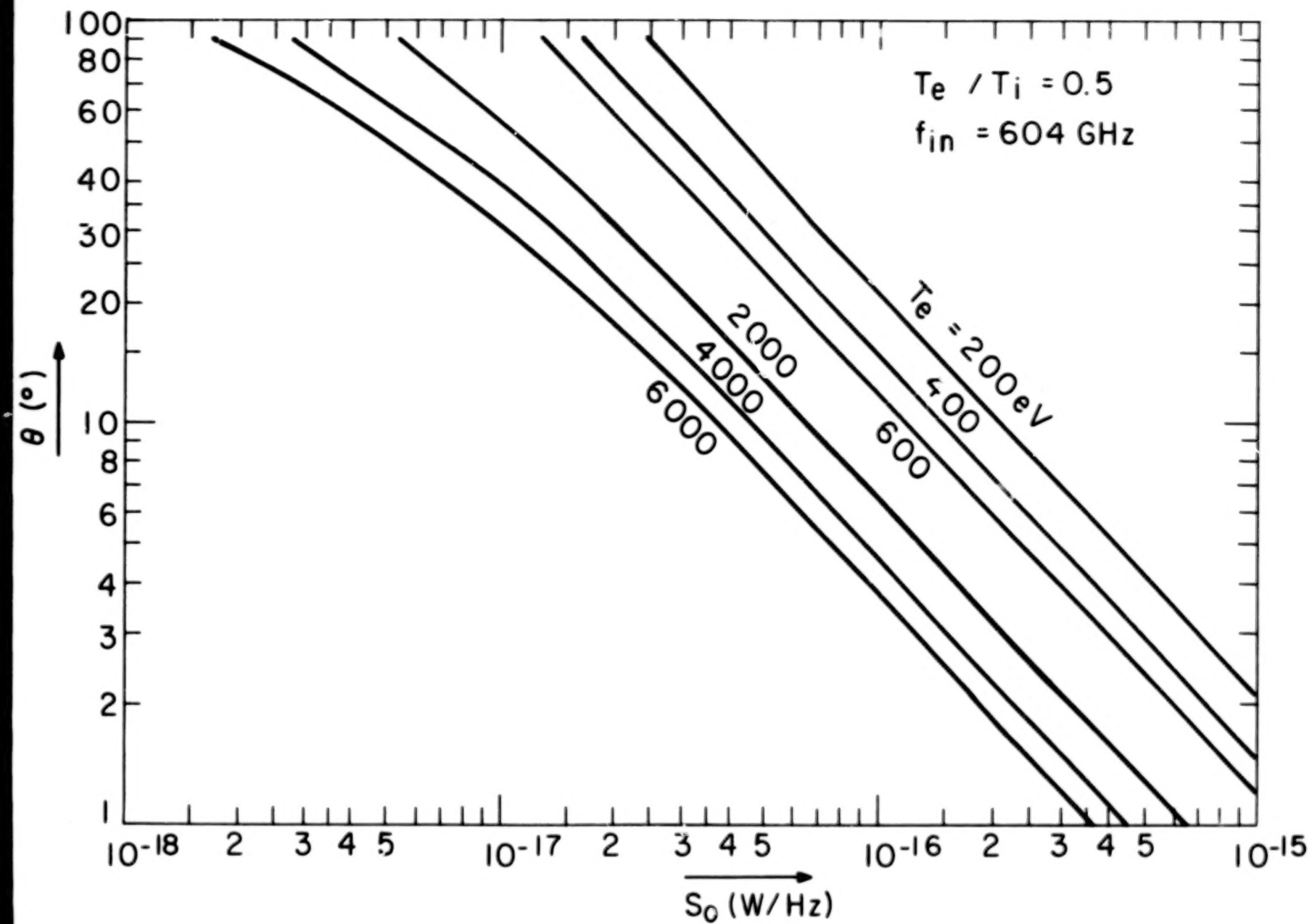
Fig. 9   Plot of the scattered spectral density at the origin S_o (W/Hz) vs. scattering angle θ for $T_e/T_i = 0.5$ for various T_e.
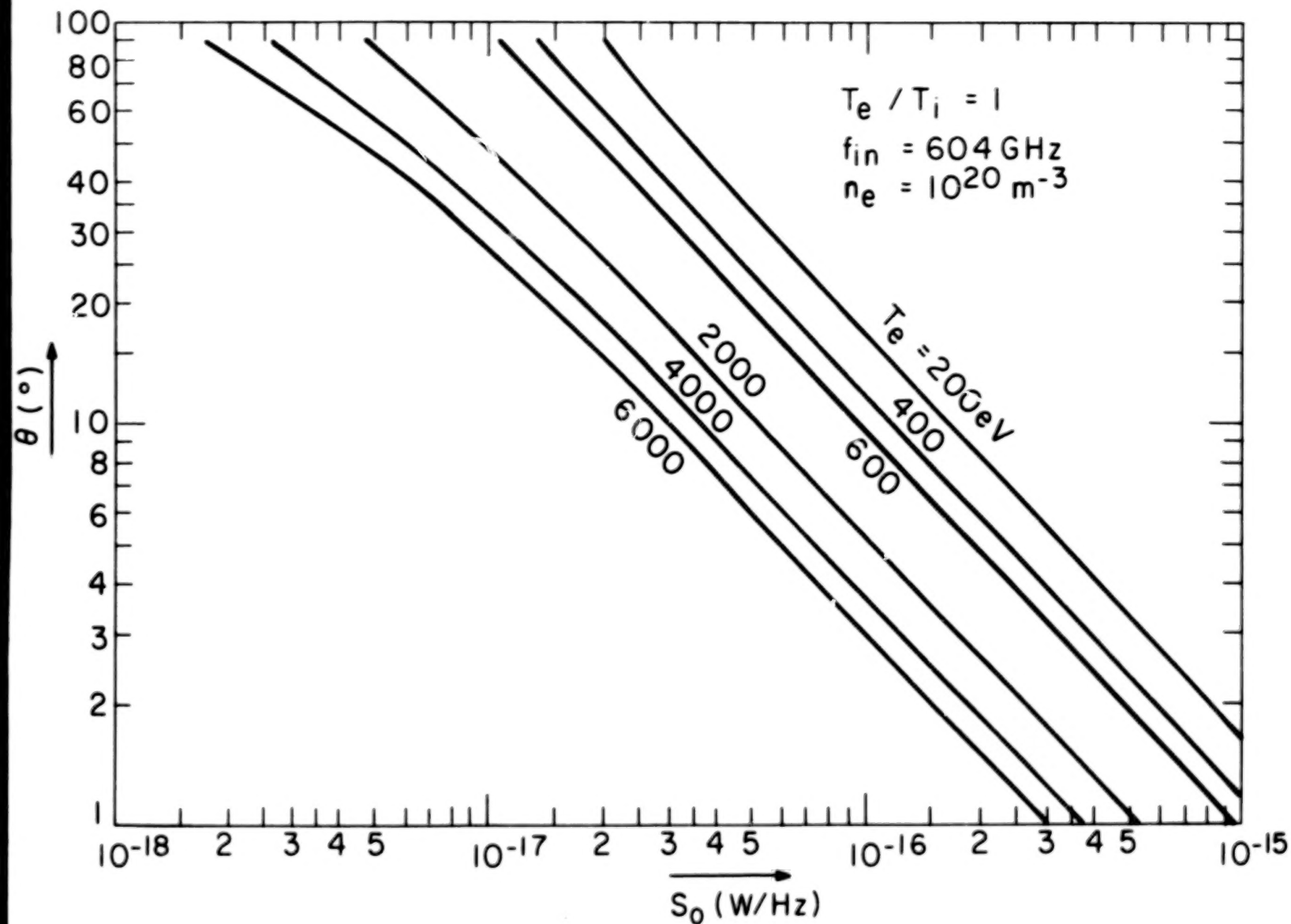
Fig. 10 Plot of S_o vs. θ for $T_e/T_i = 1$.
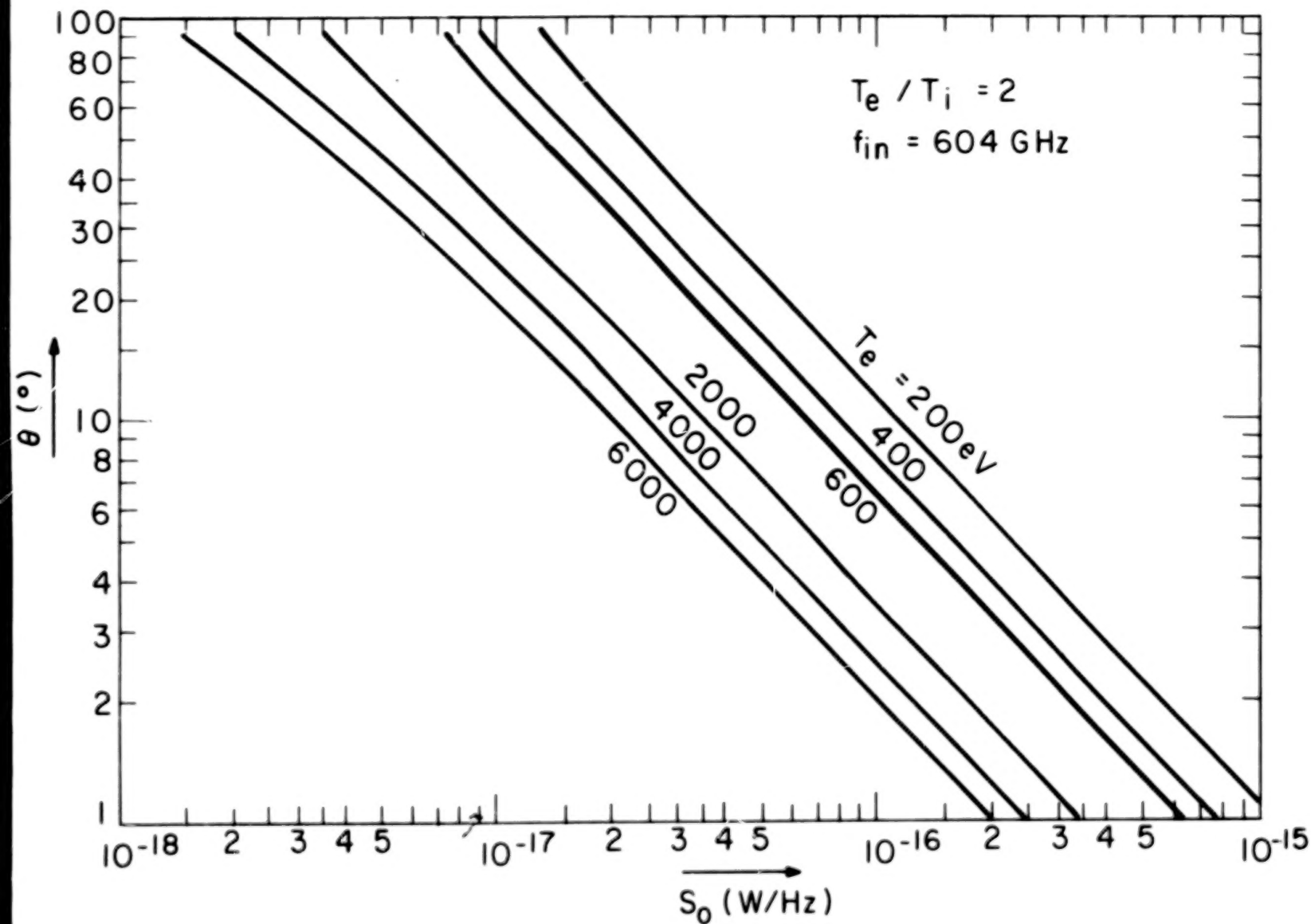
Fig. 11   Plot of S_o vs. θ for $T_e/T_i = 2$.
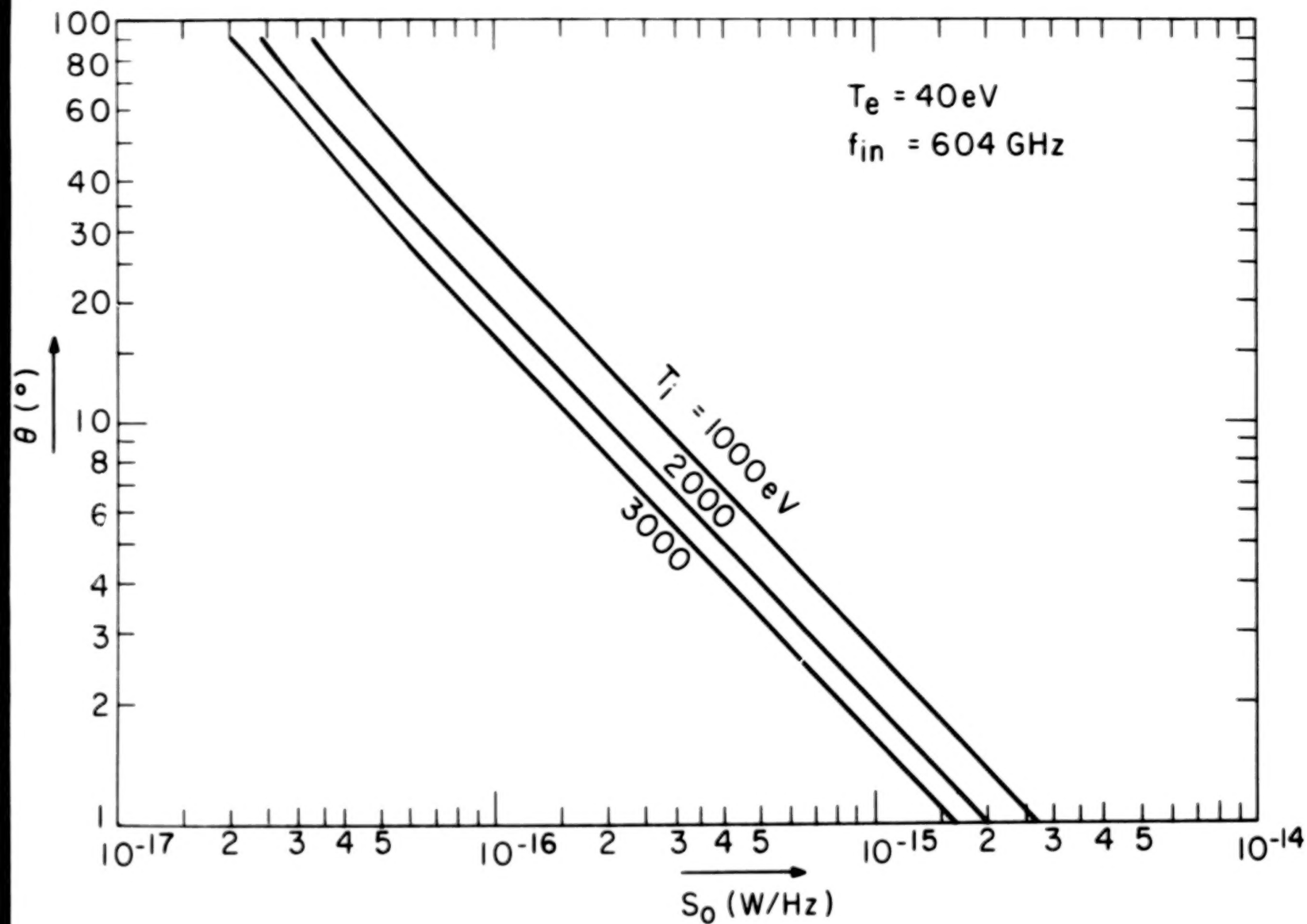
Fig. 12 Plot of S_o vs. θ for $T_e/T_i \ll 1$.

111
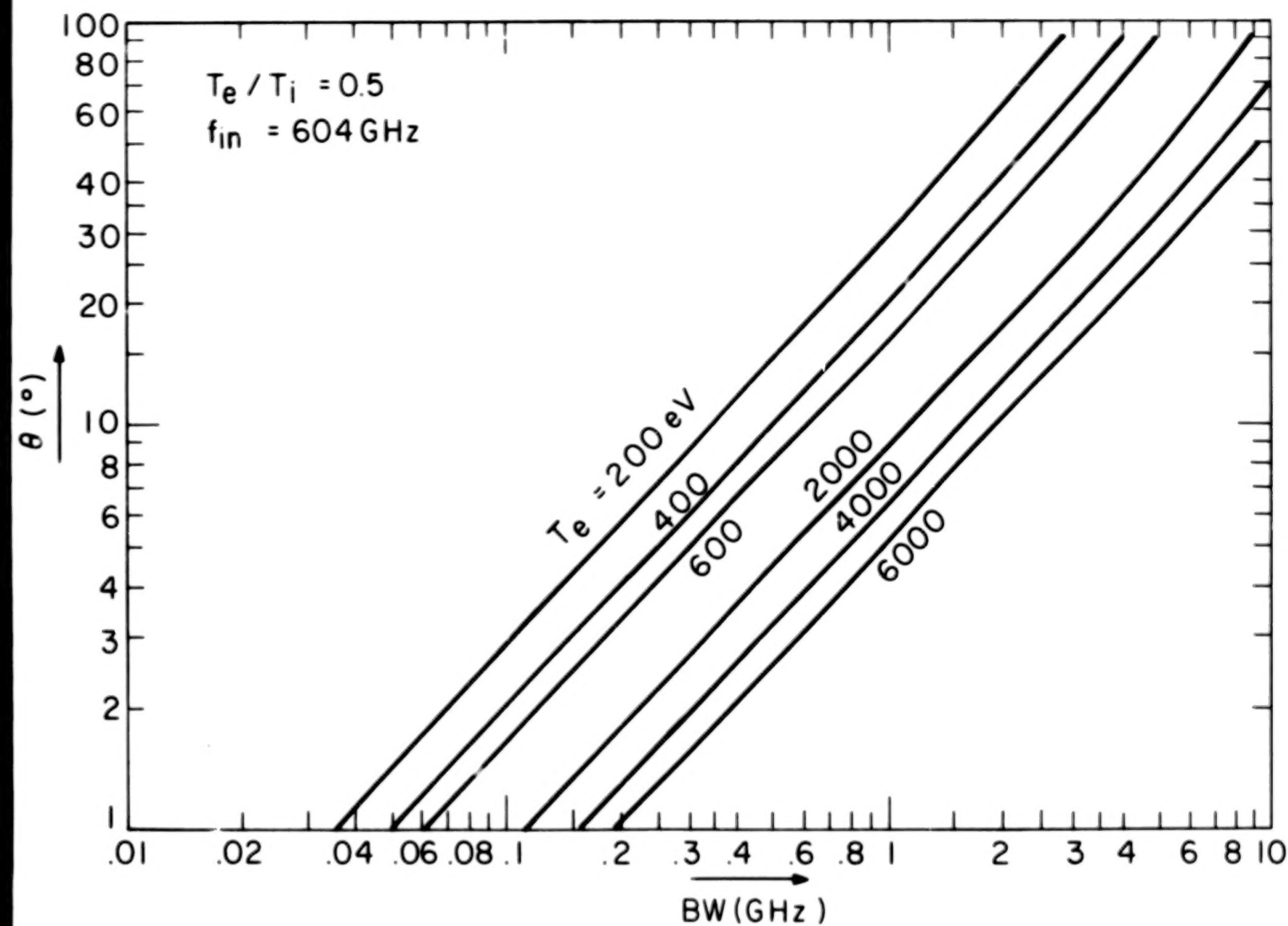
Fig. 13   Plot of the 10 db full bandwidth BW (GHz) vs. θ for $T_e/T_i = 0.5$.

11⊋

Fig. 14   Plot of BW vs. θ for $T_e/T_i = 1$.

113

Fig. 15   Plot of BW vs. θ for $T_e/T_i = 2$.

114

Fig. 16   Plot of BW vs. θ for $T_e/T_i \ll 1$.

115
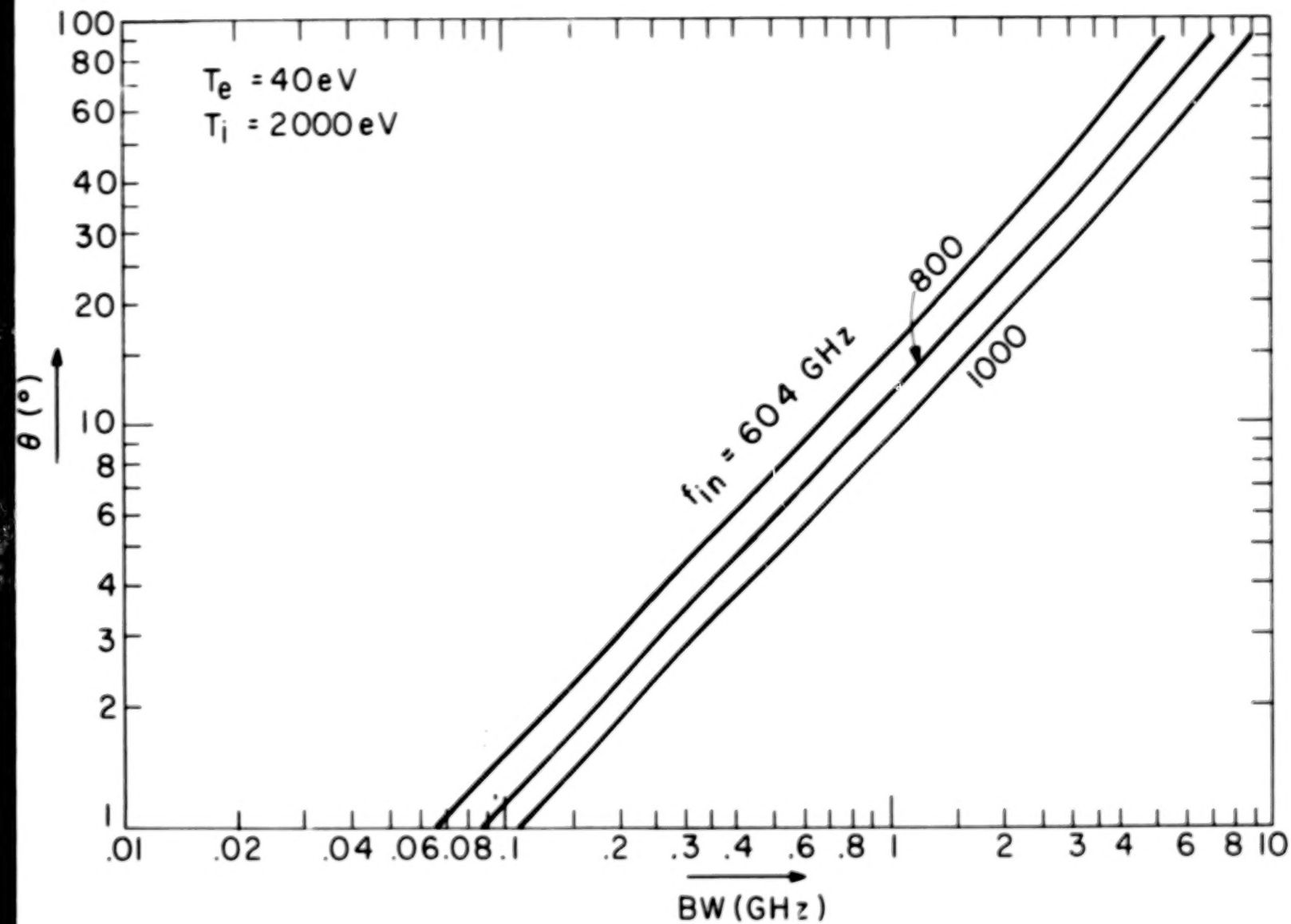
Fig. 17a   Plot of BW vs. θ for $T_e/T_i \ll 1$ and for f_{in} = 604 GHz, 800 GHz and 1000 GHz.

116
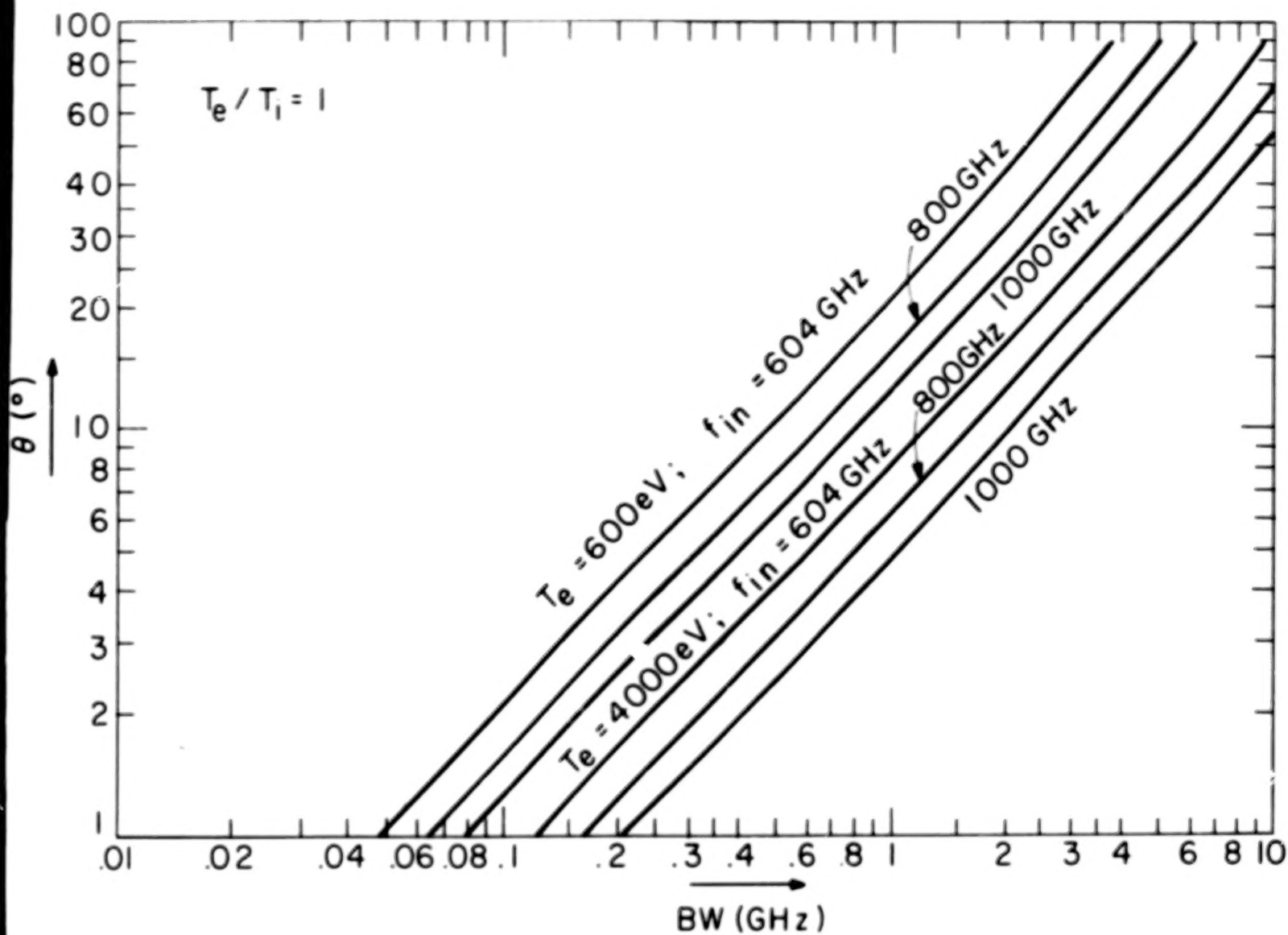
Fig. 17b Plot of BW vs. θ for $T_e/T_i = 1$ and for f_{in} = 604 GHz, 800 GHz and 1000 GHz.
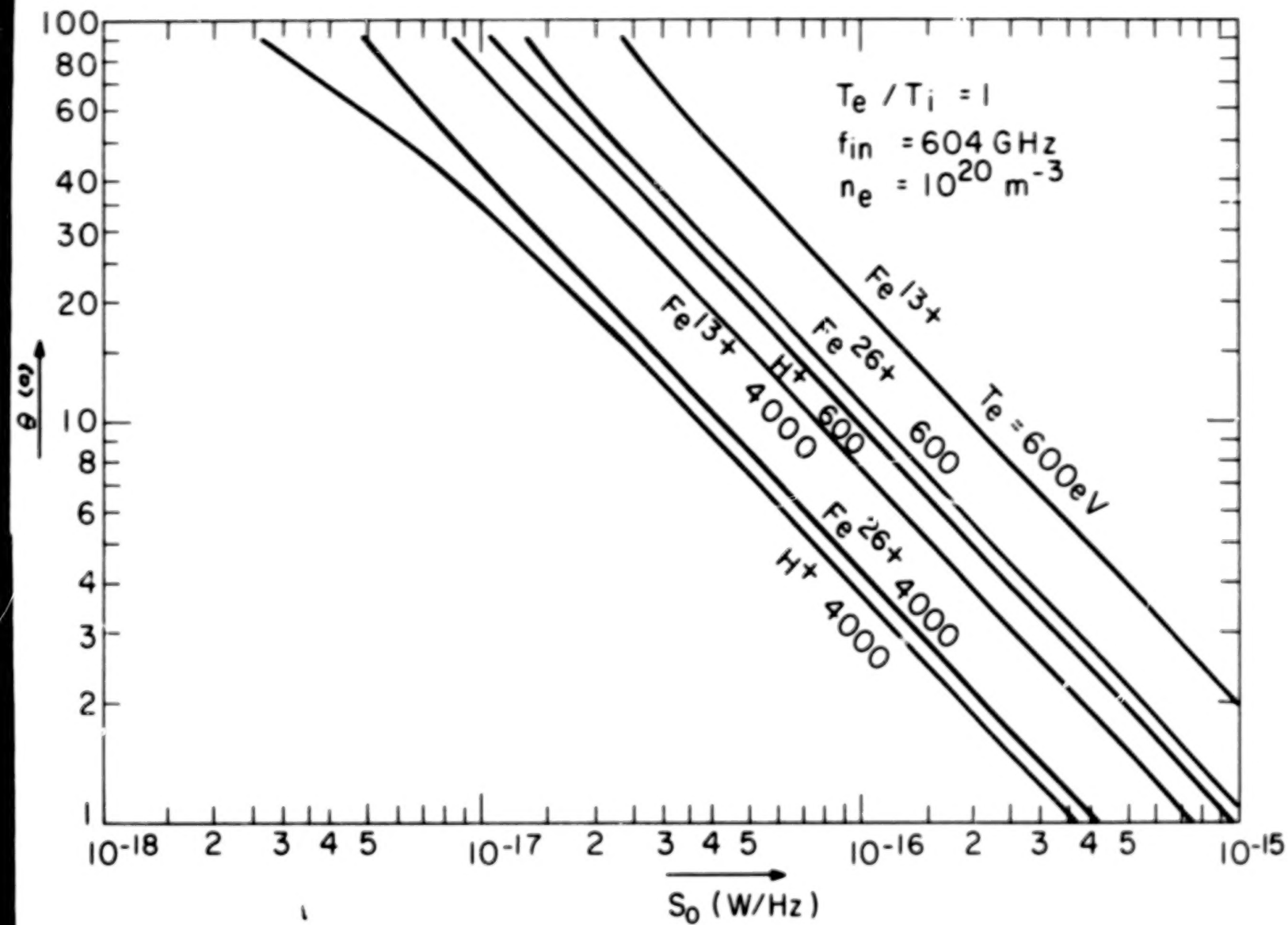
117

Fig. 18   Plot of S_0 vs. θ for $T_e/T_i = 1$ for H^+, Fe^{13+} and Fe^{26+} plasmas.

118

Fig. 19   Plot of BW vs. θ for $T_e/T_i = 1$ for H^+, Fe^{13+} and Fe^{26+} plasmas.

119
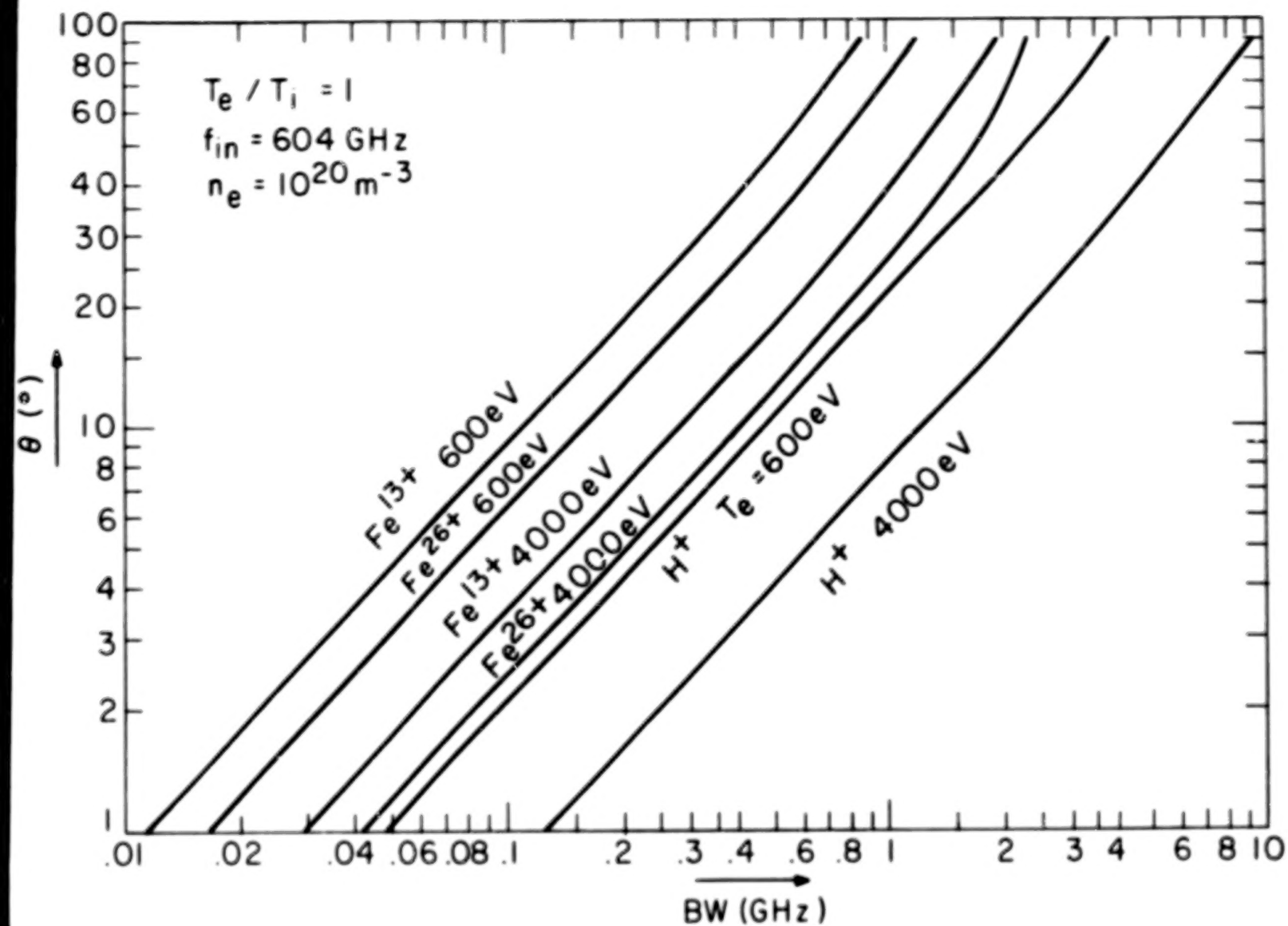
Fig. 20   Plot of S_0 vs. θ for $T_e/T_i << 1$ for H^+, Fe^+, Fe^{13+} and Fe^{26+} plasmas.

Fig. 21 Plot of BW vs. θ for $T_e/T_i << 1$ for H^+, Fe^+, Fe^{13+} and Fe^{26+} plasmas.

121
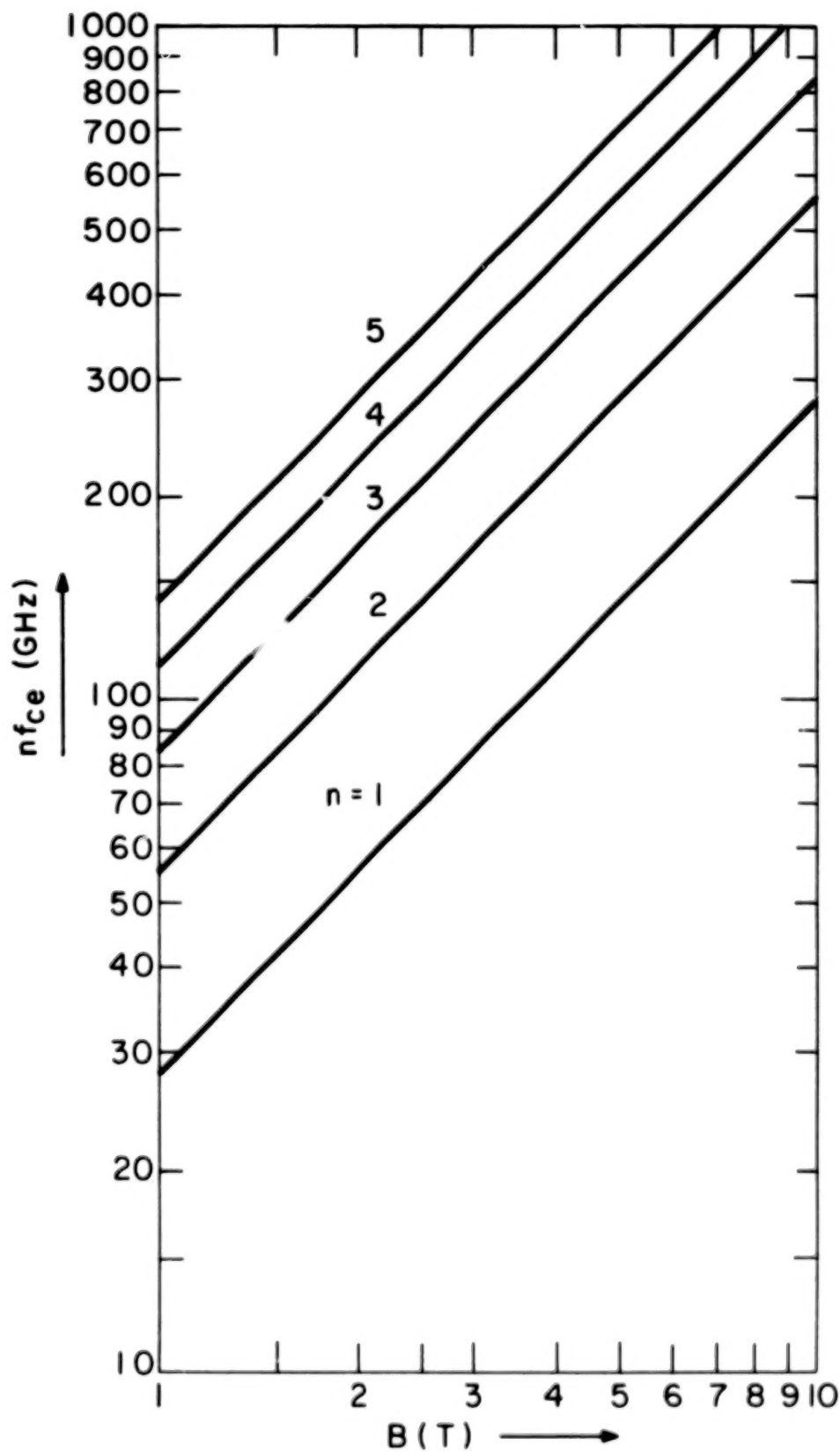
Fig. 22   Frequency of the harmonics of the electron cyclotron frequency vs. the
external magnetic field B. Both axes can be simultaneously scaled by
factors of ten.   122

BROADBAND
MIXER NOISE
Single Sideband
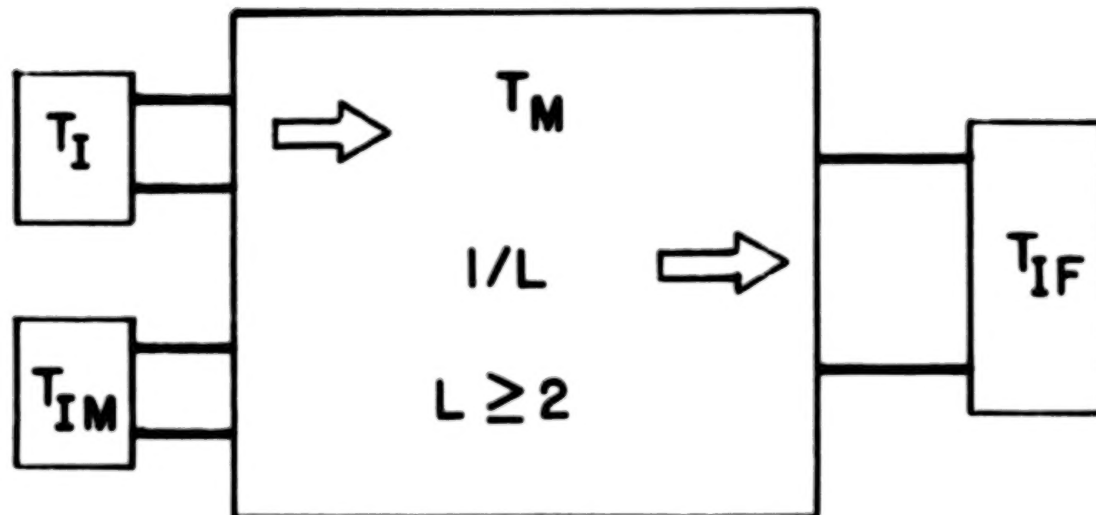
Fig. 23   Block diagram of a broadband mixer with an effective noise temperature T_M and conversion loss $L \geq 2$. The input channel and the image channel have both matched loads with noise temperatures T_I and T_{IM} respectively. The output channel is matched to an IF amplifier with an effective noise temperature T_{IF}. The effective input channel noise temperature T_{Ieff} (single sideband) is given by $T_{Ieff} = T_I + T_{IM} + (L - 2) T_M + L T_{IF}$.

123
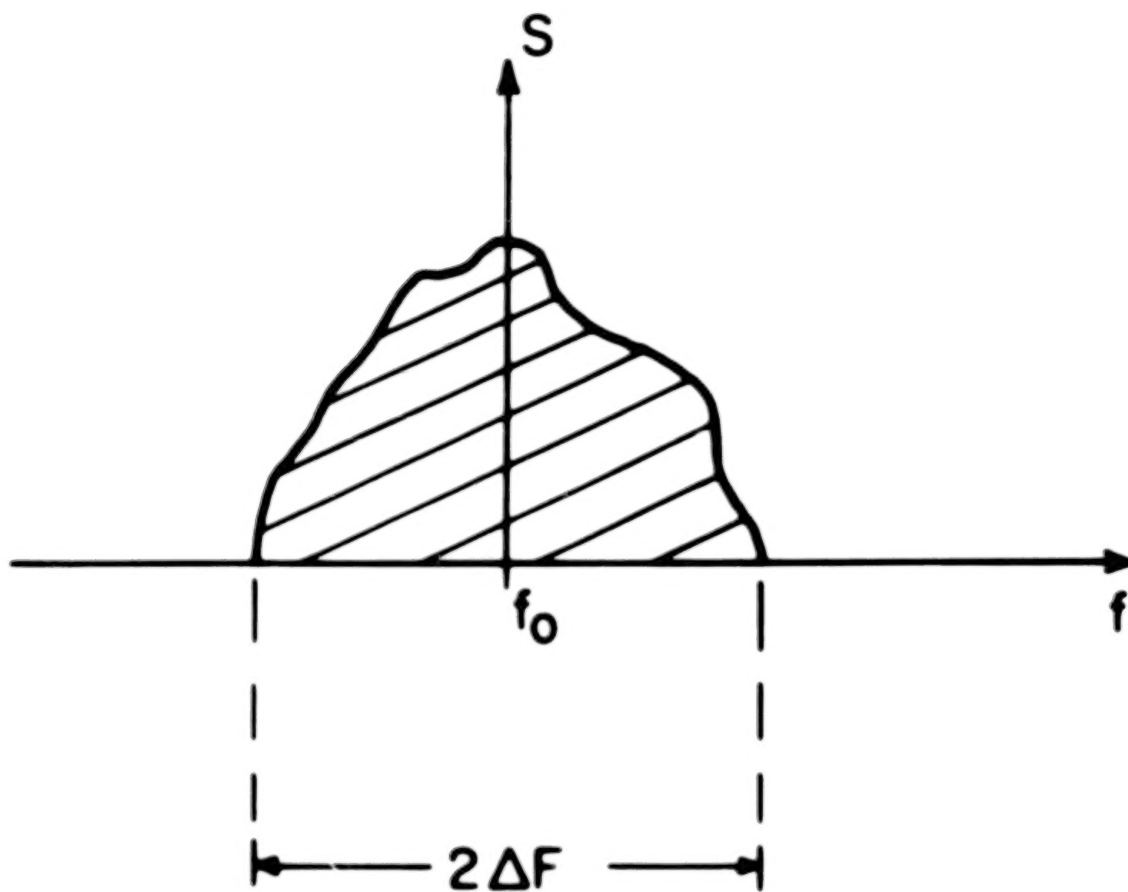
$$G(t) = g_1(t) \cos(\omega_0 t)$$
$$+ g_2(t) \sin(\omega_0 t)$$

Fig. 24   Sketch of the power spectral density of a band limited signal. The power
density must be zero beyond the $2 \Delta F$ bandwidth.

124

SAMPLING THEOREM

$$\leftarrow 1/2\Delta F \rightarrow$$

$$\text{PERIOD} \geq 1/\Delta F$$
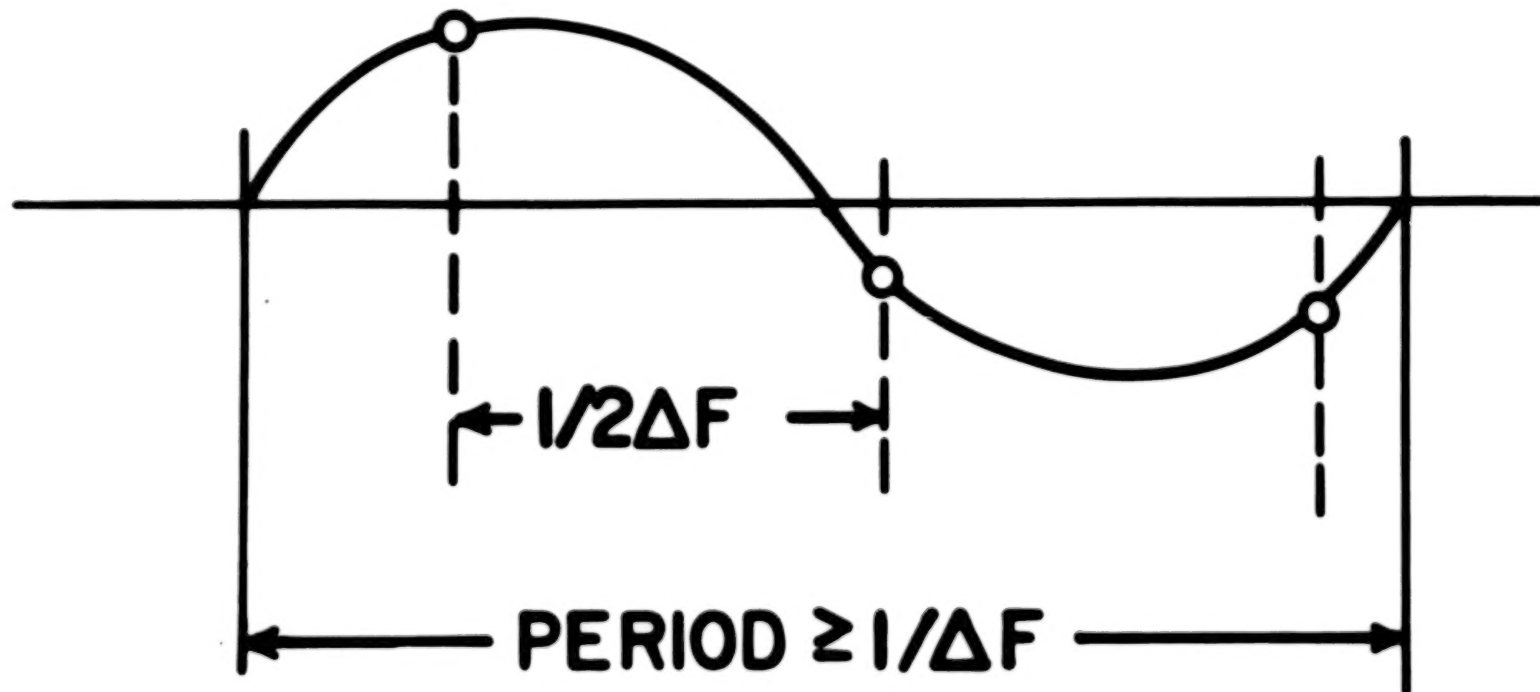
$$N = T\, 2\Delta F$$

Fig. 25   Sketch of the sampling theorem applied to a band limited signal.
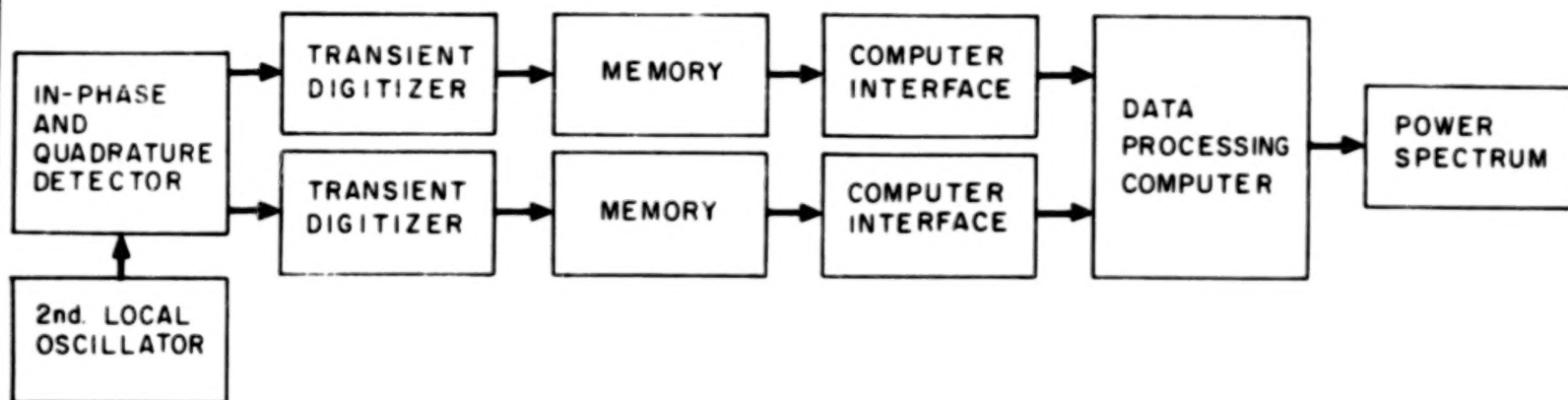
Fig. 26   Block diagram of the optimal signal processing scheme to determine the power spectral density of the Thomson scattered signal.
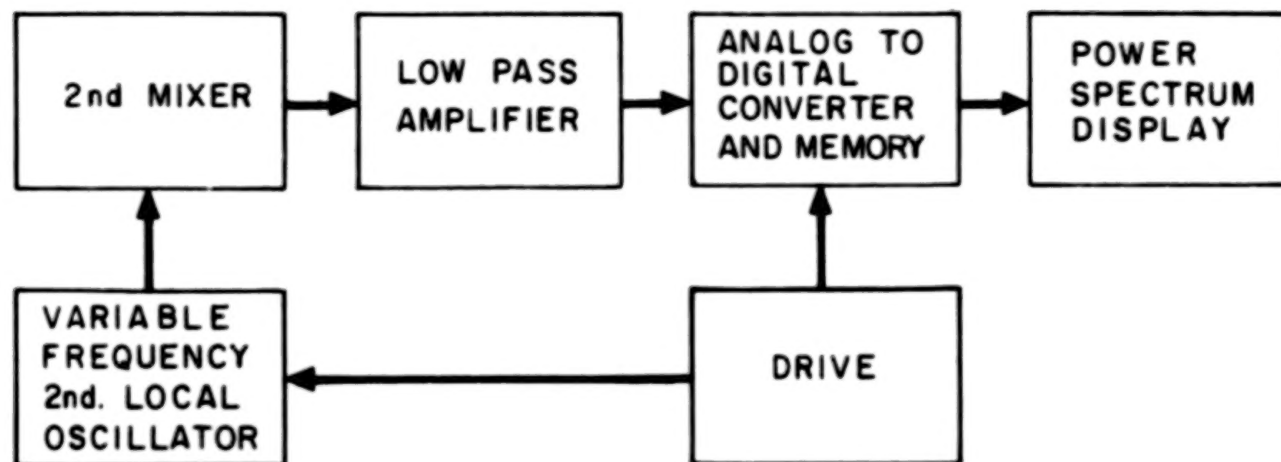
Fig. 27   Block diagram of a suboptimal signal processing scheme. It is similar to those used by commercial spectrum analyzers.
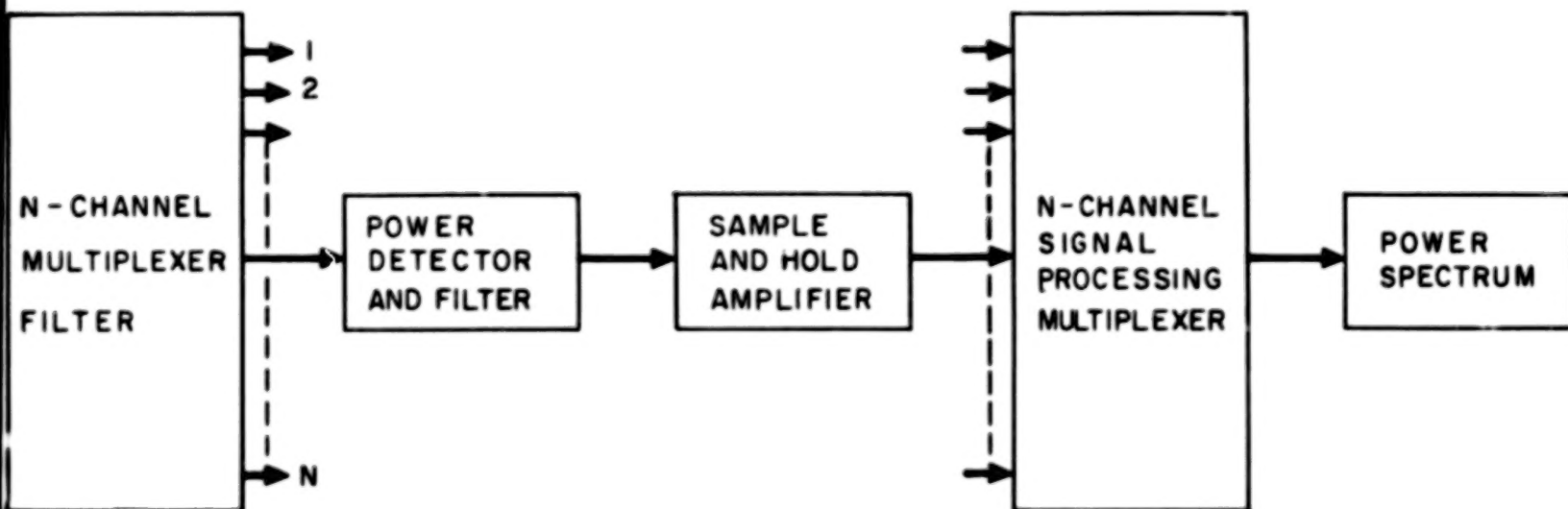
Fig. 28   Block diagram of a more efficient suboptimal processing scheme.

128
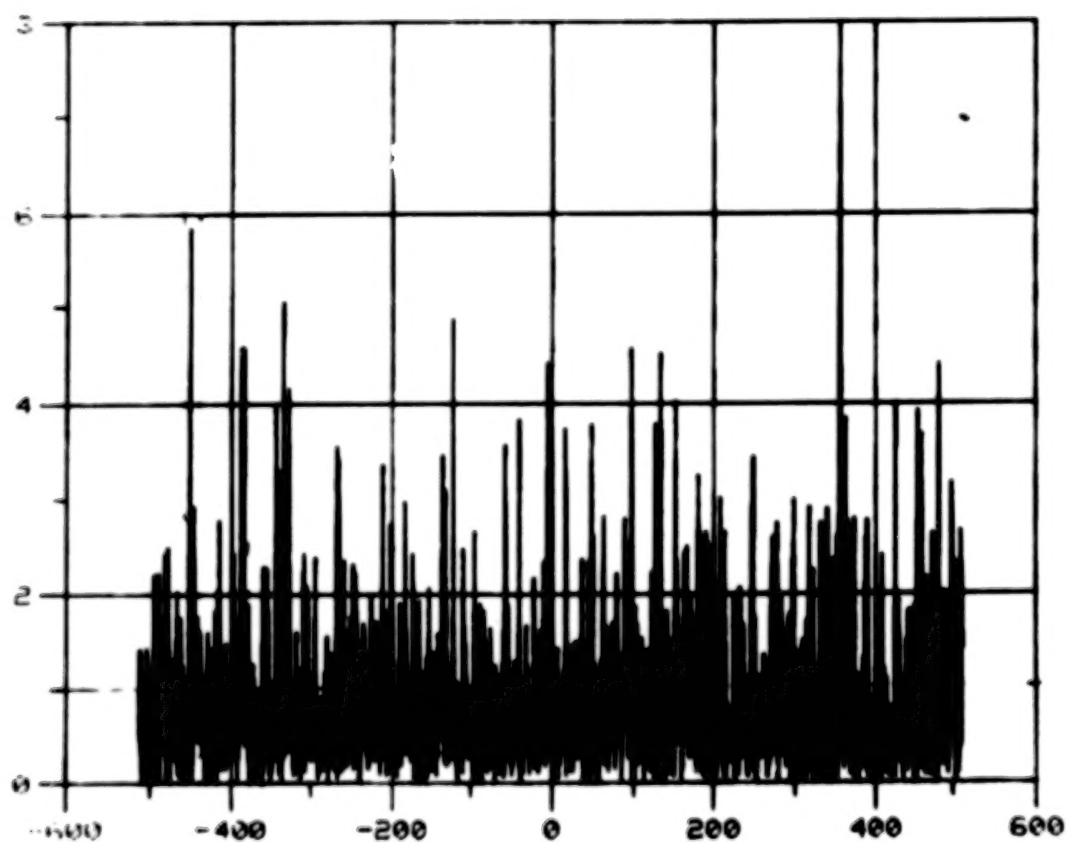
Fig. 29   Fast Fourier transform of a band limited white noise with a power density
of one (arbitrary units) vs. channel number (-512 to +512).

129
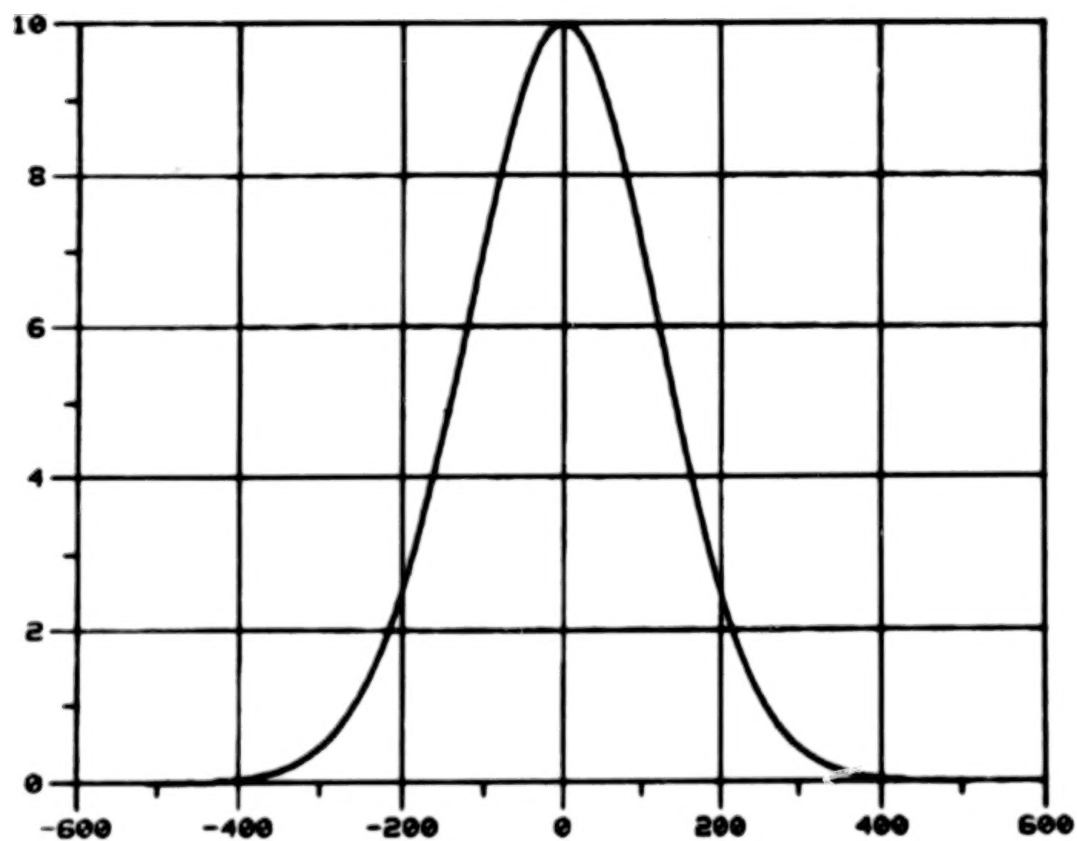
Fig. 30   Power spectral density of a band limited Gaussian noise with a peak power
density of 10 units.
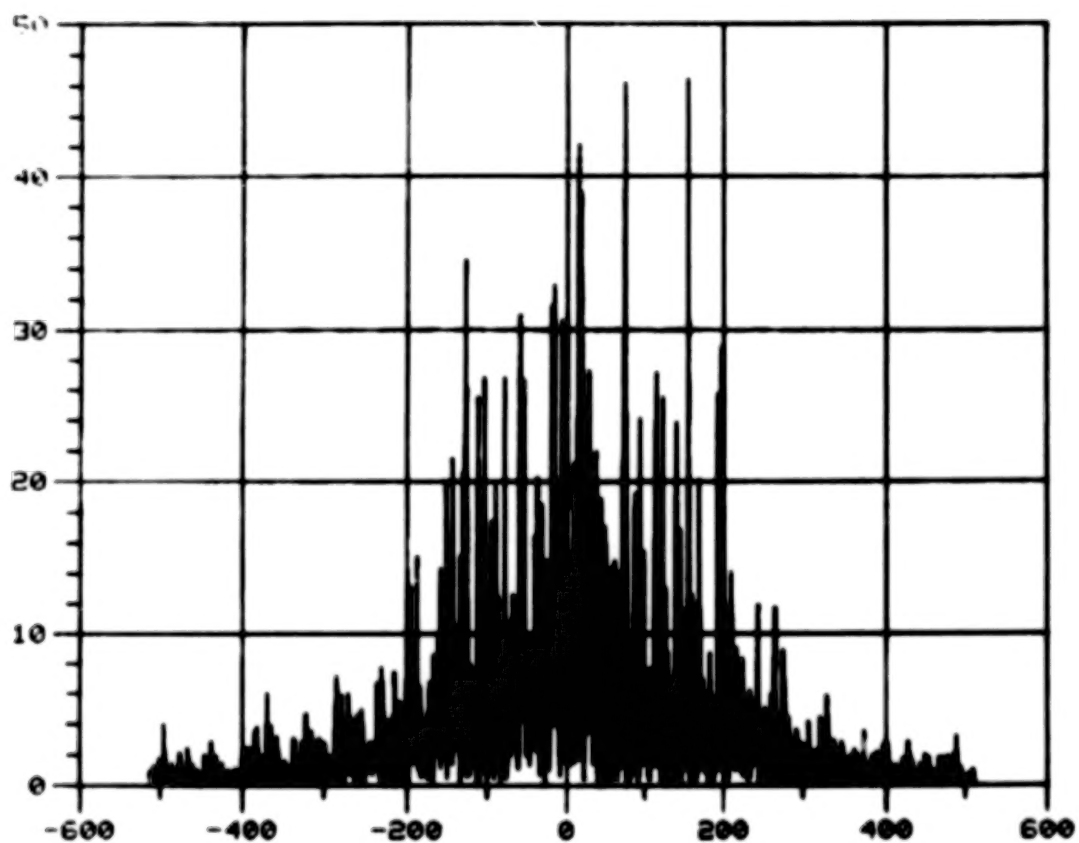
Fig. 31   Fast Fourier transform of the noise signal shown in Fig. 30.
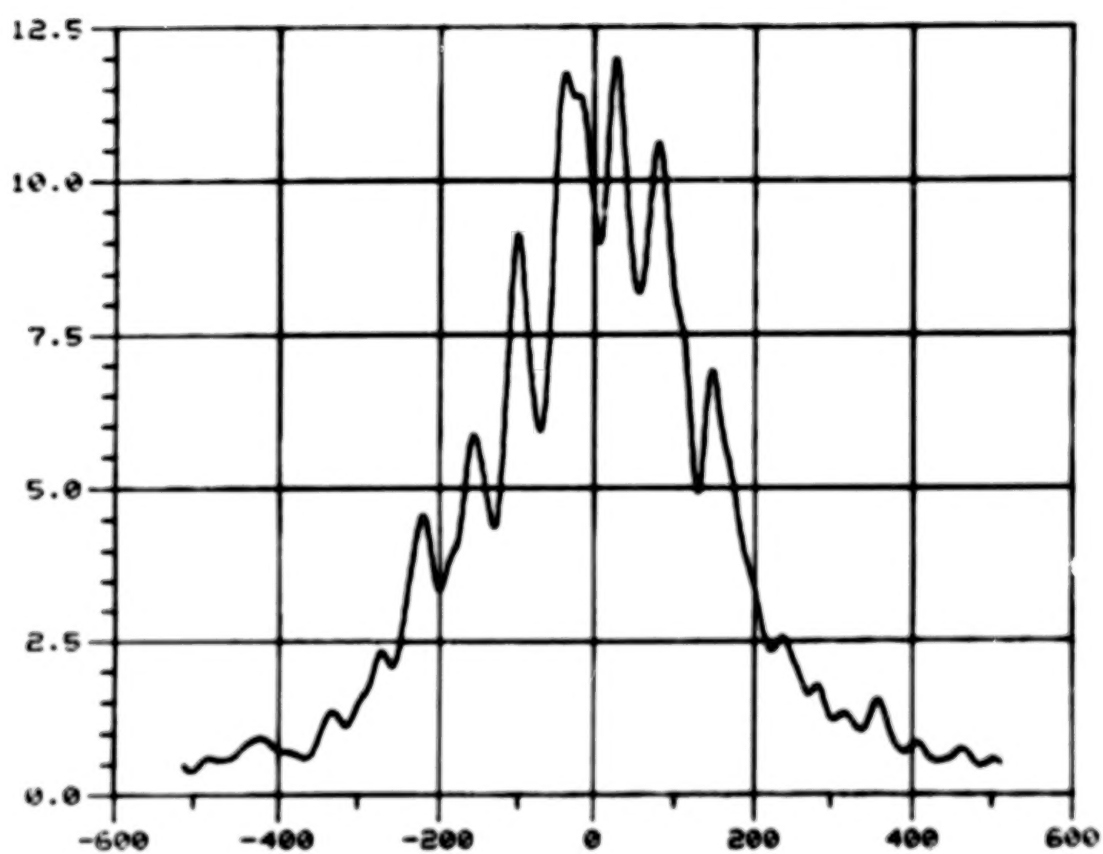
Fig. 32   Same as Fig. 31 but averaging over 64 consecutive channels.
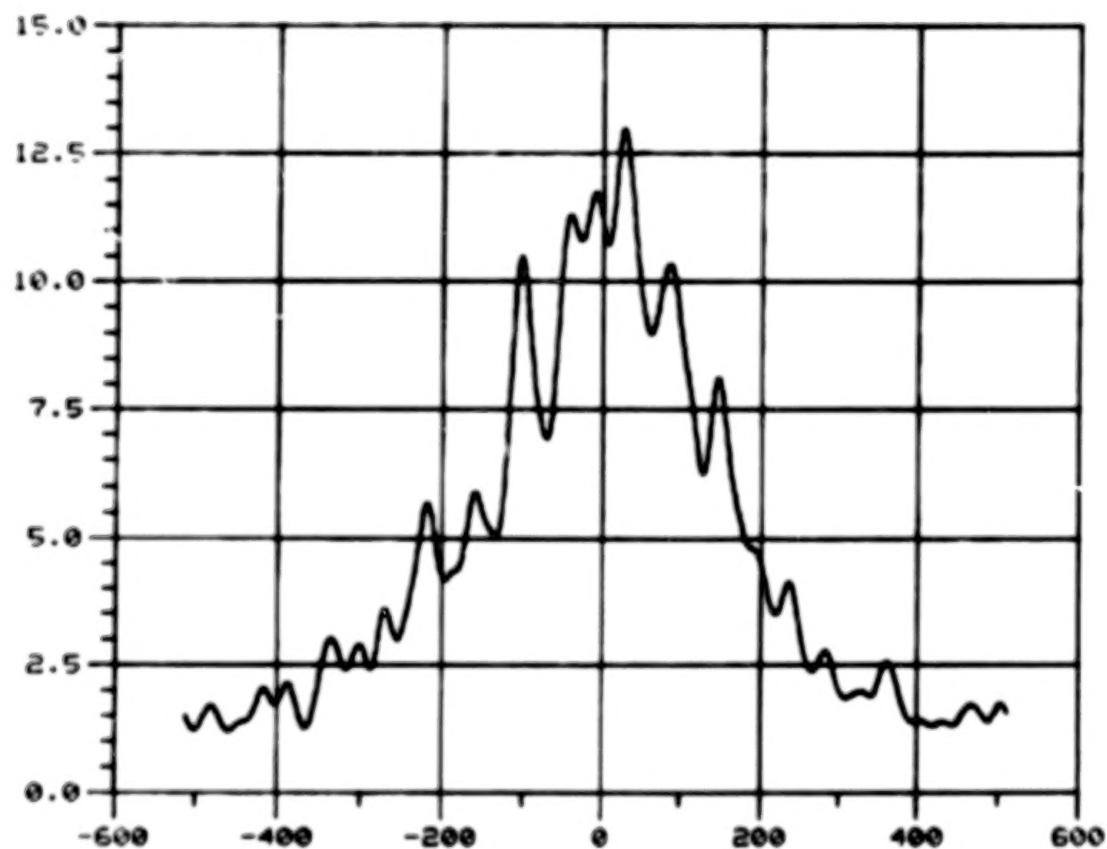
Fig. 33   Fast Fourier transform of the noise signal shown in Fig. 29 plus a noise source (simulating the scattered signal) with a power density like the one shown in Fig. 30.
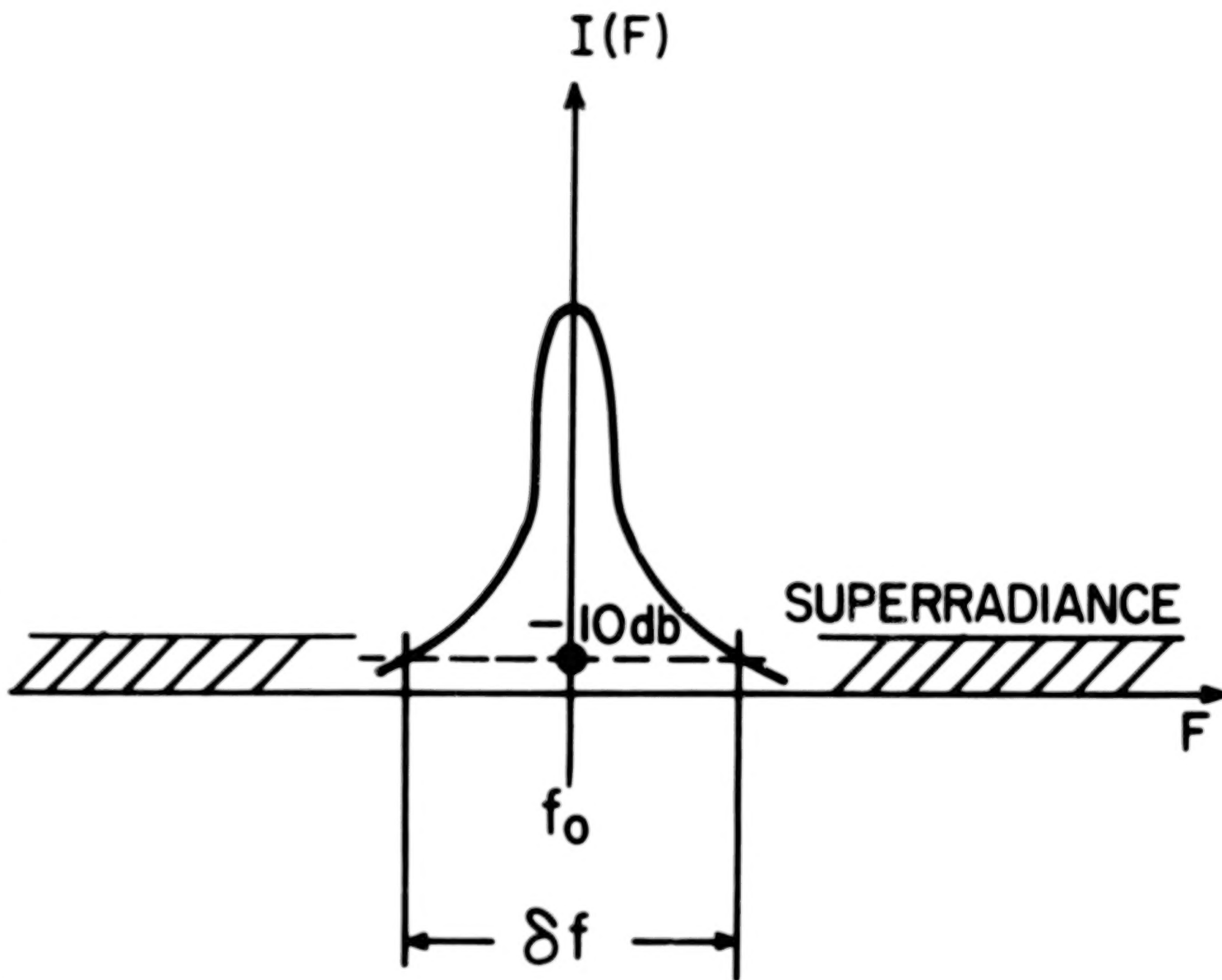
Fig. 34   Sketch of the spectral characteristics of the high power laser. The main
line is assumed to have a Gaussian lineshape superimposed in a constant,
band limited superradiance background.

134
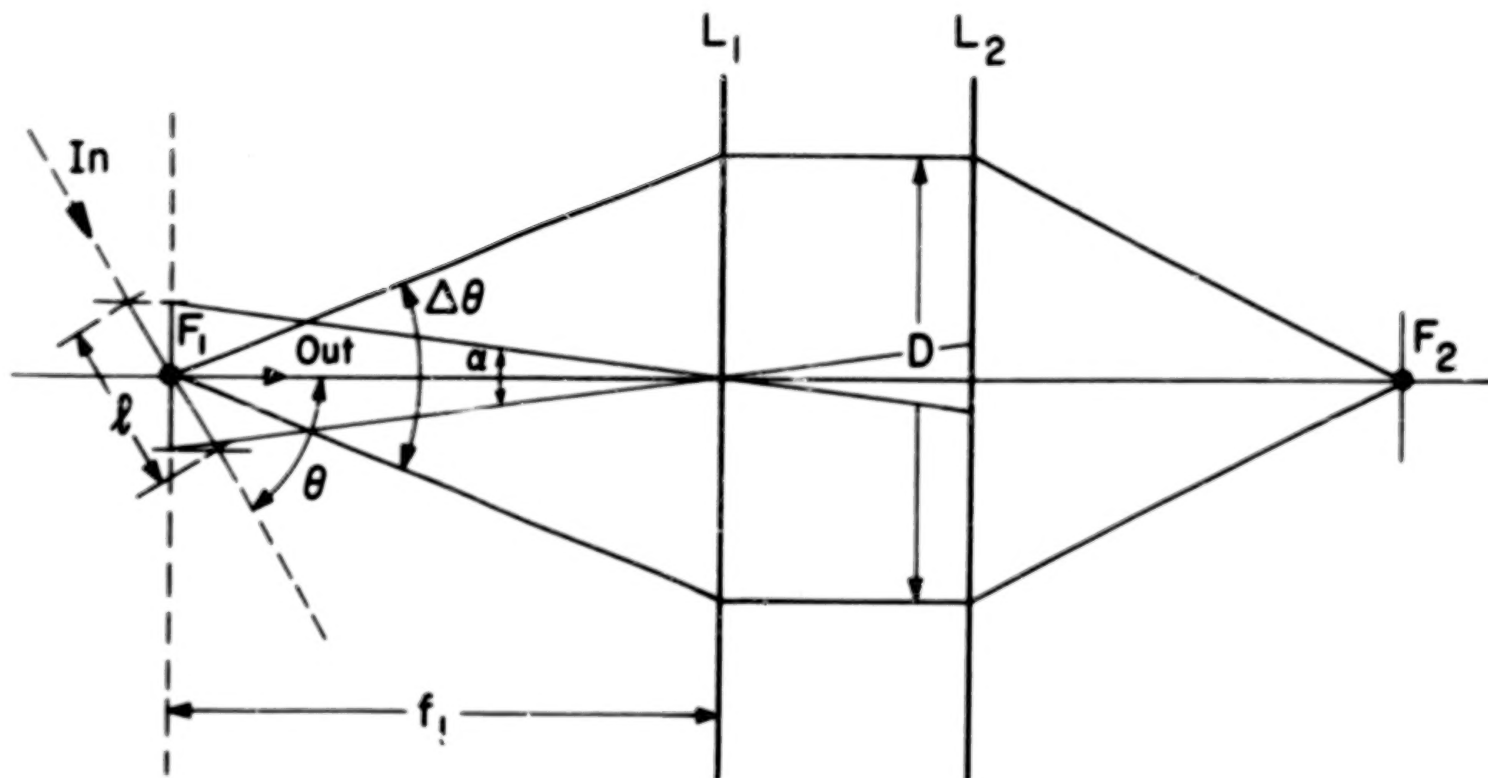
Fig. 35   Collection optics layout where L_1 and L_2 are lenses, θ is the scattering angle, $\Delta\theta$ is the angular resolution, F_1 is the focal point of L_1, f_1 is the focal length of L_1, ℓ is the scattering length, α defines the field of view of the antenna, and D is the aperture of the optics.

135
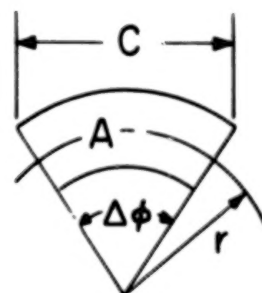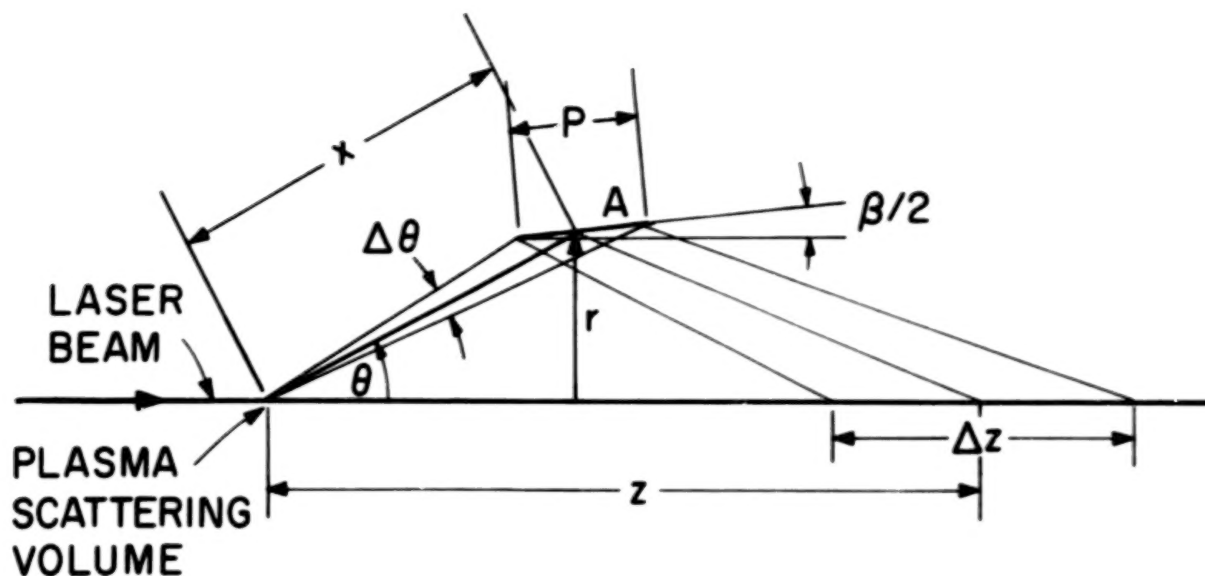
Fig. 36   Illustration defining the axicon parameters. A is the axicon, θ is the scattering angle, $\Delta\theta$ is the angular resolution, x is the distance from the plasma scattering volume to the center of the axicon, p is the slant length of the axicon, β is the apex angle of the cone of which the axicon is a segment, r is the radius of the axicon arc, z is the distance from the plasma scattering volume to the center of the image position, Δz is the length of the image, C is the longest chord in the axicon arc, and $\Delta\phi$ is the magnitude of the axicon arc.

136
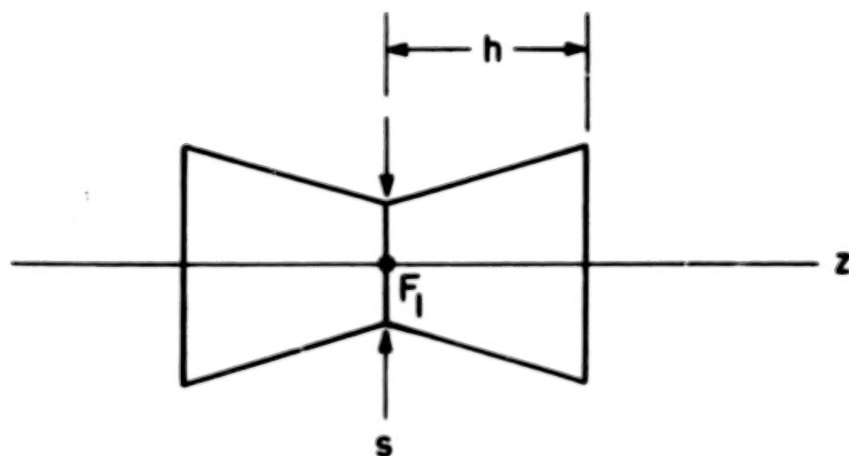
Fig. 37 The effective noise volume that the collection optics sees is equivalent to two truncated cones connected at the focal spot of lens L_1. h is the plasma radius and s is the focal spot diameter.
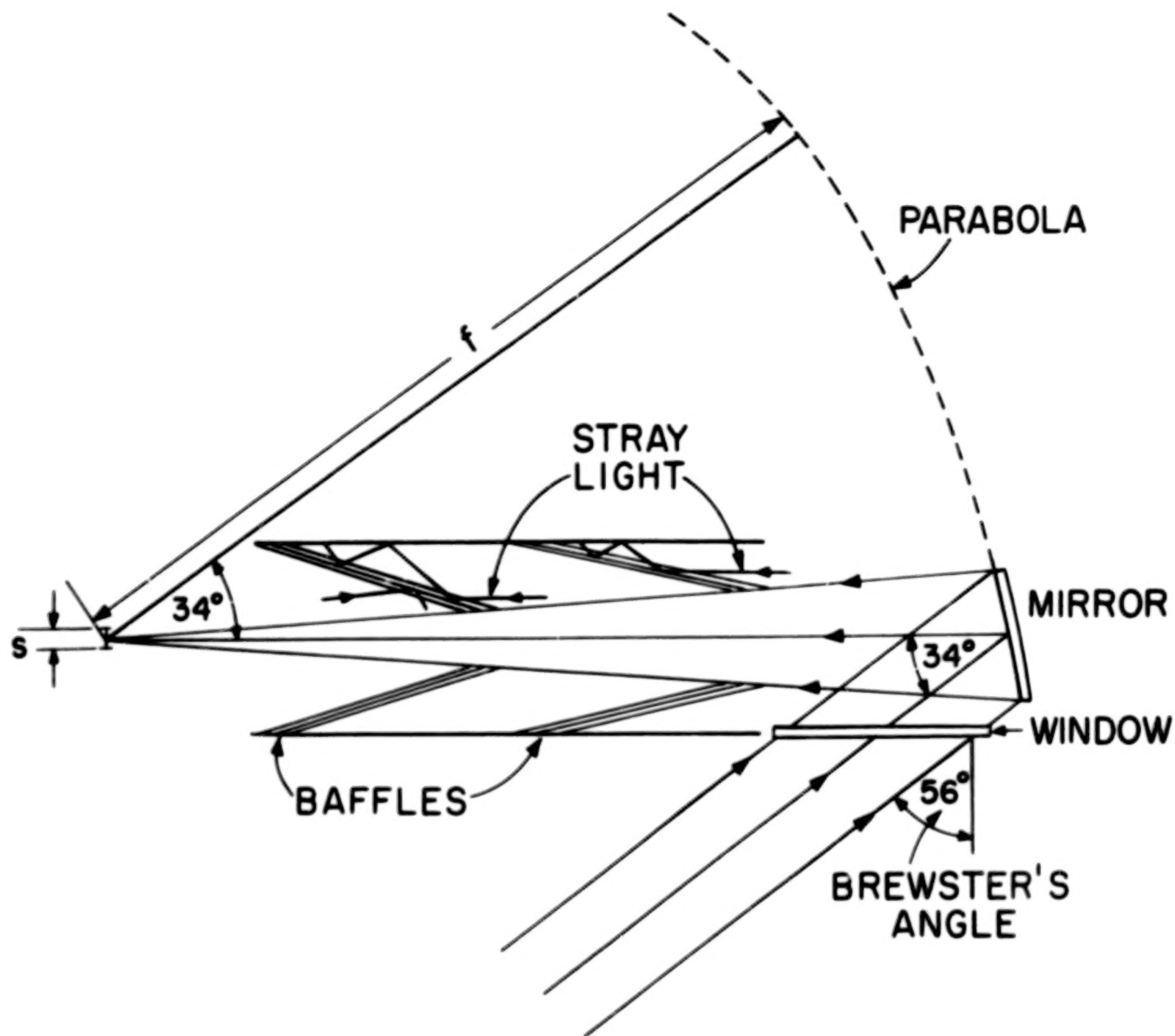
Fig. 38   Possible setup for focussing the submillimeter laser beam showing the
parabolic mirror and baffles.

138
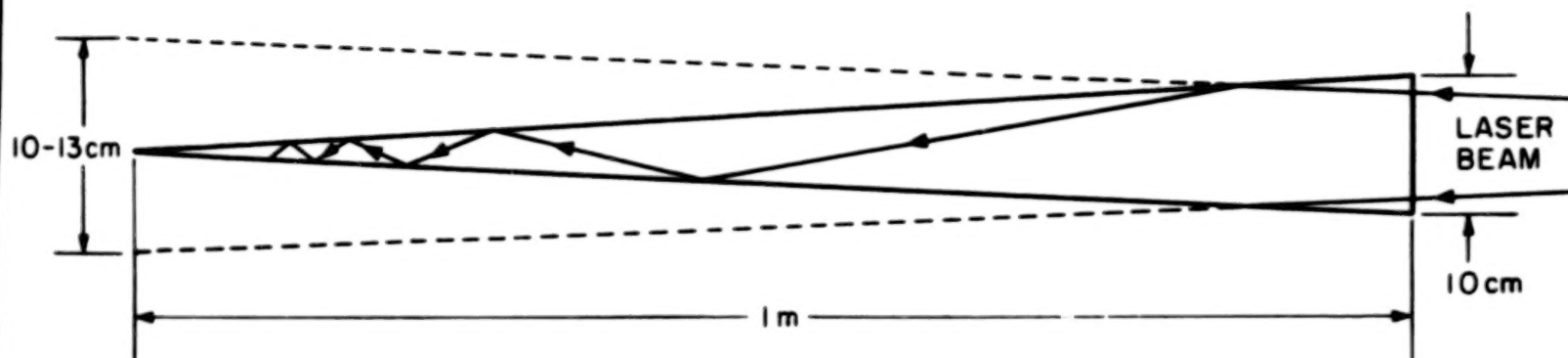
Fig. 39   Possible dimensions for a beam dump cone. Dashed lines indicate how
the laser beam would expand if no beam dump were present.

139
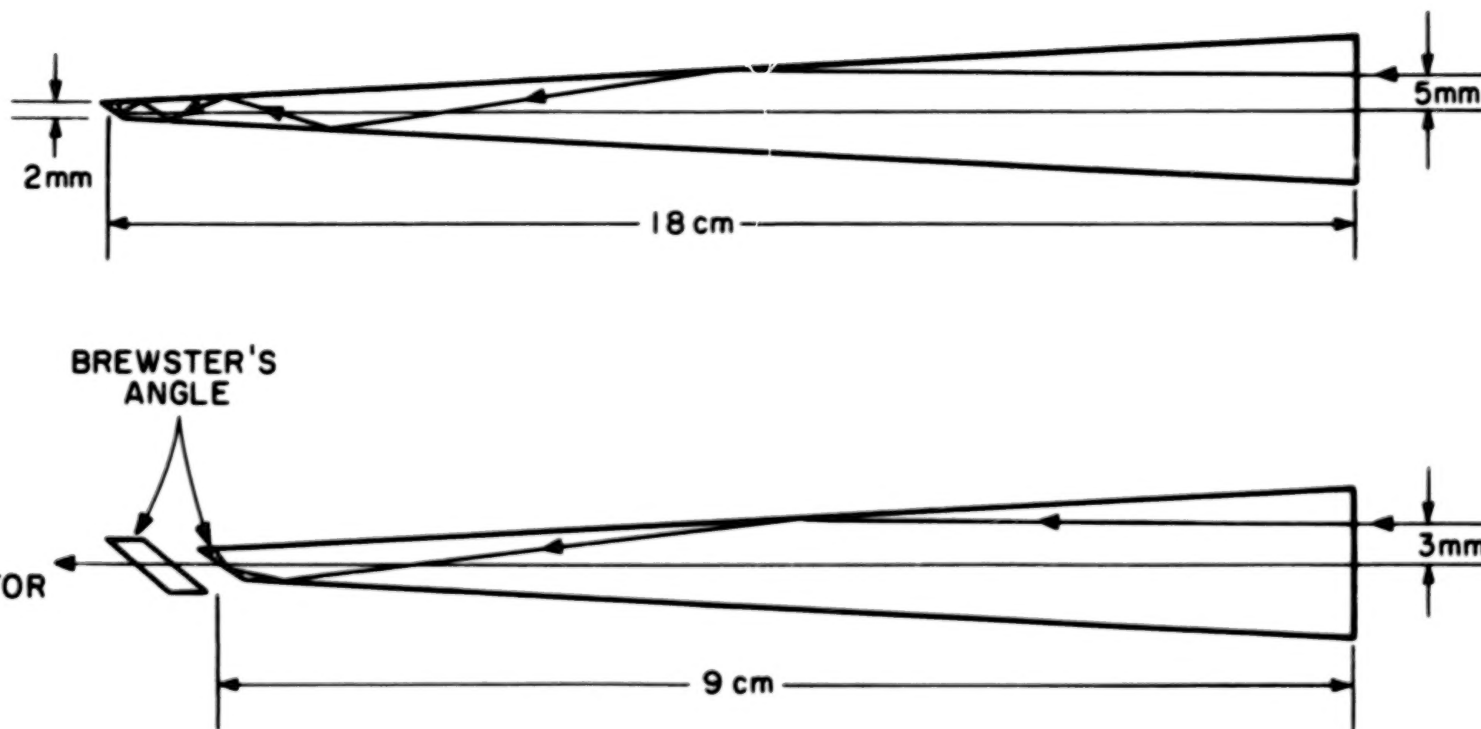
Fig. 40   Expanded views of the apex of the beam dump cone showing details of the
Brewster angle window for monitoring the laser pulse.

140
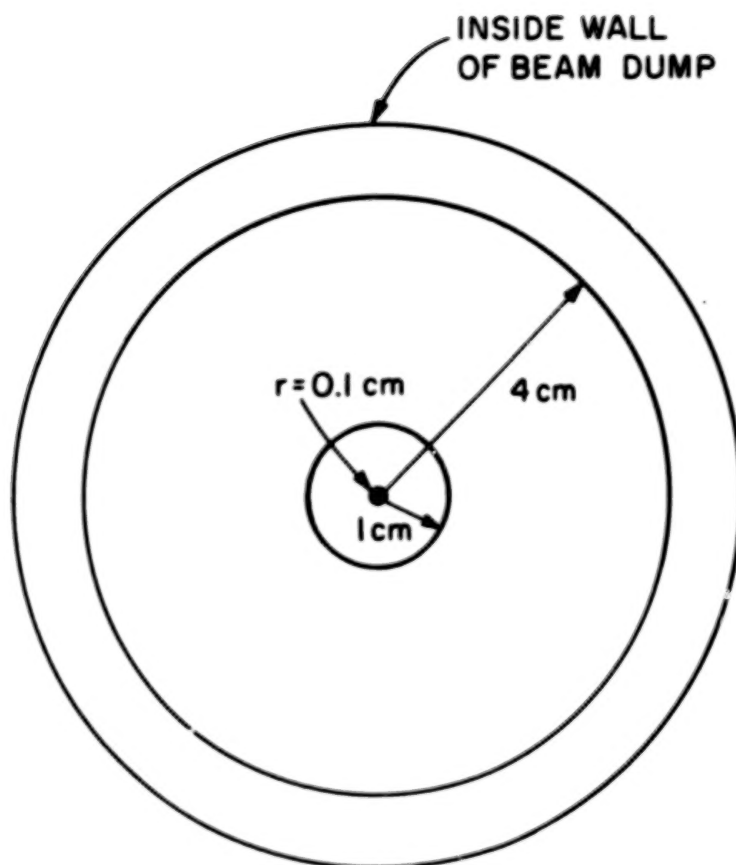
Fig. 41   Cross sectional view of the laser beam and beam dump at the beam dump access port. The laser beam is divided into three concentric areas to group the light rays of the laser beam by the number of reflections they receive.
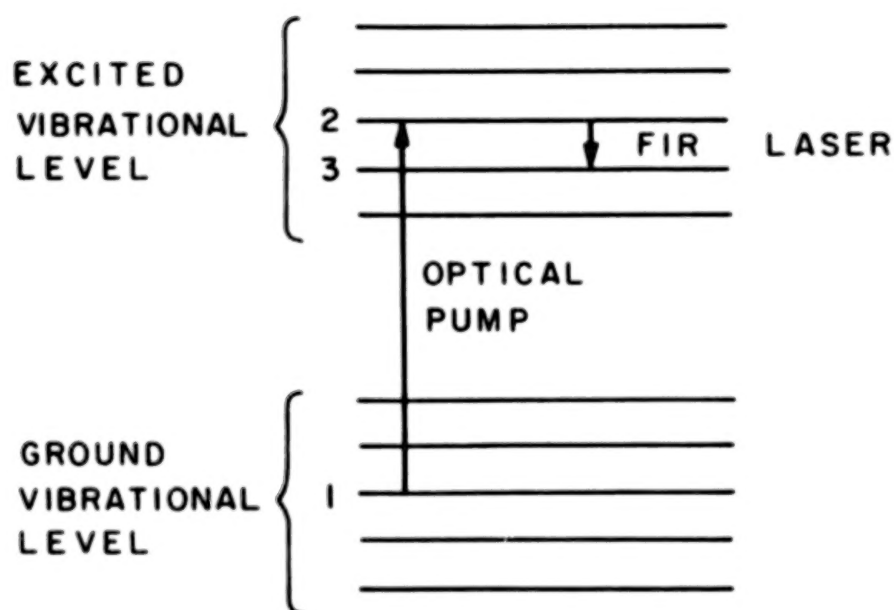
Fig. 42   Energy level diagram of an optically pumped submillimeter laser. The submillimeter transition (FIR) takes place between two rotational levels of the upper vibrational state.
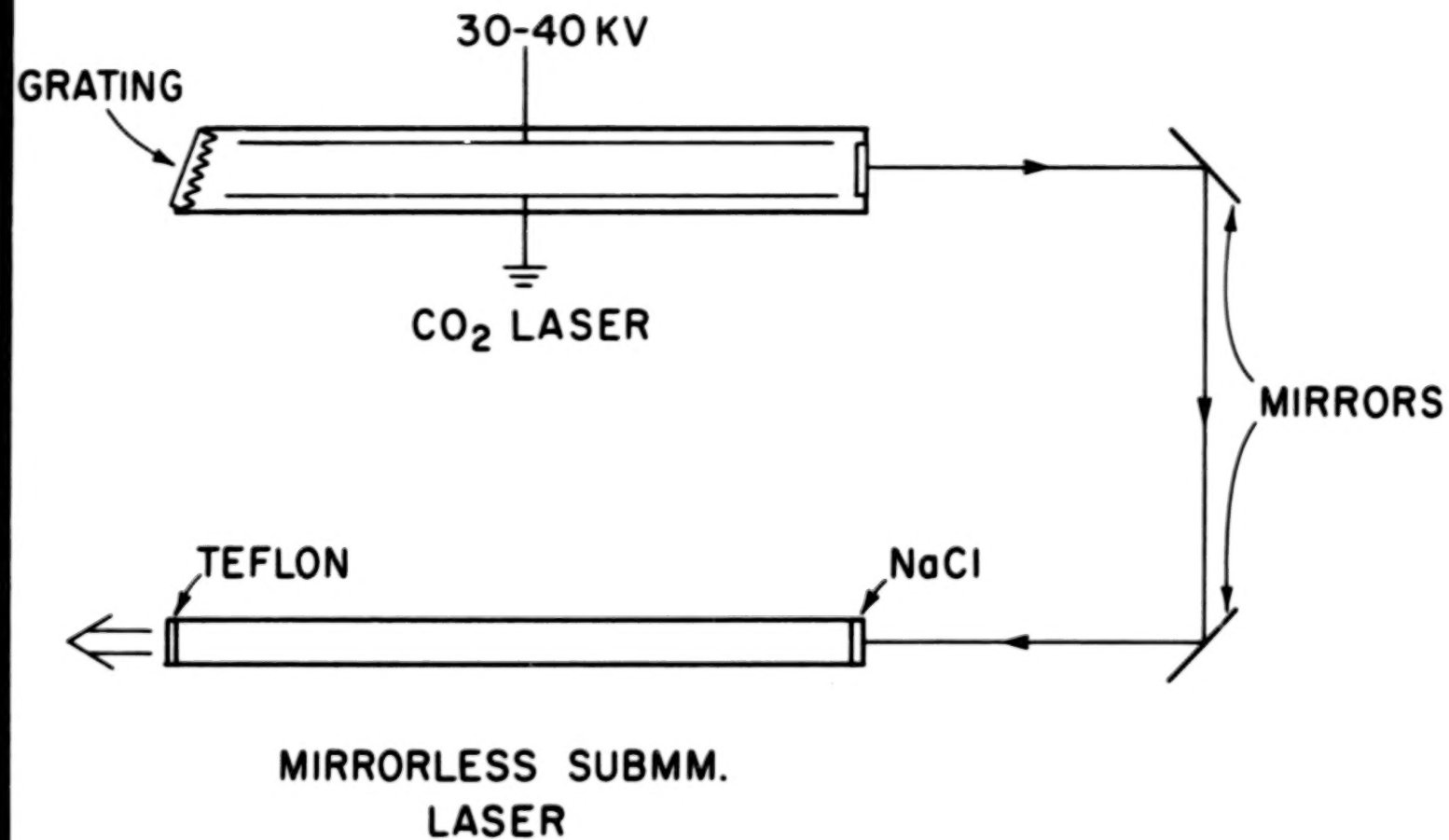
Fig. 43   Possible experimental setup for producing submillimeter laser emissions.

143
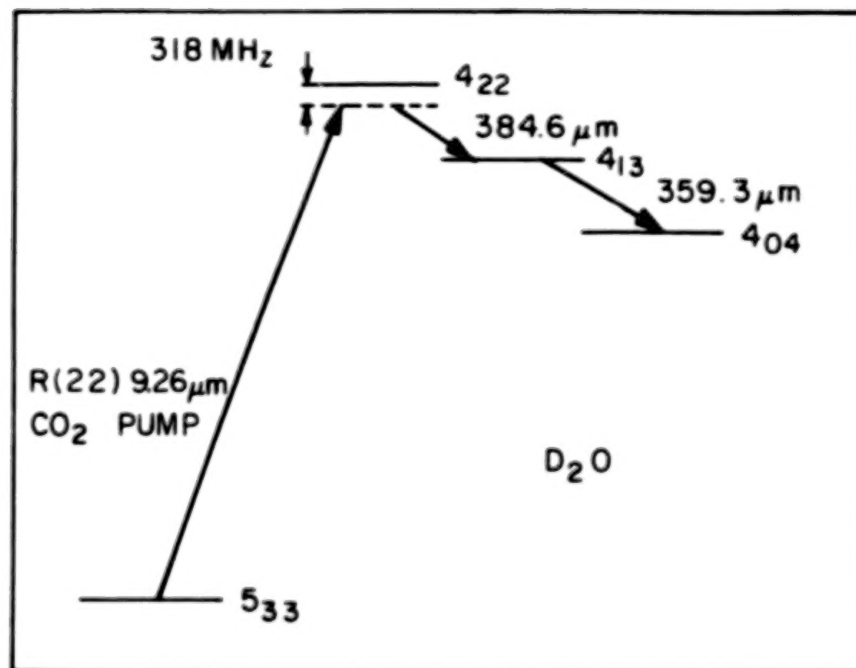
Fig. 44   The energy levels of D_2O involved in the submillimeter laser action.
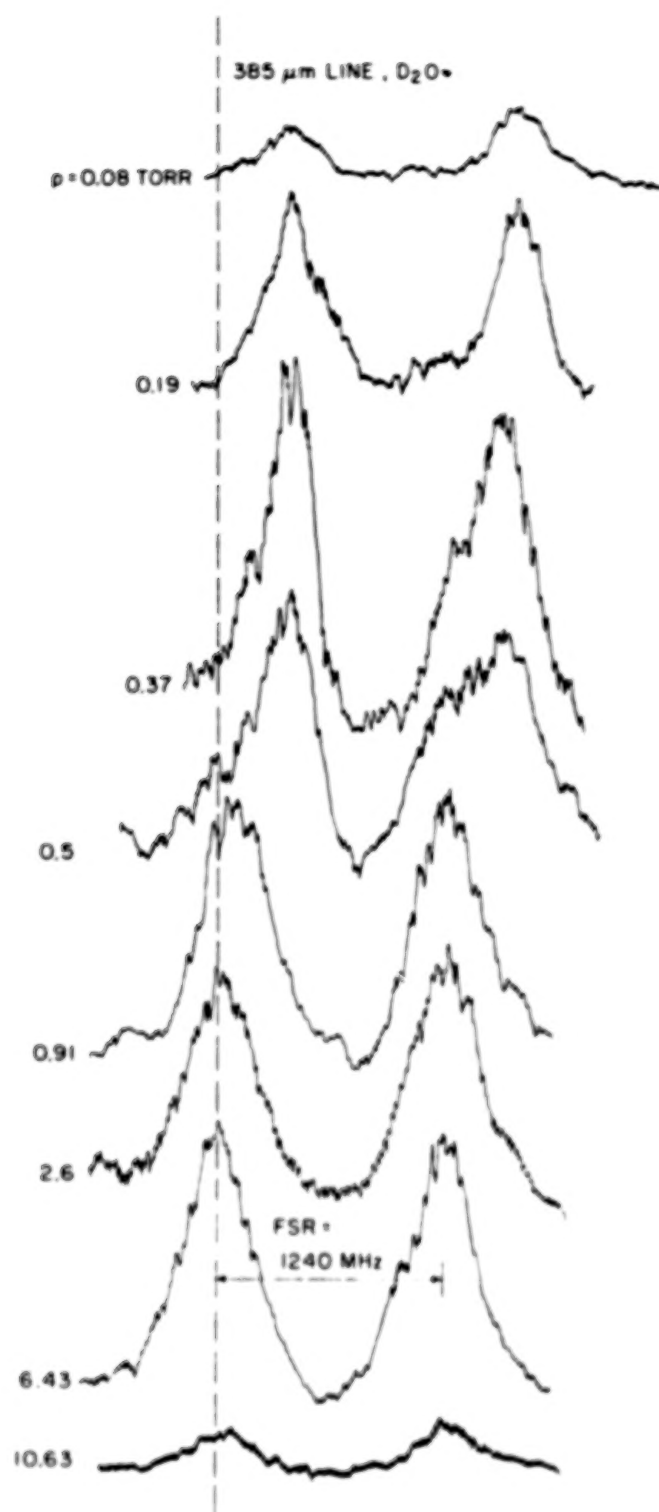
Fig. 45 Experimental Fabry-Perot scans of D_2O superradiance at 385 μm showing the switching from the line center transition to the Raman transition as pressure is increased.

145
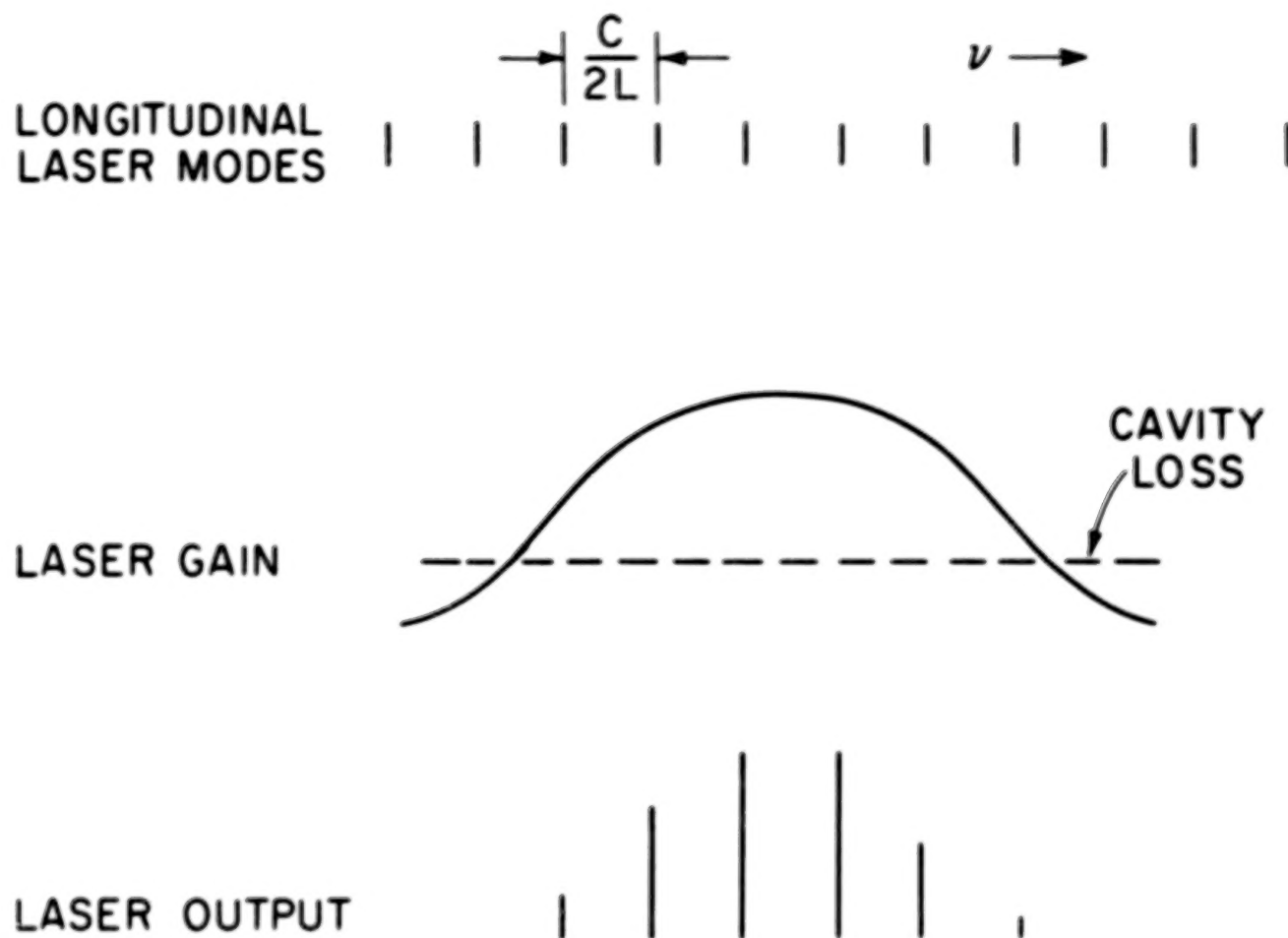
Fig. 46   Illustration of the effect of longitudinal modes on laser output.

146
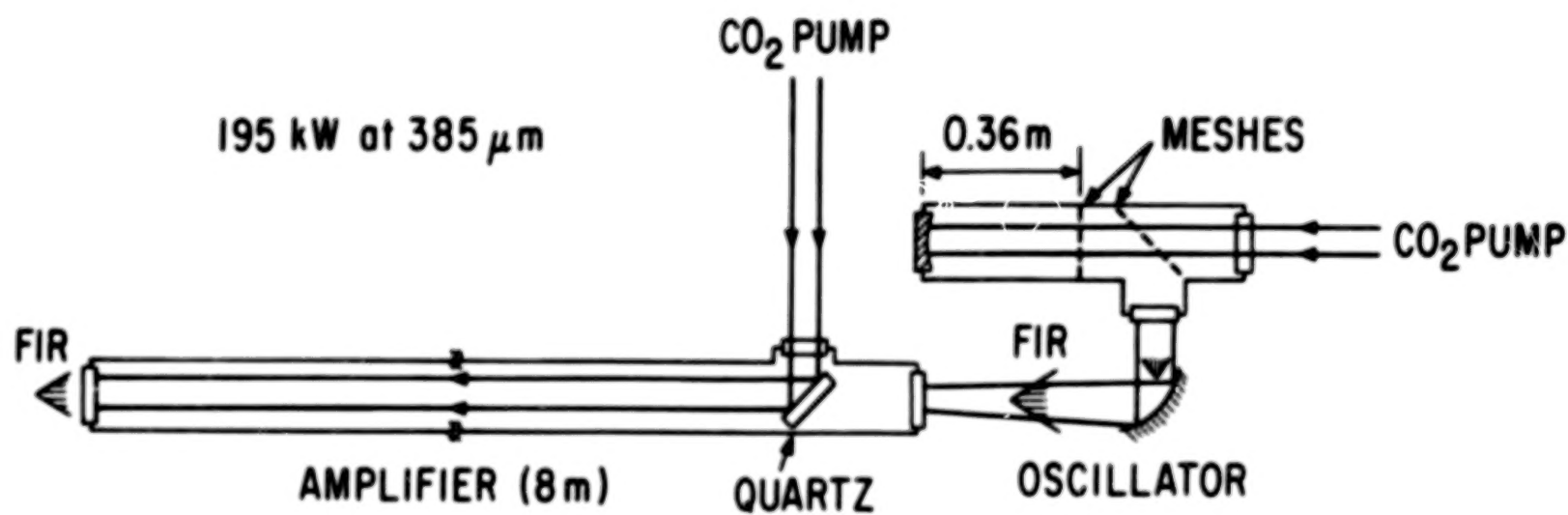
Fig. 47   Experimental details of the D_2O oscillator-amplifier setup.

147
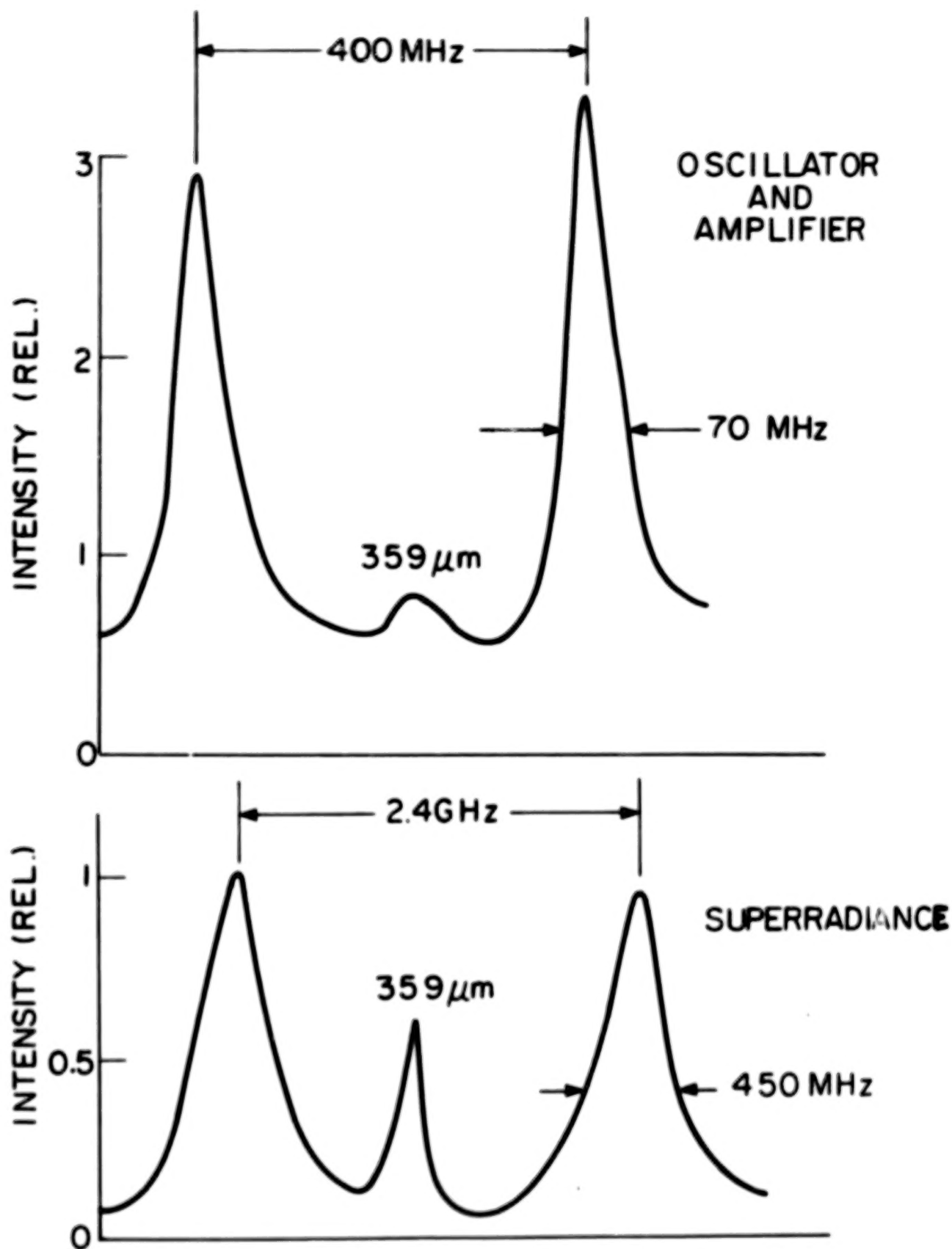
Fig. 48   Fabry-Perot scans of D_2O amplifier output. Upper curve shows the output
with the oscillator on and lower curve shows amplifier superradiance without
an oscillator signal.
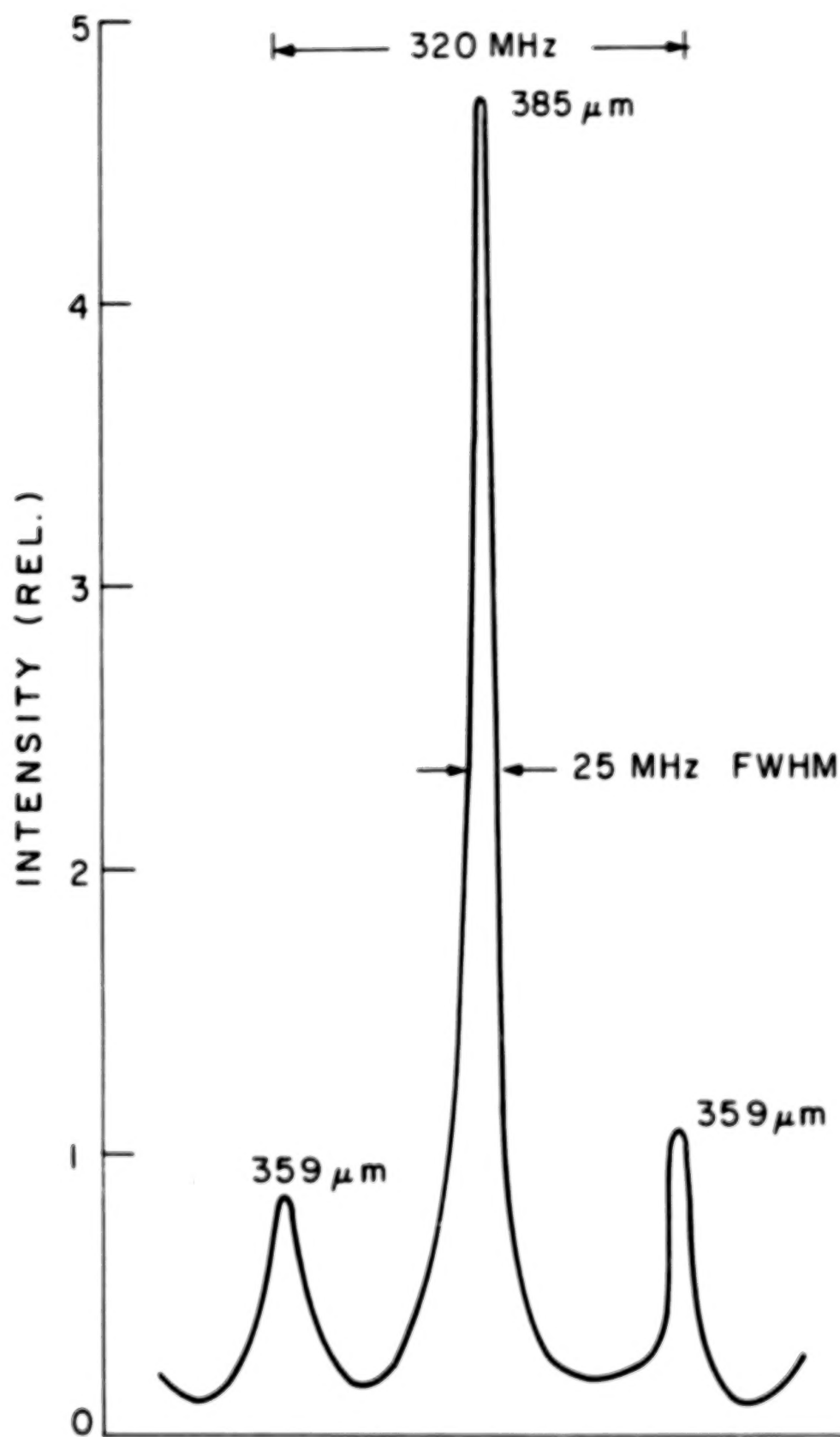
Fig. 49   Fabry-Perot scan of the output of the 36 cm long oscillator.

149
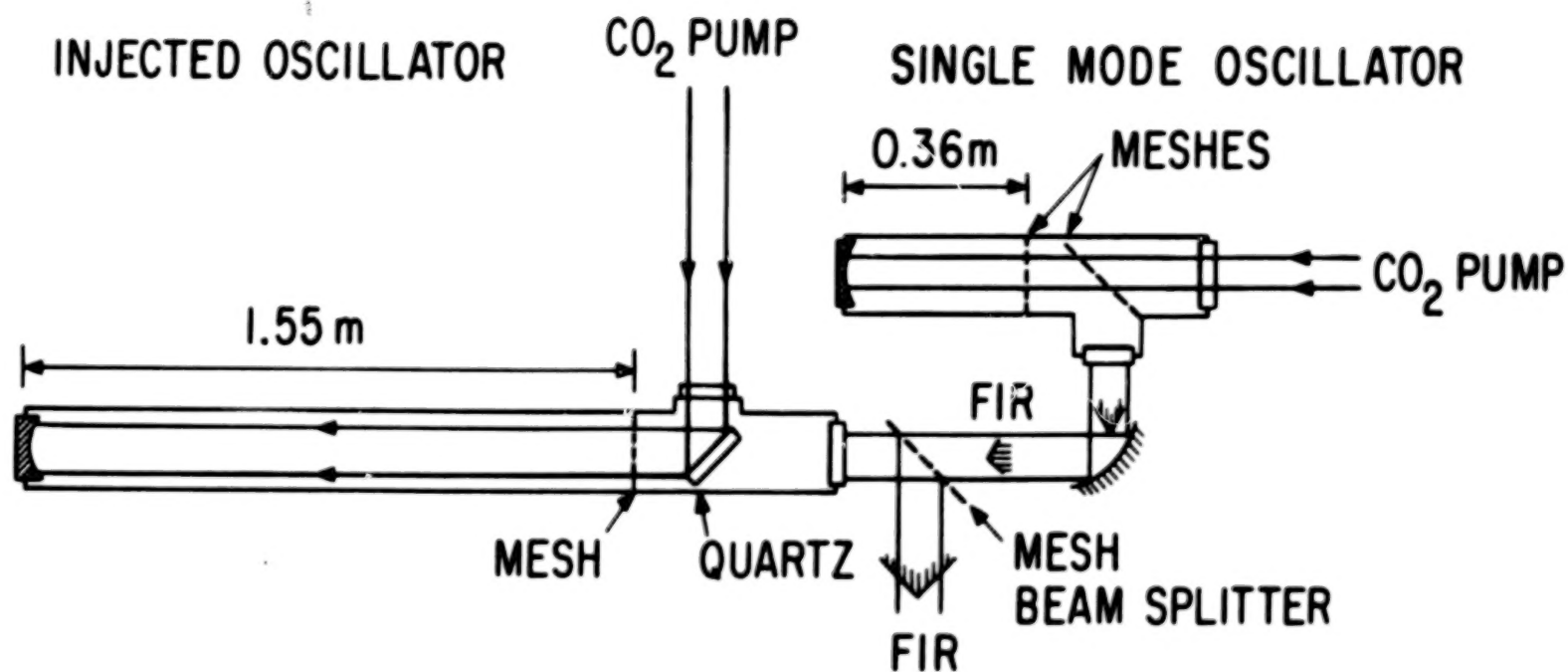
Fig. 50 Experimental arrangement for testing an injection oscillator.
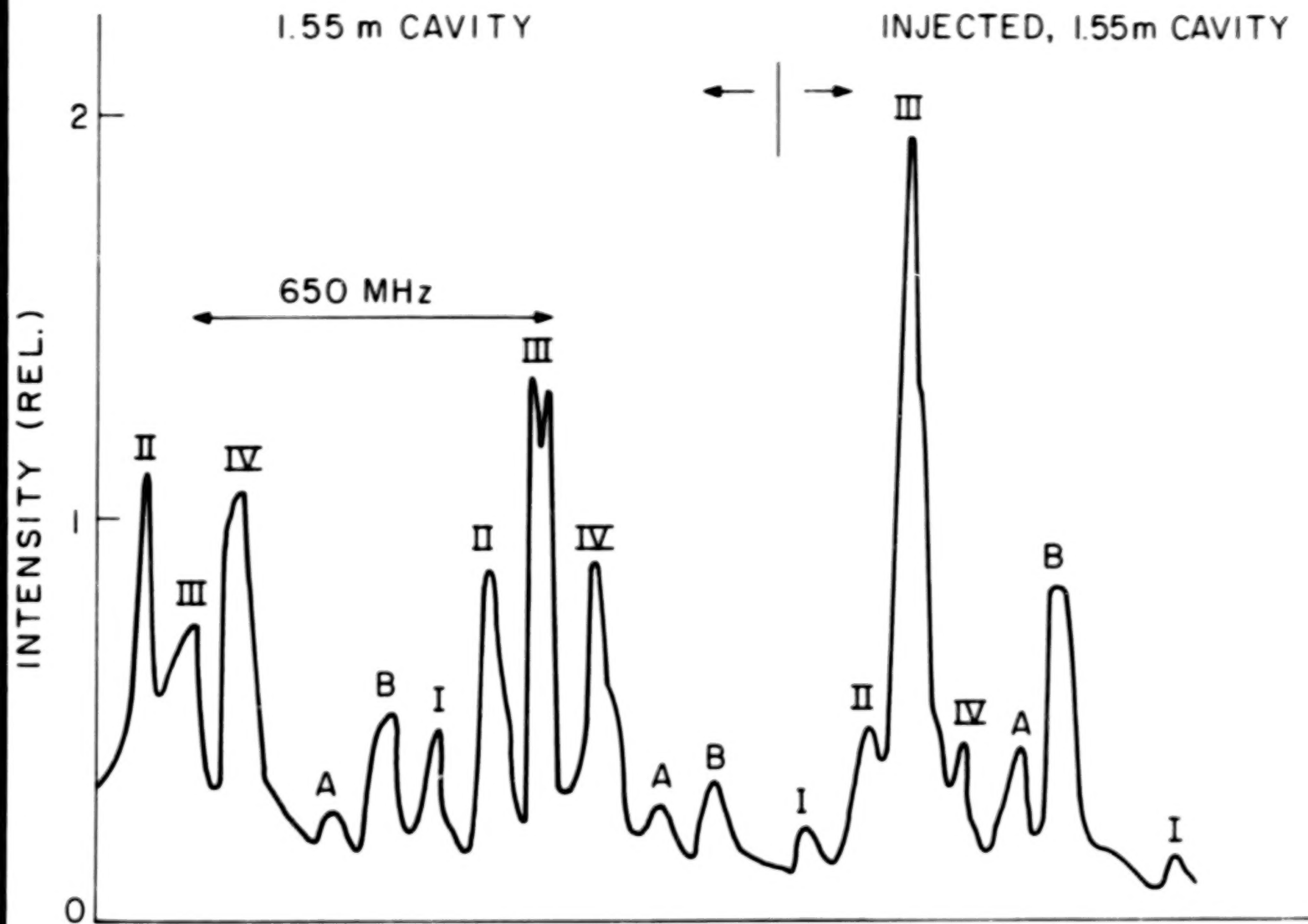
Fig. 51   Fabry-Perot scan showing the effect of injecting a signal from a short D_2O oscillator to control the modes of a long D_2O oscillator.
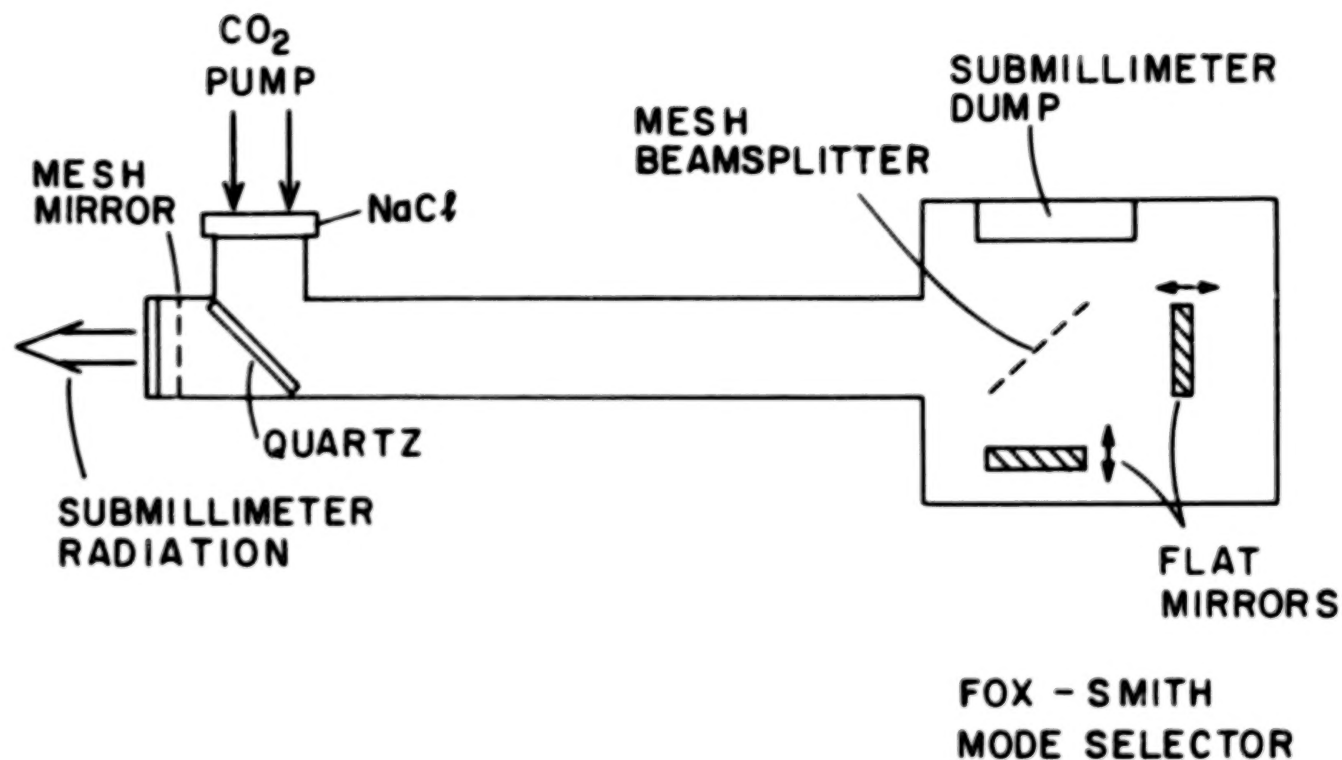
Fig. 52   Submillimeter oscillator with a Fox-Smith mode selector.

152
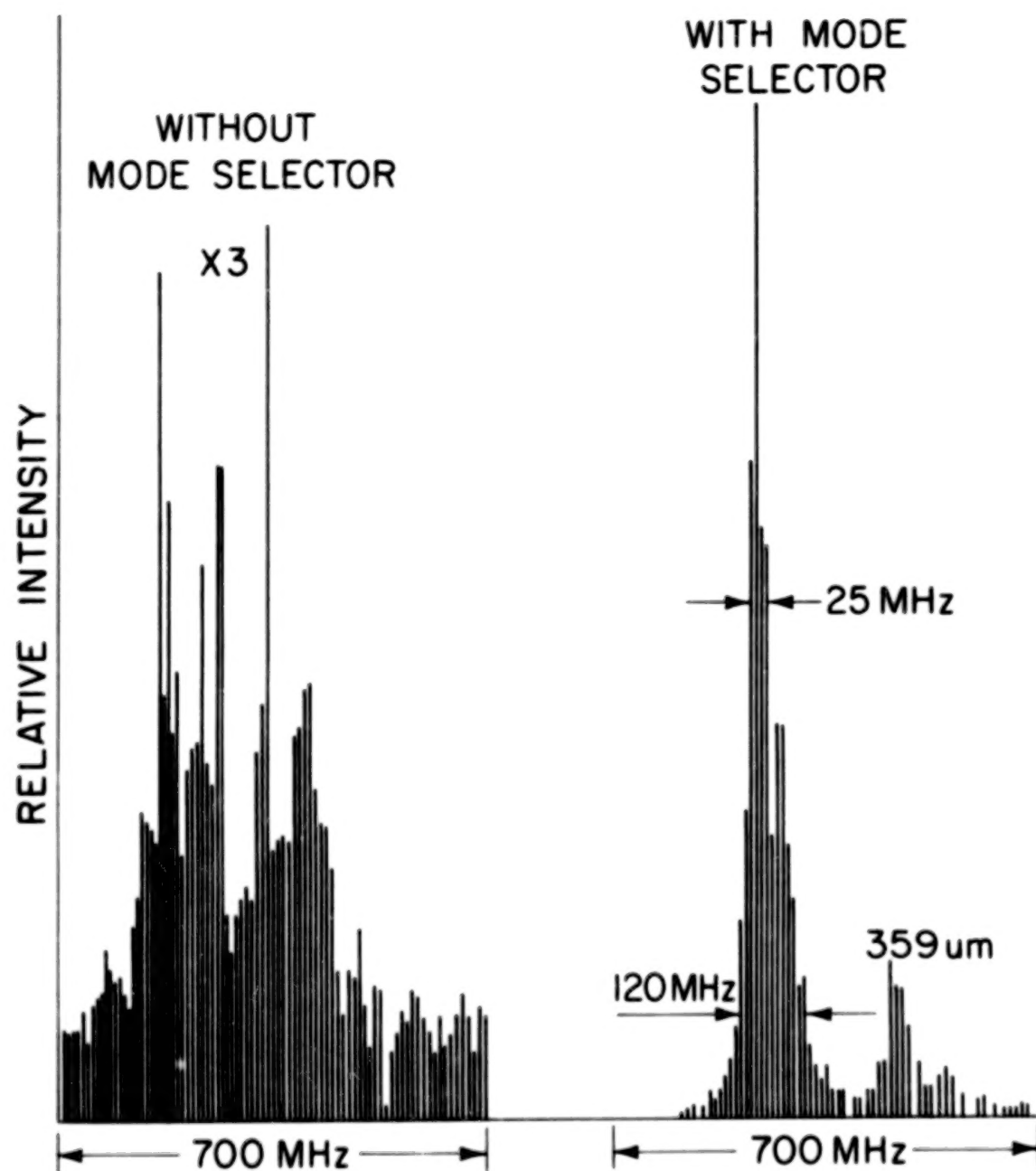
Fig. 53   Fabry-Perot scans showing the effect of the Fox-Smith mode selector on the output of a 1.6 m long D_2O laser oscillator.
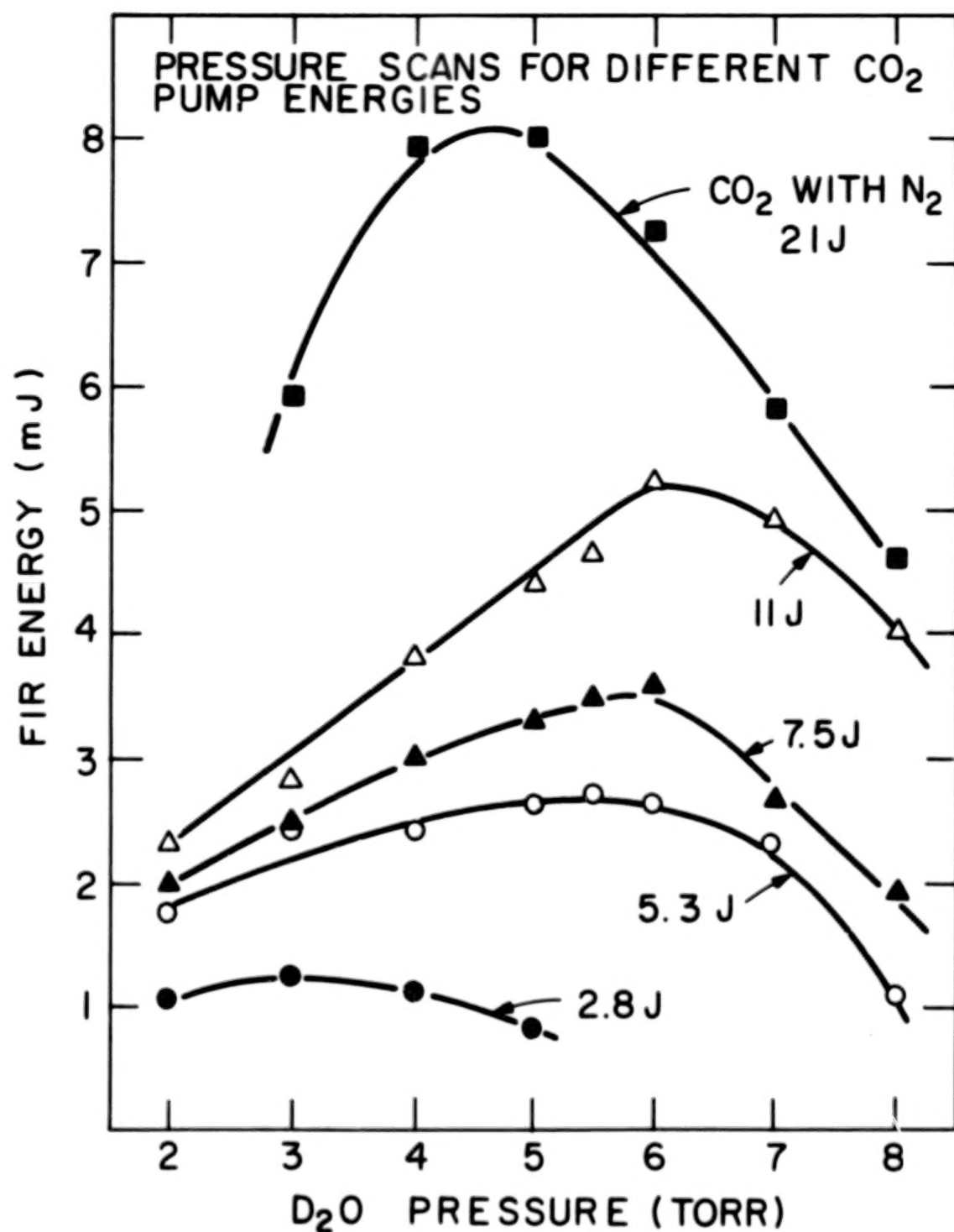
Fig. 54 D_2O pressure scans of Fox-Smith oscillator output at 385 μm on one mode for different CO_2 laser pump energies.
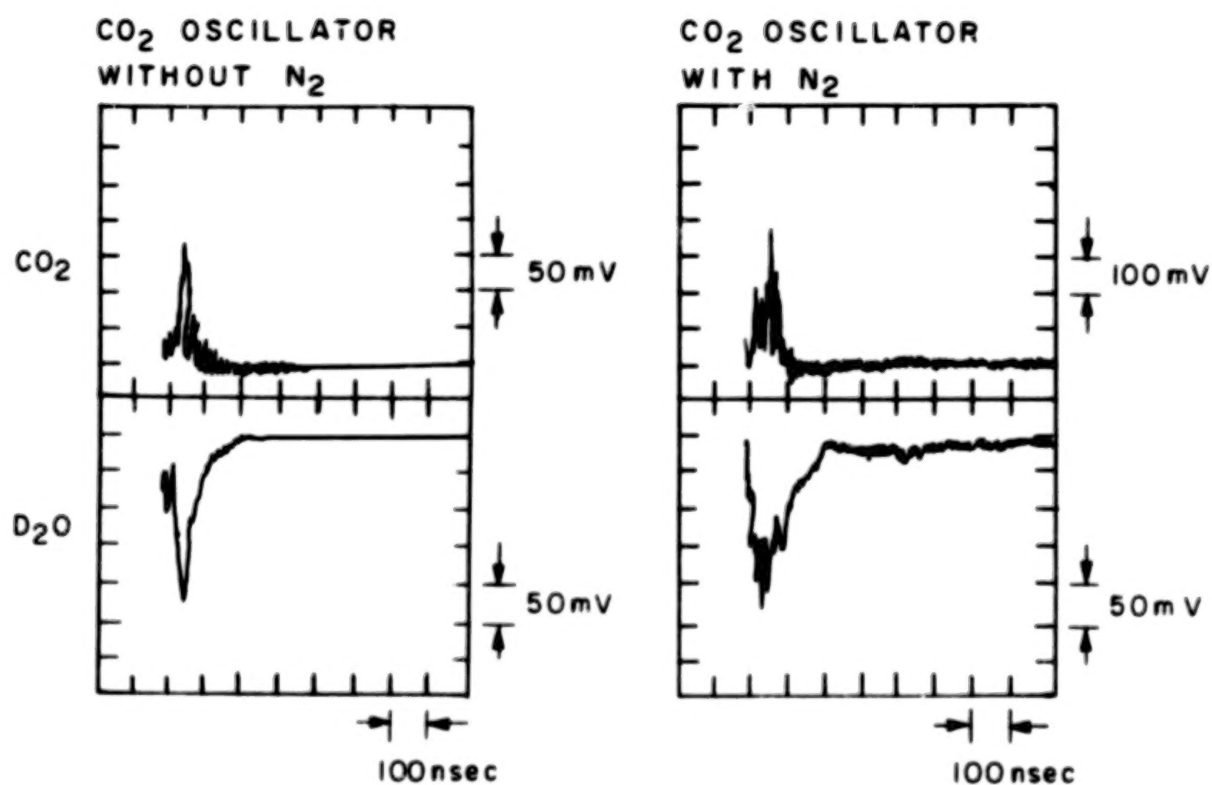
CO$_2$ OSCILLATOR
WITHOUT N$_2$

CO$_2$ OSCILLATOR
WITH N$_2$

CO$_2$

50 mV

100 mV

D$_2$O

50mV

50m V

100 nsec

100 nsec

Fig. 55   Time resolved photographs of the CO$_2$ and D$_2$O laser pulses for the CO$_2$ oscillator with and without nitrogen.

155
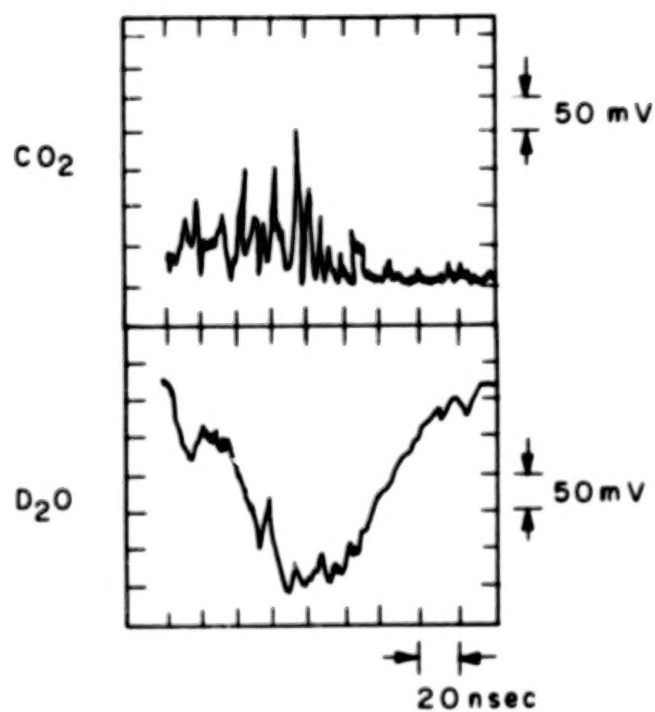
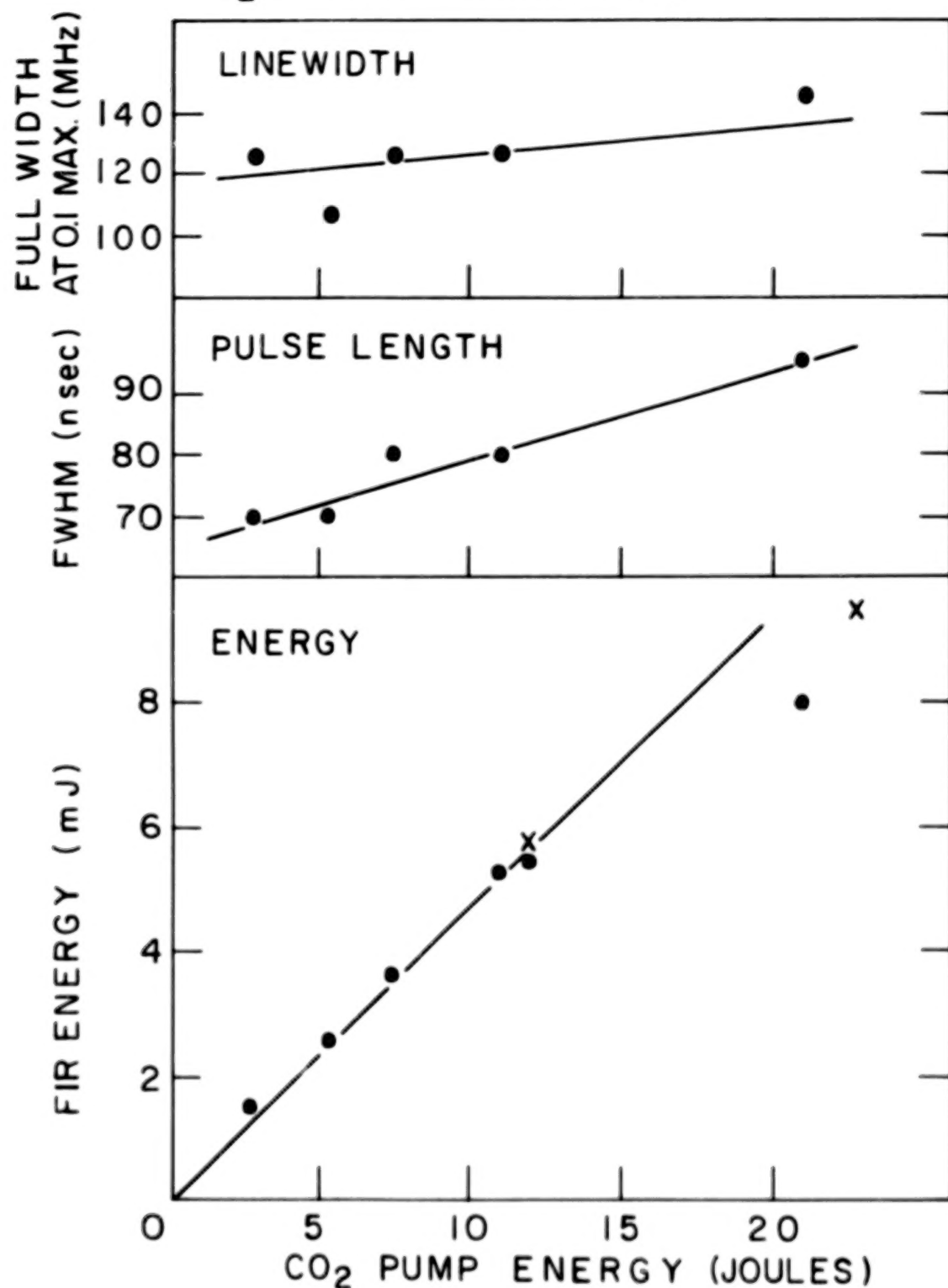Fig. 56 CO_2 and D_2O laser pulses on a 20 ns per division time scale.

156

Fig. 57 Submillimeter laser energy, pulse length, and 10 db linewidth at 385 μm as a function of CO_2 laser pump energy. 157
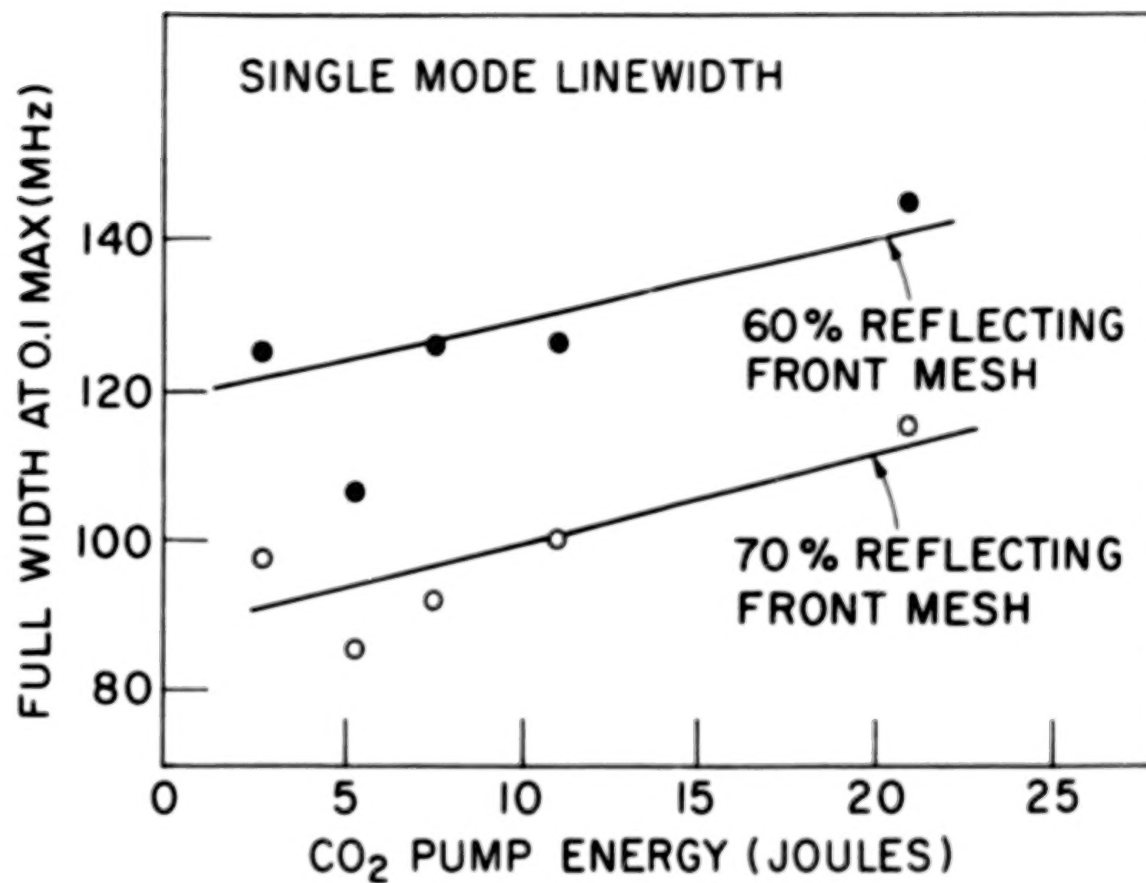
Fig. 58   The effect of changing the reflectivity of partially transmitting mirror
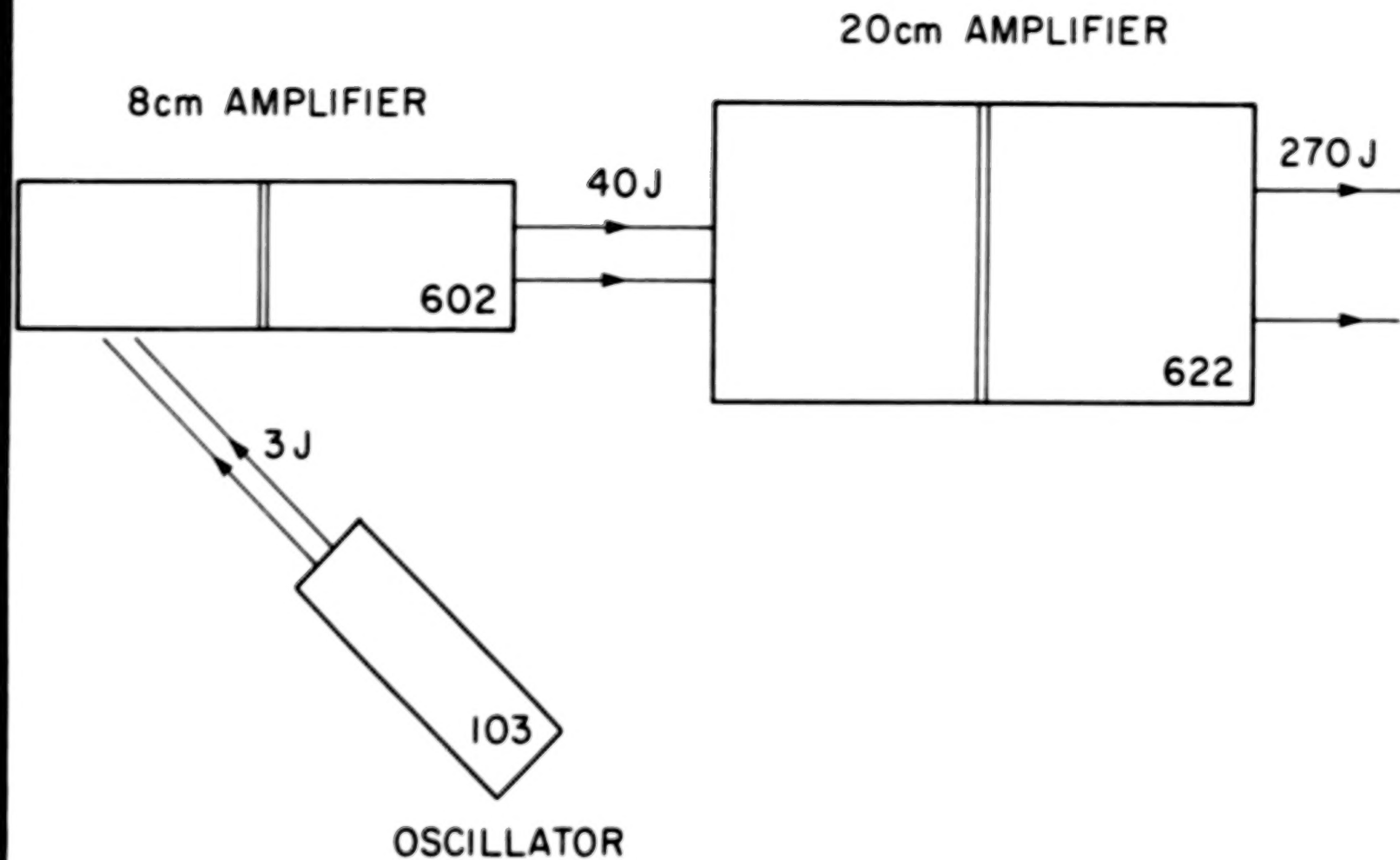in the laser cavity on linewidth.

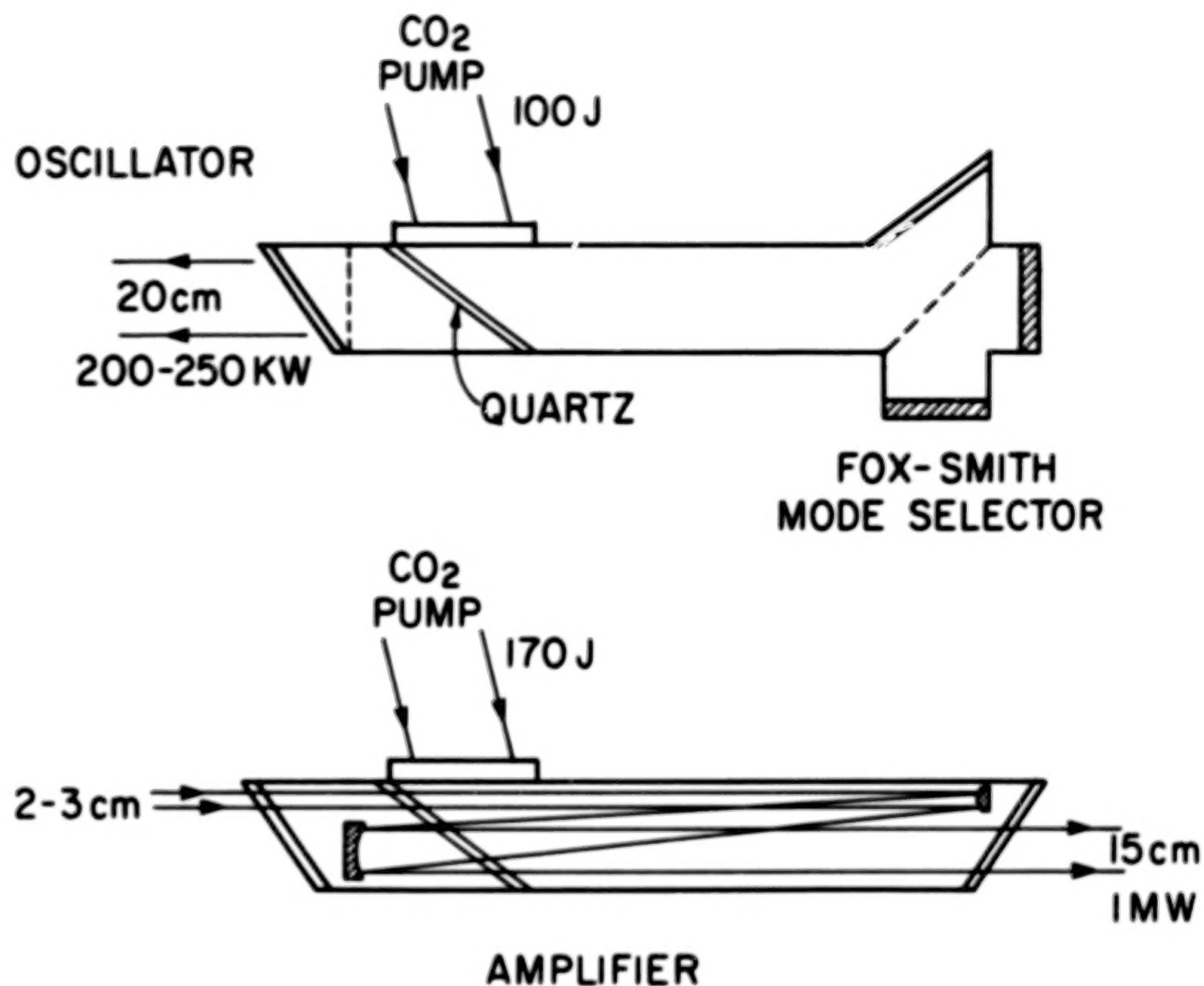Fig. 59   Sketch of 270 J CO_2 pump laser system.

OSCILLATOR

CO$_2$ PUMP

100 J

20cm

200-250 KW

QUARTZ

FOX-SMITH MODE SELECTOR

CO$_2$ PUMP

170 J

2-3 cm

15 cm

1 MW

AMPLIFIER

Fig. 60   Possible design of the 1 MW submillimeter laser oscillator and amplifier configuration.

160

1. Report No. NASA CR-2974	2. Government Accession No.	3. Recipient's Catalog No.	
4. Title and Subtitle DESIGN OF A SUBMILLIMETER LASER THOMSON SCATTERING SYSTEM FOR MEASUREMENT OF ION TEMPERATURE IN SUMMA		5. Report Date April 1978	
		6. Performing Organization Code	
7. Author(s) Herman C. Praddaude and Paul Woskoboinikow		8. Performing Organization Report No.	
		10. Work Unit No.	
9. Performing Organization Name and Address Massachusetts Institute of Technology Francis Bitter National Magnet Laboratory Cambridge, Massachusetts 02139		11. Contract or Grant No. NSG-3088	
12. Sponsoring Agency Name and Address National Aeronautics and Space Administration Washington, D.C. 20546		13. Type of Report and Period Covered Contractor Report	
		14. Sponsoring Agency Code	

16. Abstract

A thorough discussion of submillimeter laser Thomson scattering for the measurement of ion temperature in plasmas is presented. This technique is very promising and work is being actively pursued on the high power lasers and receivers necessary for its implementation. In this report we perform an overall system analysis of the Thomson scattering technique aimed to: (1) identify problem areas; (2) establish specifications for the main components of the apparatus; (3) study signal processing alternatives and identify the optimum signal handling procedure. Because of its importance for the successful implementation of this technique, we also review the work presently being carried out on the optically pumped submillimeter CH_3F and D_2O lasers.

17. Key Words (Suggested by Author(s)) Plasma ion temperature measurement Submillimeter laser Thomson scattering Ion temperature measurement by laser Thomson scattering		18. Distribution Statement Unclassified - unlimited STAR Category 75	
19. Security Classif. (of this report) Unclassified	20. Security Classif. (of this page) Unclassified	21. No. of Pages 162	22. Price* A08

END

9. 21. 78